1. AGENCY USE ONLY (Leave Blank)	2. REPORT DATE	3. REPORT TYPE AND DATES COVERED Final Report 15 May 2003 - 14 May 2007

4. TITLE AND SUBTITLE Hybrid Carbon-Glass Fiber/Toughened Epoxy Thick Composite Joints Subject to Drop-Weight and Ballistic Impacts at Various Temperatures	5. FUNDING NUMBERS DAAD19-03-1-0086

6. AUTHOR(S)

Benjamin Liaw, Feridun Delale

7. PERFORMING ORGANIZATION NAME(S) AND ADDRESS(ES) CUNY - City College of New York Department of Mechanical Engineering	8. PERFORMING ORGANIZATION REPORT NUMBER

9. SPONSORING / MONITORING AGENCY NAME(S) AND ADDRESS(ES) U. S. Army Research Office P.O. Box 12211 Research Triangle Park, NC 27709-2211	10. SPONSORING / MONITORING AGENCY REPORT NUMBER 45326.1-EG-HSI

11. SUPPLEMENTARY NOTES

The views, opinions and/or findings contained in this report are those of the author(s) and should not be construed as an official Department of the Army position, policy or decision, unless so designated by other documentation.

12 a. DISTRIBUTION / AVAILABILITY STATEMENT Approved for public release; distribution unlimited.	12 b. DISTRIBUTION CODE

13. ABSTRACT (Maximum 200 words)

Final Report

14. SUBJECT TERMS	15. NUMBER OF PAGES
	16. PRICE CODE

17. SECURITY CLASSIFICATION OR REPORT UNCLASSIFIED	18. SECURITY CLASSIFICATION ON THIS PAGE UNCLASSIFIED	19. SECURITY CLASSIFICATION OF ABSTRACT UNCLASSIFIED	20. LIMITATION OF ABSTRACT UU

Enclosure 1

Final Report

Hybrid Carbon-Glass Fiber/Toughened Epoxy Thick Composite Joints Subject to Drop-Weight and Ballistic Impacts

by

Benjamin Liaw and Feridun Delale
Department of Mechanical Engineering
The City College of
The City University of New York
New York, New York

for

December 2007

PROJECT SUMMARY

This ARO project (Contract No. DAAD19-03-1-0086) from City College of City University of New York (CCNY of CUNY) was submitted in response to ARO's FY 2002 DoD Instrumentation and Research Support for Hispanic Serving Institutions (HSIs), BAA No. DAAD19-02-R-0010 to conduct research on hybrid carbon-S2 glass fiber/toughened epoxy thick-section, hybrid interwoven composite joints subject to drop-weight and ballistic impacts. Dr. Basavaraju B. Raju of U.S. Army TACOM-TARDEC was the research collaborator and Dr. Bruce LaMattina of ARO was the program manager.

The main objectives of this project are (1) to conduct tensile, drop-weight impact and ballistic impact tests of monolithic S2 glass fiber/toughened epoxy composites and hybrid carbon-S2 glass fiber/toughened epoxy composites, (2) to verify the experimental results using damage-mechanics based, 3-D dynamic nonlinear finite element method embedded in a commercial software package, LS-DYNA, (i.e., a combined experimental-numerical approach was used in the research), (3) to provide data of research results to supplement Army's current missions in the FCS, (4) to enhance the proposers' research capabilities on composites at their institute through interaction with Army researchers and facilities so that they may participate in Army's mainstream research in the future, and (5) to involve graduate and undergraduate students, especially those from underrepresented minorities, actively in the research so that they can gain meaningful research experience and may develop interest in pursuing advanced degrees in engineering.

It is believed that results obtained in this study could benefit several Army missions and current interests in the development and implementation of Future Combat Systems (FCS), such as damage tolerance and ballistic impact study of composite integral armors (CIAs) for composite armored vehicles (CAVs) demonstrator, rotary-wing structures technology (RWST) for RAH-66 Comanche's lower forward fuselage demonstrator, etc.

1.   Introduction

This ARO project (Contract No. DAAD19-03-1-0086) from City College of City University of New York (CCNY of CUNY) was submitted in response to ARO's FY 2002 DoD Instrumentation and Research Support for Hispanic Serving Institutions (HSIs), BAA No. DAAD19-02-R-0010 to conduct research on hybrid carbon-S2 glass fiber/toughened epoxy thick-section, hybrid interwoven composite joints subject to drop-weight and ballistic impacts. The two principal investigators, Professors Benjamin Liaw and Feridun Delale, are faculty members of the Department of Mechanical Engineering at CCNY since 1984. The research effort was in collaboration with Dr. Basavaraju B. Raju of U.S. Army Tank-Automotive & Armaments Command (TACOM) – Tank-Automotive Research, Development Engineering Center (TARDEC). Dr. Bruce LaMattina was the program manager of this project at ARO.

Established in 1847 CCNY mainly serves residents of New York City, especially those from middle- and low-income families. CCNY is a minority institution and an HSI (DUNS + 4 No. 64932676) with more than 70% of the student body being minorities (approximately half of them African-Americans and the other half Hispanics). Founded in 1920, the Grove School of Engineering (GSOE) at CCNY is the only public institution offering Bachelor of Engineering degrees in New York City. Currently, the CCNY GSOE has an enrollment of more than 2,000 undergraduate and more than 500 graduate students. More than half of the GSOE's students are minorities.

We believe that the research results obtained from this study could benefit several Army missions and current interests in the development and implementation of Future Combat Systems (FCS), such as damage tolerance and ballistic impact study of composite integral armors (CIAs) for composite armored vehicles (CAVs) demonstrator, rotary-wing structures technology (RWST) for RAH-66 Comanche's lower forward fuselage demonstrator, etc. [1,2]. Through the concept of FCS, the proposed study is within Army's current umbrella plan, Army 2010 and Beyond, which is designed as a transformation of the Army to an Objective Force before 2025.

2.   Goals and Objectives

The main goals and objectives of this study are:

- To conduct tensile, drop-weight impact and ballistic impact tests of monolithic S2 glass fiber/toughened epoxy composites and hybrid carbon-S2 glass fiber/toughened epoxy composites.
- To verify the experimental results using damage-mechanics based, 3-D dynamic nonlinear finite element method embedded in a commercial software package, LS-DYNA, (i.e., a combined experimental-numerical approach was used in the research).
- To provide data of research results to supplement Army's current missions in the FCS.
- To enhance the proposers' research capabilities on composites at their institute through interaction with Army researchers and facilities so that they may participate in Army's mainstream research in the future.
- To involve graduate and undergraduate students, especially those from underrepresented minorities, actively in the research so that they can gain meaningful research experience and may develop interest in pursuing advanced degrees in engineering.

3. Technical Background

3.1: Usage of composites in Army ground vehicles

The use of high performance (i.e., light weight, high strength and stiffness) composites is a potential enabling technology to make future combat vehicles lighter, more easily deployable, versatile, and survivable. For in the design of composite integral armors (CIAs) [1], the key supporting layer to the ceramic tiles is a thick-section structural composite, which is lighter than its traditional metal counterpart. The adoption of this technology is critical to the success of the U.S. Army's Future Combat Systems since the use of composite materials may pave the way for researchers and engineers to optimize many facets of a combat vehicle's battlefield capability, namely, structural integrity, durability, ballistic protection, repairability, and signature reduction. Such a multi-functional improvement will make this vehicle more suitable for strategic global deployment [2]. In short, the quintessence of integrated survivability of ground combat vehicles, including chassis and turret, is the avoidance of detection (through signature reduction), hit (through light-weight mobility), and penetration (through ballistic protection), and if damaged, repairability at an affordable cost (i.e., truly supportable). All these can be achieved by replacing the current heavy metal parts with fiber reinforced composites.

In general, a polymer-matrix composite (PMC) reinforced with ceramic (including glass and carbon) or organic (e.g., Kevlar aramid) fibers has a tensile strength comparable with that of metals. Because of its relative lower density, the composite may usually have a more attractive specific tensile strength, i.e., tensile strength per unit weight. However, as a trade-off, the use of ceramic or Kevlar fibers in a composite renders the composite more brittle. Consequently, the composite has a relative weaker impact resistance (called *impact toughness* or *impact tolerance*) in comparison to its metallic counterpart [3]. This is particularly true if the matrix material is made of the more brittle thermosets, rather than the ductile thermoplastics.

Damage in a composite structure, caused by mechanical, thermal, and/or environmental loading, can have profound effects on the properties, performance, and life-expectation of that structure. Typical mechanical loading includes static, dynamic (or impact), fatigue (or cyclic), and creep. Once a composite is damaged, its residual stiffness, strength, and toughness should be re-evaluated to determine if the damaged composite can still meet the design specifications. Conventionally, damage tolerance in a composite structure is defined as the ability of the structure to tolerate a reasonable level of damage or defects that may be induced during manufacturing or while in service, without jeopardizing the safety of the structure and its users, i.e., structurally functional [3-6].

3.2: Thick-section composites

Although thin-laminate composites are the thrust of most structural applications of composites, the use of thick-section composites in heavy-duty structures, such as submarine hulls and armored vehicles, have been proved to be feasible. In particular, thick-section composite joints are very important structural elements in Army's advanced ground combat vehicles, such as the composite armored vehicles (CAVs), since they are used not only for the vehicle's body, but also for joining the ceramic/PMC armor to the vehicle for easy opening for inspection and repair. On battlefields these composite joints very often are subject to severe loading conditions and environments, such as impact and penetration, freezing and desert-like temperatures, etc.

The transfer of scientific and technological knowledge from that of thin-laminate composites to thick-section composites is not a trivial process. Just to name a few, the classical lamination theory is no longer valid; instead, three-dimensional effects, including edge delamination, cross-sectional warping, moduli variation through thickness and dynamic behavior, should be taken into account. Scaling effect should be considered when dealing with thick-section composites [7-10]. Fiber waviness is often introduced in thick section composites during manufacturing process due to improper resin infiltration or non-uniform composite curing and consolidation [10]. Thermal damage may be caused by high temperature (thermal spiking) in the interior of the thick section due to exothermic cross-linking reactions of thermosetting matrix materials and poor heat transfer in the composite. Finally, residual stresses can be easily induced due to the heterogeneous nature of the constituent materials and the high processing temperature needed for thick-section composites. Since thick-section composites behave very differently from their thin-laminate counterparts, research on this load-bearing composite structure has gained a lot of attention recently. The afore-mentioned issues, such as fiber waviness, cross-sectional warping, edge delamination, moduli variation through thickness, three-dimensional stress wave propagation, etc., have been studied by researchers using various experimental techniques (ultrasound [11-14], vibration [15], dynamic moiré interferometry [16], neutron radiography [17], transient thermography [18]). Damage resulting from shock, drop-weight impact, tensile, compressive, shear and three-point bending were investigated experimentally and analytically by other researchers [19-32].

3.3: Hybrid composites

So far, most of studies of load-bearing capability of thick-section composites have been limited to composite materials made of single fiber system [7-32]. This is especially true for composite joints even though joining is very critical in the manufacturing and repair of composite structures [33-36]. On the other hand, there have been extensive investigations and engineering applications of thin-laminate composites made of hybrid fiber composites, which incorporate different types of fibers in a single composite system. The first hybrid composite utilizing fiberglass reinforced plastics and a honeycomb core made of balsa wood was produced in the U.S. in 1942 [37]. Since then the use of high performance fiber hybrid composites has been growing rapidly. One of the advantages of using hybrid composites is the flexibility in the choice and distribution of fiber reinforcements. Hancox [38] classified four basic types of hybrid composites: Type A is made of intermingling fibers of different types in a common matrix (i.e., *intermingled* or *intraply*); Type B is formed by laminating layers with fibers of different types (i.e., *interlaminated* or *interply*); Type C is in a form of fiber skins with a fiber core; and Type D is constructed by fiber skins with a non-fiber core. In addition, if the reinforcements are fabric, each fabric may contain more than one-type of fiber and is termed *interwoven* [39].

Indeed, because of the freedom of choosing reinforcement and matrix constituents and the selection of manufacturing process, the possible types of hybrid composites useful for scientific and engineering applications can run the gamut. Although most of the reinforcements used in hybrid composites are continuous fibers, such as carbon (graphite), glass, Kevlar, boron, etc., [40-51], other forms of reinforcements, such as natural fibers (bamboo, oil palm, etc.) [52,53], woven or non-woven fabrics, glass mats, and interplies [54-62], short fibers [63-65], particulates (glass beads, calcite and talc particles, etc.) [64], wollastonite whiskers [65], the relatively inexpensive thermoplastic fibers (PET, polyethylene, polypropylene, etc.) [65-71],

thermotropic liquid crystalline polymer (TLCP) fibrils [72,73], etc., have also been used. The choice of resin system is also very broad [74] and may include almost all types of polymers. For instance, to manufacture a polymer matrix hybrid composite, one can use the strong, stiff and relatively brittle thermosets (e.g., epoxy [48,57,71], phenol-formaldehyde [53], etc.) or the relatively ductile, yet tougher thermoplastics (e.g., PPS [45,46], vinylester [62], poly(methylvinylsiloxane) [65], PMMA [66,67], PBO [70], PEEK, PES, polycarbonate [73], PAEK [75], etc.). In addition, one can also adopt practically any process commonly used for polymer composite manufacturing, e.g., compression molding, vacuum bag/autoclave, pultrusion, filament winding, etc. to manufacture hybrid polymer composites [76-79]. Furthermore the concept of hybrid composite has gone beyond the realm of conventional polymer composites. Hybrid metal-polymer laminates, called fiber metal laminates (FMLs), have been widely used in aerospace industry [80-82]. Song et al. [83] reported investigation of hybrid metal matrix composites (MMCs). Some recent efforts were geared toward the studies of functionally gradient hybrid composites [84] and smart hybrid composites incorporating shape memory alloys (SMAs) [85-88]. One of the goals of manufacturing smart hybrid composites is to develop a material system with self-diagnosing function for preventing fatal fracture [89].

In practice, hybrid composites with two types of fibers are most useful and cost-effective. For instance, the inexpensive E-glass fibers may be used to mingle with the relatively costly carbon/graphite or aramid fibers. Carbon/graphite fibers are chosen for their low density, high specific strength and high specific modulus. On the other hand, aramid fibers provide low density, high impact and fatigue strength. However aramid has a relatively lower specific compressive strength [41].

Intuitively we can extend the concept of linear Rule of Mixtures for a single-fiber composite:

$$E_c = v_f E_f + v_m E_m$$

where E_c, E_f, E_m are the thermomechanical properties of interest of the composite, fiber, and matrix, respectively, and v_f, v_m are the fiber and matrix volume fractions, respectively, to the Rule of Hybrid Mixtures (RoHM) of a hybrid composite:

$$E_{hc} = v_{f1} E_{f1} + v_{f2} E_{f2} + v_m E_m$$

where E_{hc}, E_{fi}, v_{fi} ($i = 1,2$) are the thermomechanical properties of the hybrid composite, constituent fibers, and the volume fractions of the constituent fibers, respectively. However, it has been reported widely that many hybrid composites show a synergistic effect, called hybridization, which causes the resultant thermomechanical property to deviate from the linear RoHM [40,90-94]. We call the deviation positive *or* negative hybridization, depending on the relative value of a thermomechanical property of a hybrid composite with respect to the hypothetical linear RoHM. One of the requisites for the occurrence of hybridization effect is that the two types of fibers differ in mechanical properties and the interfaces they form with the matrix are also not the same [63].

With hybridization, it is possible to design a composite material system to better suit various requirements. For instance, since the mechanical properties of glass and carbon fibers and the interfacial properties of a glass-fiber-reinforced polymer and a carbon-fiber-reinforced polymer differ greatly, the hybridization effect would very likely exist for their hybrid composites. For example, the fracture energy and compression modulus of Type B hybrid

glass/carbon/epoxy composites was observed to show a negative hybridization effect [93,95]. However, if the Type A hybrid composite is formed, i.e., incorporating both glass and carbon fibers into a single matrix, one would lead to better properties than those expected from the RoHM [40]. Several researchers found the hybrid effects of the tensile modulus and the strain at failure of glass-rich hybrids [90,92,95] to be positive. As interpreted by Zweben [92], on micromechanical level the high elongation glass fibers in the hybrid composite behave like crack arrestors hindering cracks to propagate through the composite. Thus, the strain level required to fail the hybrid composite is enhanced, resulting in a positive synergistic effect due to hybridization. Similar positive hybridization effect has also been reported for woven fabric hybrid composites [54,55,96,97].

In spite of the freedom of tailoring hybrid composites and gaining positive hybridization to meet design requirements, effects of such enhancements may be offset when one considers problems related to thick-section composites. For instance, due to difference in thermal expansion coefficients of fibers and resin, thermal mismatch is already a concern in thin hybrid composites [43]. This problem, as well as other issues (e.g., fiber waviness) would be even more severe when thick-section composites are considered. Since the majority of applications of thick-section composites are for military use, temperature rise in armor-grade hybrid fiber composites during ballistic impact and projectile penetration should be carefully accounted for [98,99]. Unfortunately, the literature available for thick-section hybrid composites is very meager [44,45]. It is practically non-existent for thick-section interwoven hybrid composites.

3.4: Composite joints

With only a few exceptions the joints in a composite structure usually determine the overall strength of that structure because more often than not one of the joints will become the weakest part of the structure. Open literature on joining of single-fiber composites by either mechanical fastening (bolted, pinned, or riveted), adhesive-bonding, or the combined bonding-mechanical-fastening is abundant (see Ref. [33-36,100]). In a nutshell [36,101], the advantages of a mechanical joint are:

- tolerance to the effects of environment and fatigue loading
- ease of inspection
- capability of repeated assembly
- higher reliability
- no special surface preparation required

However, it requires a hole to be drilled, which causes unavoidable stress concentrations as well as a weight penalty due to the addition of the bolt to the composite. On the other hand, the advantages of a bonded joint are:

- high strength/weight ratio of the joint region
- low part count
- no strength degradation due to cutouts
- potential corrosion problems minimized
- larger area for load distribution (with little or no stress concentration)

However, it requires careful surface treatment of the adherend, may be affected by severe environment, and is difficult to dismantle for inspection.

It is well known that for a thick-section composite load transfer through bolted joins is more practical since the bearing action of the bolt and the shearing action of the clamps would be sufficient if the joint is designed correctly. On the other hand, adhesively-bonded joints are mainly for thin-laminate composites. As cited by Dvorak et al. [102], in order to transfer load properly, the recommended overlap length for a double lap joint is 46t to 60t, where t is the laminate thickness. This will result in an impractical joint length for thick-section composites, which has a thickness t at least 0.5"). A more serious problem results from the often low interlaminar shear strength of the top plies, which may cause initial joint failure not by adhesive failure but by delamination of the surface plies. Once the outer plies are delaminated, stress concentrations will occur at these isolated plies, causing lamina-pullout since a significant portion of service load is now taken by these isolated, delaminated outer plies. Hence, the original design idea of increasing composite thickness to support higher load would not work. The problem may be alleviated but not eliminated entirely by distributing the adhered surface through the thickness of the adherends in stepped-lap joints [103-105] or tongue-and-groove joints [102,106]. In either design the end sections of adherends need to be machined into steps or grooves first, which not only will cost more in the manufacturing/repair process, but also will induce stress concentrations; thus offsetting the merit of re-distributing loading through the thickness.

Another point of concern is the severe working conditions under which a military ground vehicle is expected to perform. An adhesively-fastened joint may reach its glass transition temperature due to temperature rise from repeated loading or working under higher temperature conditions. Above its glass transition temperature an adhesive may show viscoelastic or viscoplastic behavior. Large deformation due to creep in the adhesive joint may ensue, thus defeating the purpose of fastening. To prevent this, one of the proposers suggested a remedy by adding a bolt as the back up to hold the adherends in place in case of adhesive failure [104,105]. Since it is a secondary fastening mechanism, the required bolt size will be smaller and may result in lighter stress concentrations.

So far, there is very little data available on using a combination of reinforcement, such as glass, graphite, and Kevlar, to make hybrid composite joints [101,107]. Open literature on thick-section hybrid composite joints, to the best of proposers' knowledge, is still non existent. With the flexibility of selecting reinforcing fibers and the possibility of positive hybrid effects, one may be able to design a hybrid thick-section composite joint optimized for impact strength and damage resistance so that better designed Army combat vehicles, such as the FCS, may become a reality.

3.5: Impact damage in composites

Impact of solid projectiles on a composite structure may result in substantial damage and significantly reduce the usefulness of the structure. Conventionally, we characterize impact damage into two classes: *low-velocity* (i.e., *non-penetrating*) impact damage and *ballistic* (i.e., *penetrating*) impact damage [3]. As its name implies, the non-penetrating, low-velocity impact mainly causes internal, invisible damage. In practice, low-energy, non-penetrating impact may occur when a larger object (such as a tool) is accidentally dropped onto a composite structure. On the other hand, ballistic impact occurs when a solid object impinges at a composite structure at a high velocity, causing deep penetration, perforation, and/or spalling fragmentation.

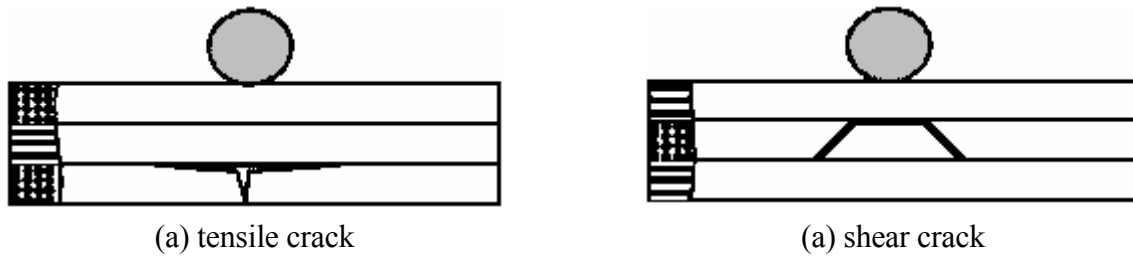(a) tensile crack   (a) shear crack

Figure 3.5-1. Two basic types of matrix cracks [3].

As soon as the impactor contacts the target, a complex wave pattern, including possibly a compressive P-wave, shear SH- and SV-waves, and surface Rayleigh and Love waves, immediately ensues [108]. The material behind a compressive wave is, in general, in a tensile state. When reflected from a boundary (such as the back face of the target plate), the compressive wave may change into an expanding (i.e., tensile) wave. After being amplified by the oscillatory motion of the target plate, these waves may generate tensile and/or shear cracks (see Fig. 3.5-1) in matrix [109,110]. In general, due to bending motion of the target plate, which creates compression near impact site while tension at the opposite side of the plate, shear cracks frequently occur right underneath the impact site whereas tensile cracks develop at the opposite side of impact.

Once these matrix cracks are formed, regardless which type, they often deflect at the interface of laminae of different orientations to form delamination [110,111]. Experimental studies consistently reported that no delamination was observed between two adjacent plies having the same fiber orientation. It is also interesting to note that when impacted from top, the delaminated area (which occurs at interfaces between plies of different fiber directions) has an oblong or "peanut" shape, as illustrated schematically in Fig. 3.5-2, with its major axis being oriented along the fiber direction of the lower ply at that interface.
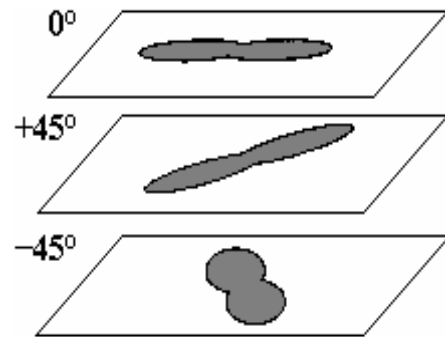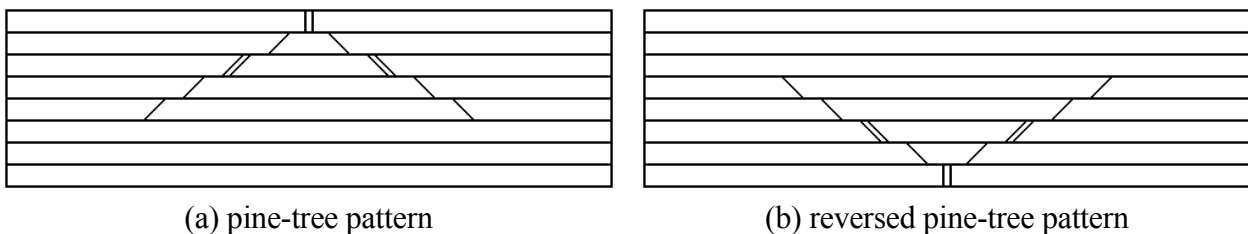

Figure 3.5-2. Orientation of delamination

(a) pine-tree pattern   (b) reversed pine-tree pattern

Figure 3.5-3. Typical sectional views of damage pattern in a composite [3].

Depending on the flexural rigidity of the target plate, two basic modes of damage patterns have been reported [112]. For a stiff thick composite block subjected to impact, a pine-tree damage pattern, as shown in Fig. 3.5-3(a), may develop; whereas low-velocity impact on a flexible thin composite panel may result in a reversed pine-tree damage pattern, as depicted in Fig. 3.5-3(b). Bending stiffness mismatch has been attributed to as the main factor causing these two damage patterns [113]. Experimental evidence (e.g., [114]) shows that once more severe damage types,

such as, debonding along fiber-matrix interface, fiber pullout, and fiber breakage, etc., occur, the target plate will suffer extensive damage, rendering the composite irreparable.

Various apparatus have been developed to simulate low velocity impact tests. The most common type is the drop-weight tester [115,116], which generates impact velocity by dropping the impactor from a given height. The impact velocity produced by this method is usually low (in an order of 10 m/s). For instance, using Newton's second law, one can quickly estimate that a gravity-driven drop from a height of 5 m will achieve a maximum impact velocity of merely 9.9 m/s. High velocity impacts (in an order of 1,000 m/s) are, in general, achieved by shooting the projectile from a gas gun [117]. In addition to impact velocity, other important parameters deserving consideration include: the impactor's mass (which, in conjunction with the impact velocity, constitutes the impact energy), shape, elastic properties, the incidence angle, the target's material properties [114], lay-up configuration [114,118], stitching [119,120], tension preload (i.e., initial stress) [121], environmental conditions [122,123], etc. For instance, as summarized in a comprehensive review by Abrate [3], impact damage resistance can be increased by:

- Using toughened epoxy or thermoplastic as the matrix material,
- Introducing "interleaving", i.e., discrete layers of very tough, very ductile resin inserted at certain interfaces,
- Making the fiber-matrix interface more "rubbery" rather than "glassy" (this is particularly useful for composites reinforced by glass fibers),
- Adopting woven or stitched (instead of unidirectional) laminates (to improve through-the-thickness stiffness, thus reducing bending stiffness mis-matching),
- Applying initial tension (to make the target plate more difficult to bend).

Due to its inherent complexity, attempt to reconstruct the entire sequence of impact-damage events in a composite, if not impossible, can be very difficult. To obtain solutions, very often one needs to make drastic compromises, i.e., by adopting great approximations. For instance, results from quasi-static indentation analyses [124,125] have been widely used to estimate time histories of impact force and contact area. The results were used, in turn, to determine the onset and extent of damage [126]. By incorporating appropriate strength-theory-based failure criteria and fracture-mechanics-based crack propagation criteria [127-131] into three-dimensional stress analyses (often through finite element codes), the final extent of damage site, especially the delamination area, may be evaluated. This approach in general involves extensive computations and has been limited to simple lay-up configurations, e.g., symmetric cross-ply laminates. Numerical simulations of high-velocity impact phenomena in three-dimensional thick-section composites is still non-existence [6]. Most of previous work on numerical modeling on high-velocity impact was mainly limited to two-dimension simulations [132]. The available three-dimensional numerical simulation codes [133] are for either homogeneous materials (e.g., monolithic ceramics) or bi-materilas (e.g., ceramic/metal armors) [134-137].

Post-impact studies of composites usually involve:

- Non-destructive evaluation of damage extent, especially the delamination area, using X-ray radiographic [110] and/or ultrasonic [111] techniques,
- Estimating residual properties, especially the compressive-after-impact (CAI) strength [138] and compressive-after-ballistic impact (CABI) strength [6], residual tensile [139] and flexural [140] strength, stiffness, and ductility, residual buckling stability [141], etc.

Compared to impact on traditional single-fiber unidirectional composites, studies on the effects of impact loading on woven composites [142-146], stitched composites [147-149], composite joints [150-153], and hybrid composites [46-48,57,62,79,154] are still very few. It should also be pointed out that when a material is subject to high-velocity impact, its property may change due to the effect of high strain rate and temperature resulting from during penetration and severe deformation [155-157].

4.   Research Results

4.1: Materials

The main goal of the proposed research is to investigate damage caused by low-velocity and ballistic-speed impact in thick-section hybrid composite joints and the ensuing issue of damage tolerance. After reviewing available literature [6,119-120,142-149,158-165] and considering Army's need for ground combat vehicle applications and the capabilities of the laboratories at CCNY and U.S. Army TACOM, we would like to propose for this project the choice of 1/4" composites (approximately 24 layers) made of toughened epoxy (cured at 350°F, instead of 250°F) reinforced by carbon/S2 glass interwoven stitched fabrics. S2 glass fiber-reinforced toughened epoxy has been proven to be a viable material for the Composite Armored Vehicle demonstrator program. Previously the proposers had investigated the thermomechanical behaviors of this material through a contract from U.S. Army TACOM. (Contract No. DAAE07-96-C-X-121, 04/09/1996-06/30/1999).

The selection of interwoven fabric composites with through thickness stitching should increase the out-of-plane bending rigidity and reduce, if not fully eliminate, delamination during impact. We also would like to suggest using vacuum-assisted resin-transfer molding (VARTM) to manufacture the hybrid composites since using the VARTM technique will allow us to design the preform easily, which is a feature very desirable for hybrid composite manufacturing [166]. However we are fully aware of the existence of a new process, called co-injection resin-transfer molding (CIRTM), which was developed by Army Research Laboratory, University of Delaware, and the CAV/Crusader composite structure contractor, United Defense Limited Partnership (UDLP) [2,6,167]. If the technique is available to us, we would like to use it to make specimens. For either manufacturing process, great care should be taken during preform preparation to reduce, if not fully avoid, fabric warping due to fiber crimping and fiber breakage due to stitching. Another important factor, stacking (lay-up) sequence, should be carefully evaluated [69,118].

After careful evaluation, the vendor, EDO Fiber Innovations, was selected to manufacture both strip- and panel-types of composite specimens for the project. Per recommendation from TACOM-TARDEC engineers, the composites are made of API SC-79 epoxy resin reinforced by fabrics, which are made of either IM-7 graphite (i.e., carbon) fibers, or S-2 glass fibers, or the hybrid of these two. All fabrics are crimped 0/90 degree, plain-weave woven, with a weight of 10-12 oz/sq yd and a 6K tow size. The fiber volume fraction is around 55%. A resin tackifier was used prior to the VARTM molding operation with a curing temperature around 350°F.

4.2: Static tests

Quasi-static tensile tests of 1/4" thick composite strip specimens were tested at CCNY in a 22-kip MTS 810 universal testing machines equipped with an environmental chamber (Fig. 4.2-1). The complete load and displacement curves were recorded using National Instruments LabVIEW and DAQ data acquisition system. Strain gage technique were used to verify the recorded displacement data and to evaluate the Poisson's ratios.


Figure 4.2-1.   The MTS machine with an environmental chamber.

Woven composite strip specimens with four different lay-ups were tested under uniaxial tension. The four lay-up configurations are: all S2-glass fiber reinforced (called GL), all IM-7 graphite fiber reinforced (called GR), symmetric hybrid S2-glass outside and IM-7 graphite inside reinforced (called GL-GR-GR-GL), and symmetric hybrid IM-7 graphite outside and S2-glass inside reinforced (called GR-GL-GL-GR). Due to the woven fiber structure, the transverse modulus (i.e., along the warp direction, called the 2-axis) of the composites was assumed to be the same as the longitudinal modulus (i.e., along the fill direction, called the 1-axis). Thus, tensile tests for transverse direction were not carried out. For each lay-up configuration, eight tests were conducted: four along the fill direction (i.e., a 0/90 plain-weave woven composite) for measuring the E_1 and E_2 Young's moduli and four inclined by 45° (called x-axis) with respect to the fill direction (i.e., a ±45 plain-weave woven composite) for measuring the E_x (therefore the shear modulus G_{12}). Figure 4.2-2(a) shows the longitudinal stress-strain relation along the fill direction of GL specimens with error bars indicating the spread of data deviation. Even though each test did not exhibit identical result, similar trend for all these tests was observed. Each curve has a linear portion corresponding to the undamaged state, followed by a second linear portion with a smaller angle of slope. Figure 4.2-2(b) shows the typical optical pictures taken at different strain levels during the test. As shown in Fig. 4.2-2(a), the curve is almost linear and failure at around 426 MPa. As shown in Fig. 4.2-3, the measured Poisson's

ratios for these S2-glass fiber-reinforced composites are: $\nu_{12} = 0.1621$ and $\nu_{13} = 0.4134$, respectively.

Figure 4.2-4(a) shows the in-plane shear stress-strain relation of GL specimens with error bars indicating the spread of data deviation; whereas, Figure 4.2-4(b) shows the typical optical pictures taken at different strain levels during the test. As shown in Fig. 4.2-3(a), the curve is linear initially, followed by an appreciable nonlinear portion, and failure at around 180 MPa. Finally, Figures 4.2-5 and 4.2-6 show the longitudinal stress-strain relation along the fill direction and the shear stress-strain relation of GR specimens with error bars indicating the spread of data deviation. The curve shows a linear portion failed at around 600 MPa for the longitudinal case and at around 185 MPa for the shear case. As shown in Fig. 4.2-7, the measured Poisson's ratios for these IM7-graphite fiber-reinforced composites are: $\nu_{12} = 0.0202$ and $\nu_{13} = 0.4634$, respectively.
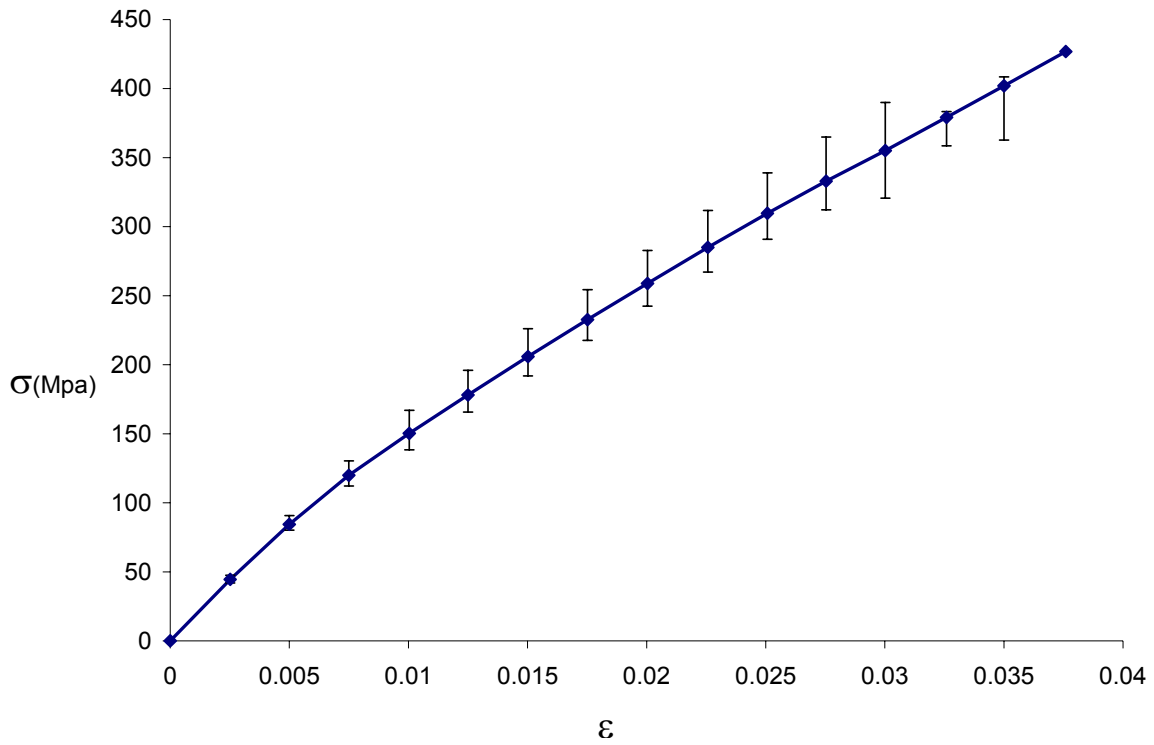
$E_1 = E_2 = 17.047$ GPa $\qquad \sigma_{max} = 426$ MPa $\qquad \varepsilon_{max} = 0.0376$

Figure 4.2-2(a) Tensile-induced damaged longitudinal stress-strain curves for 0/90 plain-weave woven composite GL specimens.

$\varepsilon = 0$ $\qquad$ 0.008 $\qquad$ 0.016 $\qquad$ 0.024 $\qquad$ 0.032 $\qquad$ 0.038
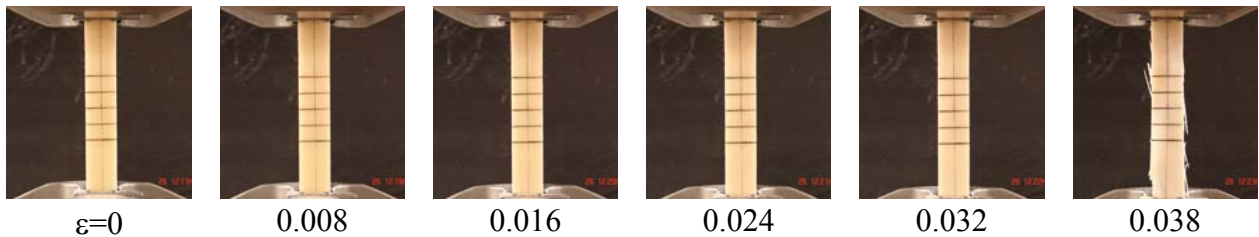
Figure 4.2-2(b) Optical pictures of a 0/90 plain-weave woven composite GL specimen taken during tensile testing at different strain levels.
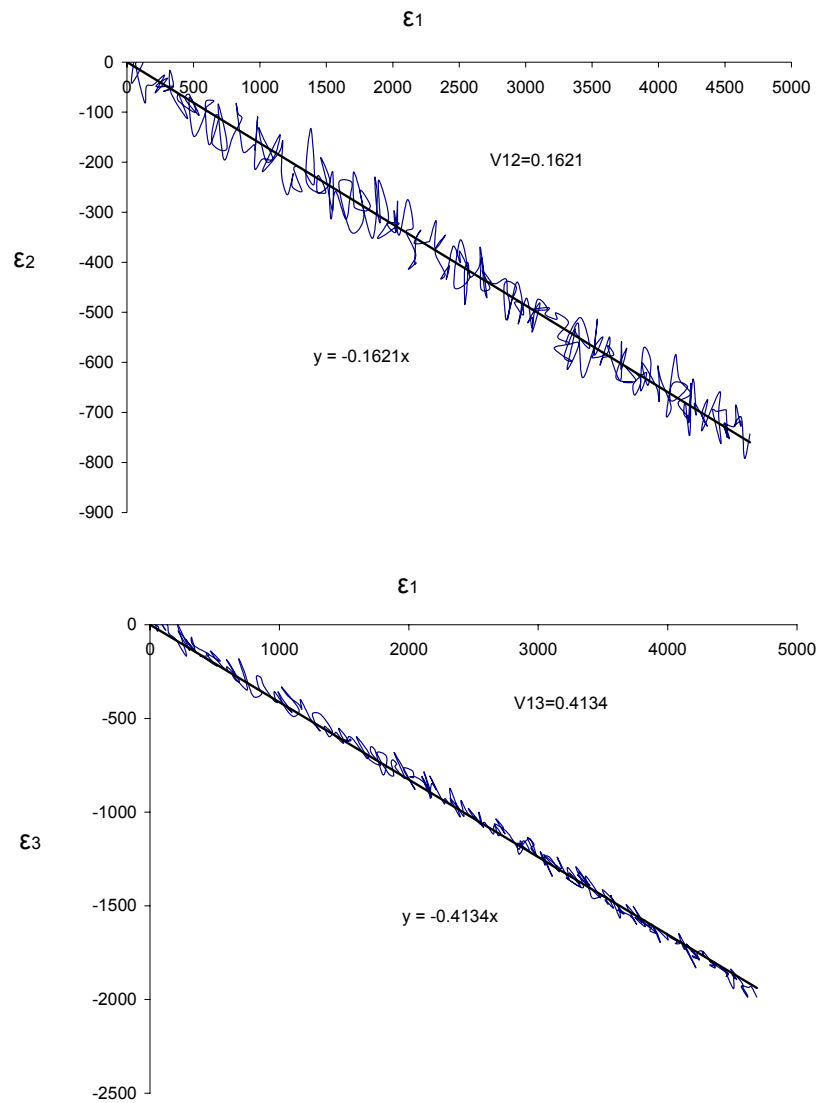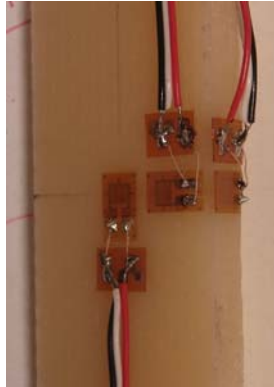
Figure 4.2-3   The measured Poisson's ratios of the 0/90 plain-weave woven composite GL specimens.
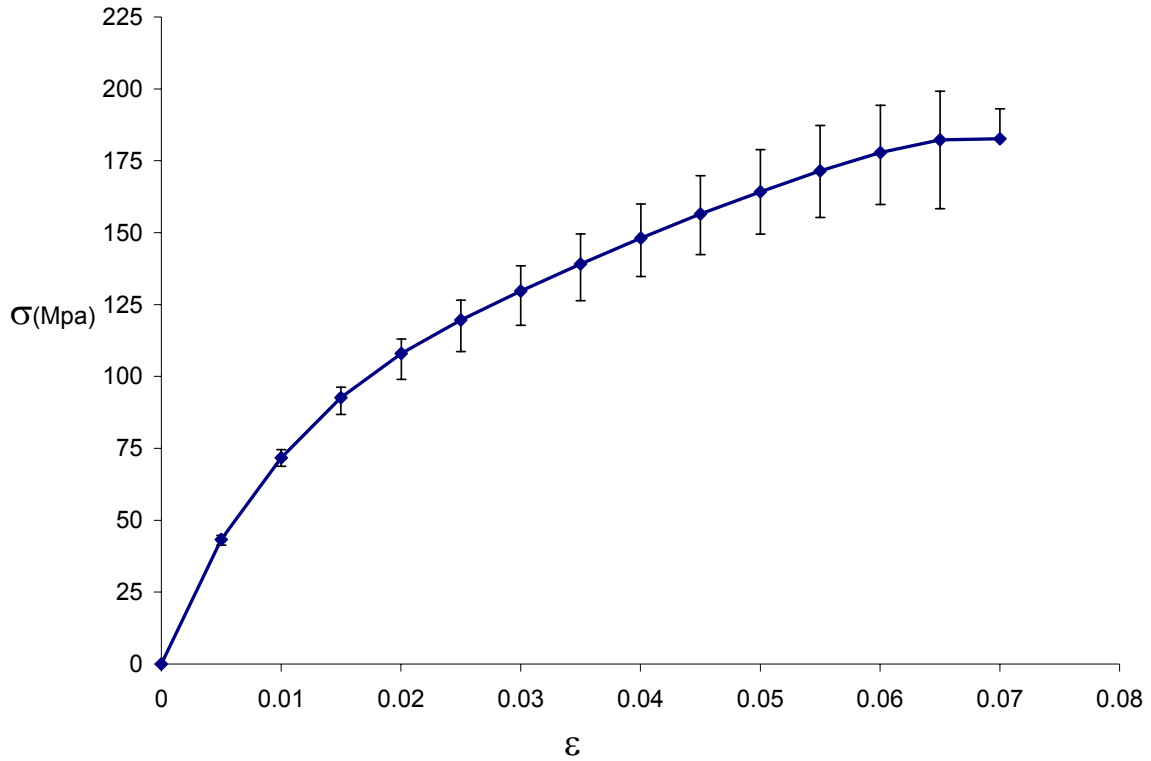
E_x = 8.667 GPa G_{12} = 10.43 GPa σ_{max} = 180 MPa ε_{max} = 0.07

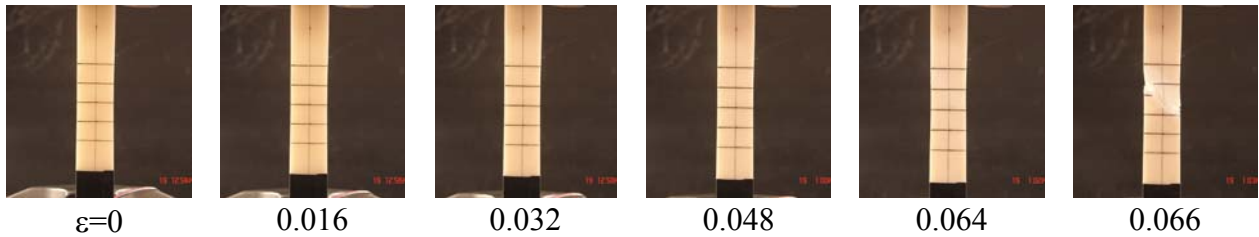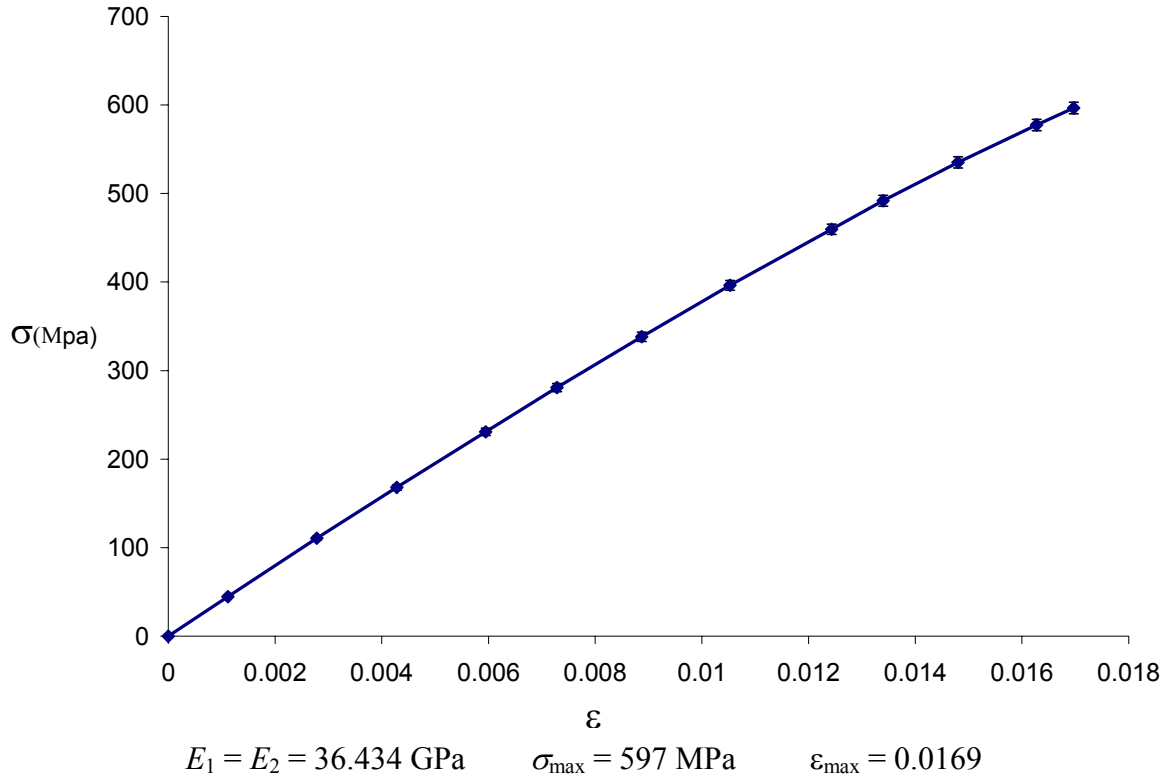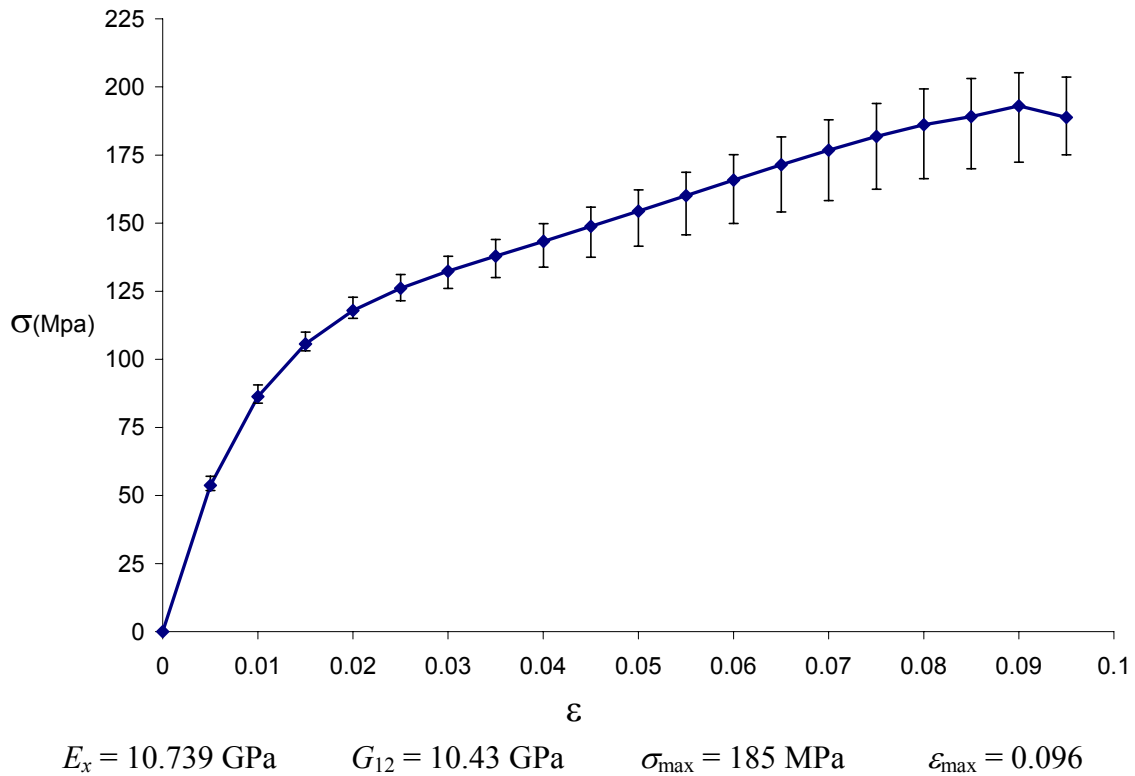Figure 4.2-4(a)   Tensile-induced damaged shear stress-strain curves for ±45 plain-weave woven composite GL specimens.

| ε=0 | 0.016 | 0.032 | 0.048 | 0.064 | 0.066 |

Figure 4.2-4(b)   Optical pictures of a ±45 plain-weave woven composite GL specimen taken during tensile testing at different strain levels.

The hybrid GR-GL-GL-GR composite's longitudinal stress strain curves had three stages: a linear behavior at the beginning, followed by a second linear portion with a smaller angle of slope. During the third stage, the graphite part in the hybrid specimen was fractured first and the stress was dropped to 100 MPa. However, the glass part in the hybrid composite was still undamaged. Thus, the stress increased linearly up to 180 MPa until the glass part in the hybrid specimen fractured. Figure 4.2-8(a) shows the stress strain relations of the GR-GL-GL-GR specimen. Optical pictures of the same test are shown in Figure 4.2-8(b). Optical pictures clearly show that graphite part fractured first (ε=0.032) and the glass part fractured later (ε=0.041).

$$E_1 = E_2 = 36.434 \text{ GPa} \qquad \sigma_{max} = 597 \text{ MPa} \qquad \varepsilon_{max} = 0.0169$$

Figure 4.2-5   Tensile-induced damaged longitudinal stress-strain curves for 0/90 plain-weave woven composite GR specimens.
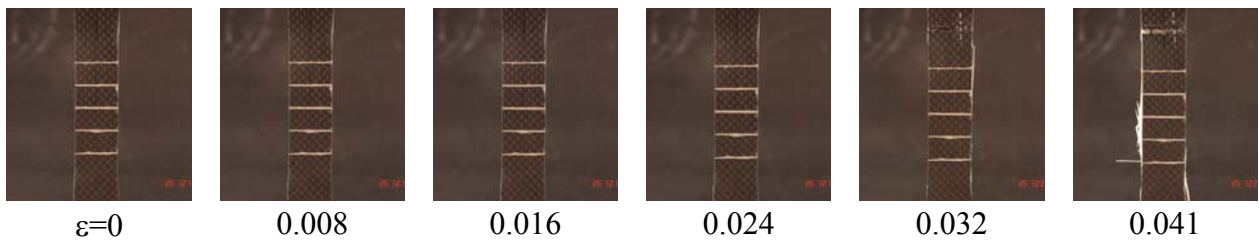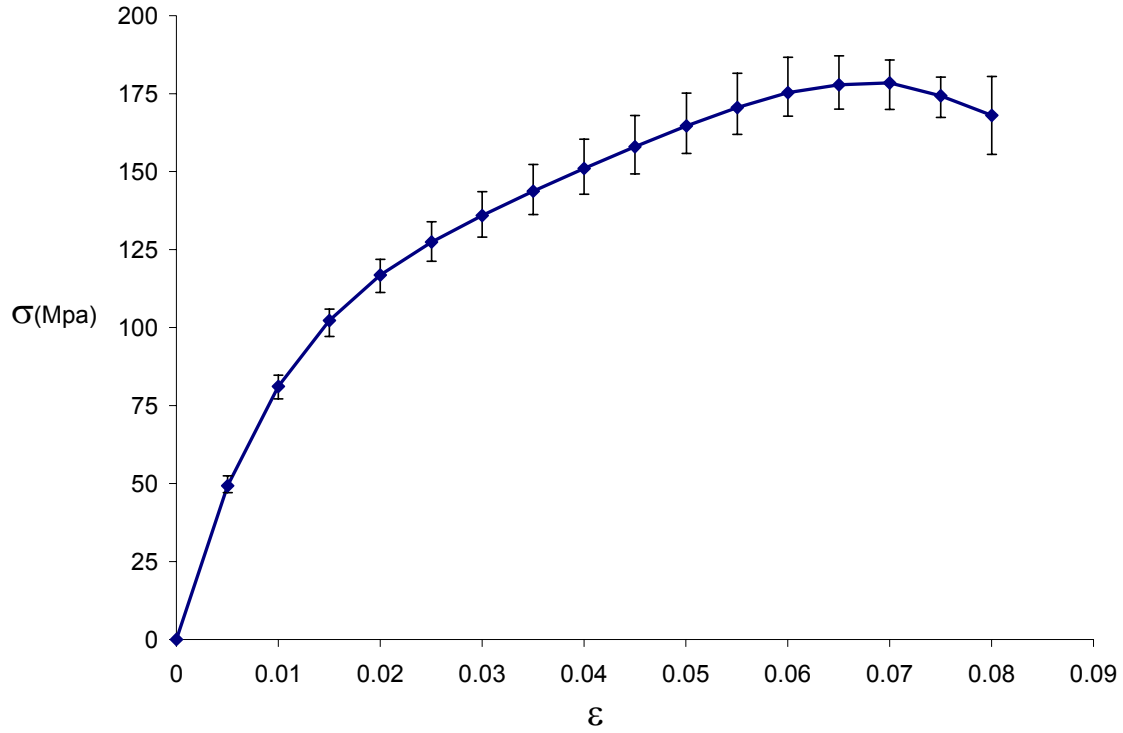

$$E_x = 10.739 \text{ GPa} \qquad G_{12} = 10.43 \text{ GPa} \qquad \sigma_{max} = 185 \text{ MPa} \qquad \varepsilon_{max} = 0.096$$

Figure 4.2-6   Tensile-induced damaged shear stress-strain curves for ±45 plain-weave woven composite GR specimens.
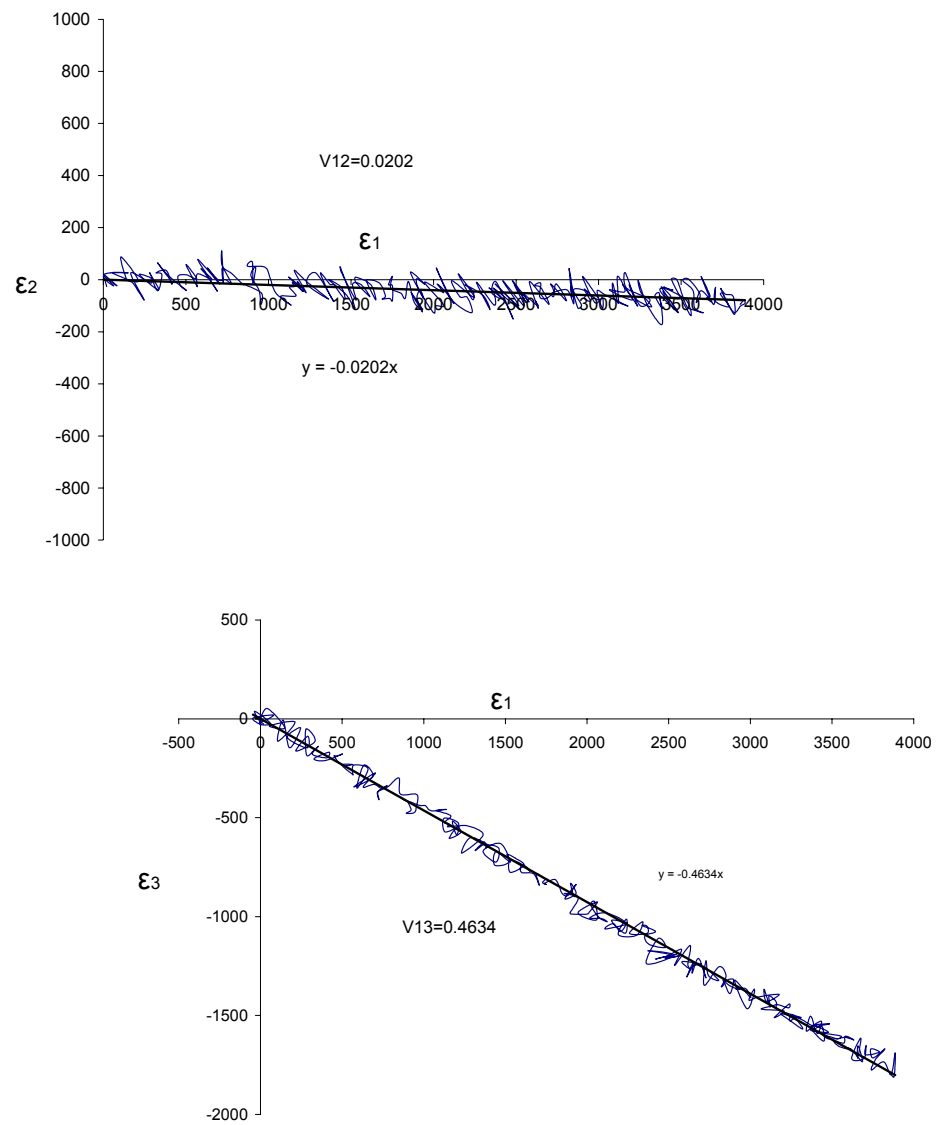
Figure 4.2-7 The measured Poisson's ratios of the 0/90 plain-weave woven composite GR specimens.

On the other hand, the two-stage stress-strain failure was not observed for shear tests of hybrid specimens. Shear tests exhibit a linear portion at the beginning followed by a second linear portion with smaller slope. Graphite and glass failed together. The shear stress-strain relations of GR-GL-GL-GR specimen and optical pictures taken during the test are shown in Fig.4.2-9. Finally, the behaviors of hybrid GL-GR-GR-GL specimens were similar to the hybrid GR-GL-GL-GR specimens. The longitudinal and shear stress strain relation are shown in Figs 4.2-10 and 4.2-11, respectively.
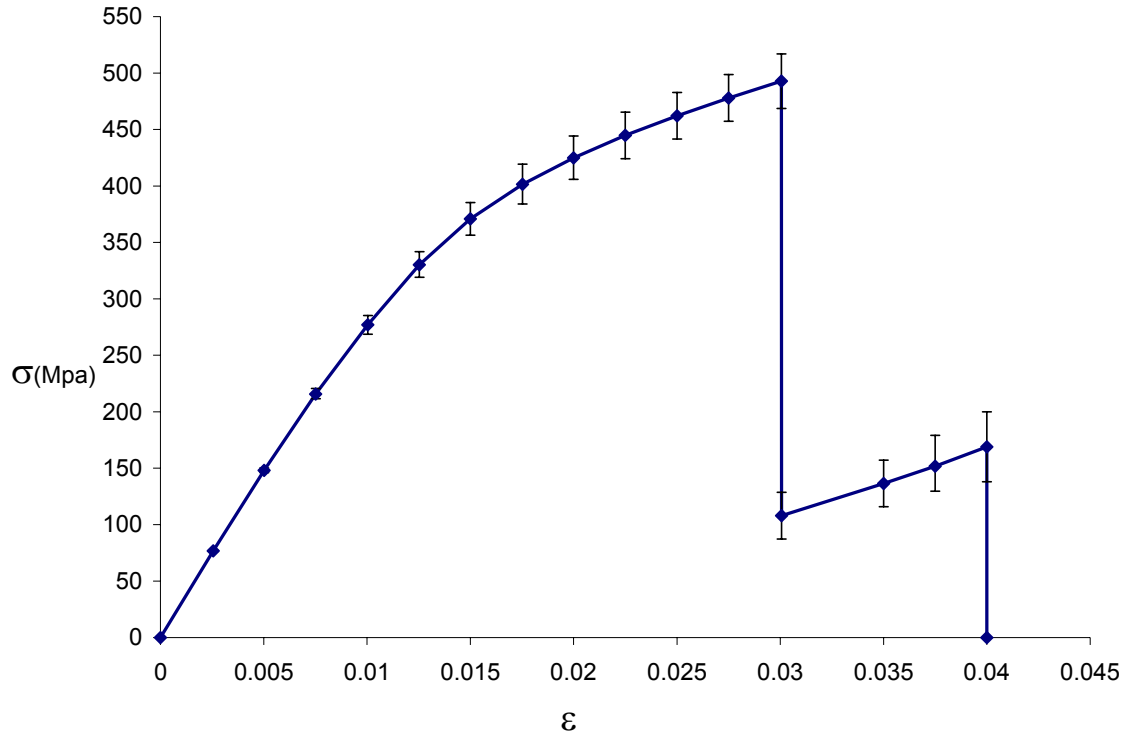
$E_1 = E_2 = 29.036$ GPa $\sigma_{max} = 493$ MPa $\varepsilon_{max} = 0.03$

Figure 4.2-8(a)   Tensile-induced damaged longitudinal stress-strain curves for 0/90 plain-weave woven composite symmetric GR-GL-GL-GR specimens.

$\varepsilon=0$ 0.008   0.016   0.024   0.032   0.041

Figure 4.2-8(b)   Optical pictures of a 0/90 plain-weave woven composite symmetric GR-GL-GL-GR specimen taken during tensile testing at different strain levels.
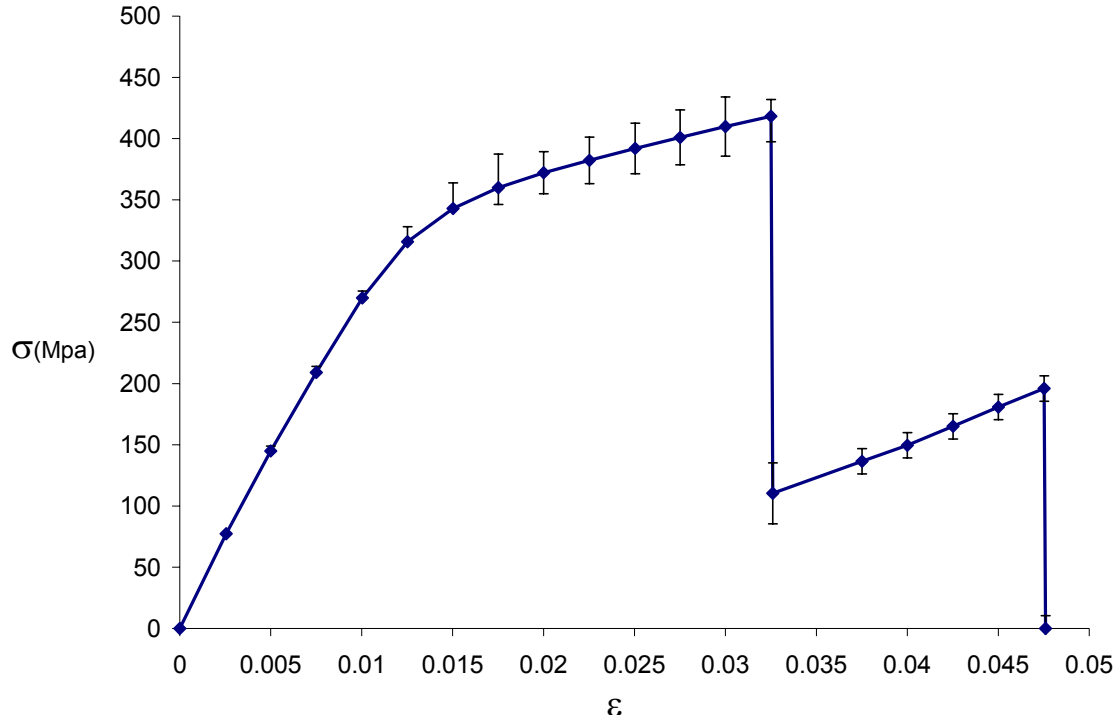
$E_x = 9.793$ GPa $\qquad G_{12} = 10.43$ GPa $\qquad \sigma_{max} = 175$ MPa $\qquad \varepsilon_{max} = 0.08$

Figure 4.2-9(a) Tensile-induced damaged shear stress-strain curves for ±45 plain-weave woven composite symmetric GR-GL-GL-GR specimens.
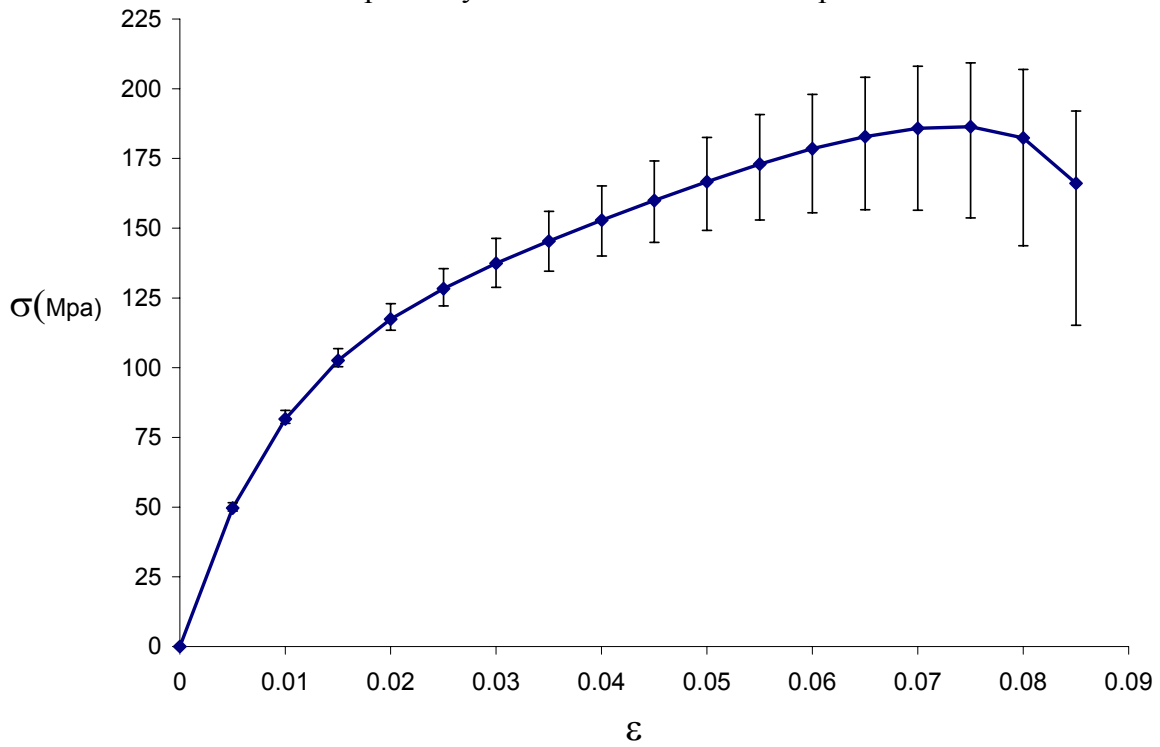

$\varepsilon=0$ $\qquad$ 0.024 $\qquad$ 0.048 $\qquad$ 0.072 $\qquad$ 0.089

Figure 4.2-9(b) Optical pictures of a ±45 plain-weave woven composite symmetric GR-GL-GL-GR specimen taken during tensile testing at different strain levels.

$$E_1 = E_2 = 27.582 \text{ GPa} \qquad \sigma_{max} = 418 \text{ MPa} \qquad \varepsilon_{max} = 0.0325$$

Figure 4.2-10   Tensile-induced damaged longitudinal stress-strain curves for 0/90 plain-weave woven composite symmetric GL-GR-GR-GL specimens.

$$E_x = 9.938 \text{ GPa} \qquad G_{12} = 10.43 \text{ GPa} \qquad \sigma_{max} = 185 \text{ MPa} \qquad \varepsilon_{max} = 0.085$$

Figure 4.2-11   Tensile-induced damaged shear stress-strain curves for ±45 plain-weave woven composite symmetric GL-GR-GR-GL specimens.

<u>4.3: Drop-weight impact tests of S2-glass fiber reinforced toughened epoxy composites</u>

Because of their high specific strength and stiffness, composite materials have been adopted for various beam-type load-bearing structures for several decades [168]. Recently these high strength, high stiffness and low density composites had found beam-type structural applications under high loading rates, such as drive-shafts of automotives, rotor blades of helicopters, intake fan blades of jet engines, or even an entire composite wing of a space craft [169-171]. The damage tolerance of a composite used for this class of applications depends greatly on the impact-resistance capability of the material. When designing a composite beam, we often treat it as a 1-D linearly-elastic member and pay attention only to the axial stress/strain induced by the flexural deformation. However, once a composite beam is damaged, no matter what the source of defect is (e.g., delamination, matrix cracking, fiber breakage, fiber-matrix debonding, etc.), the 1-D nature, in general, is no longer preserved and the damaged structural member should be treated in the more complicated 3-D manner, including nonlinear elasticity and anisotropy induced by damage [171,172]. Furthermore, in order to achieve significant reduction in cost and weight, advanced technologies such as stitching, braiding and knitting had recently been employed to form 3-D composites [173-175]. Hence the study of structural behaviors of composite beams requires rigorous analyses based on the more realistic 3-D nonlinear anisotropic constitutive laws. In this study, a combined experimental and 3-D dynamic nonlinear finite element approach was adopted to study composite beams subject to drop-weight or ballistic impact.

Experimental procedures

Composite panels made of toughened epoxy (i.e., cured at 350°F) reinforced by uni-directional S2 glass fibers (44% fiber volume fraction) were first machined into simple strip or dog-bone beam specimens. The panels had 24 layers (approximately 6.35 mm) of laminae, which were stacked with different lay-up configurations:

1) **uni-directional**: $\left[0^{\circ} \right]_{24}$

2) **cross-ply**: $\left[0^{\circ}_{3} / 90^{\circ}_{3} \right]_{2S}$, $\left[0^{\circ}_{2} / 90^{\circ}_{2} \right]_{3S}$ or $\left[90^{\circ}_{2} / 0^{\circ}_{2} \right]_{3S}$

3) **quasi-isotropic**: $\left[0^{\circ}_{3} / 45^{\circ}_{3} / 90^{\circ}_{3} / -45^{\circ}_{3} \right]_{S}$ or $\left[90^{\circ}_{3} / 45^{\circ}_{3} / 0^{\circ}_{3} / -45^{\circ}_{3} \right]_{S}$

The first part of the experimental program involved low-velocity impact tests, which were conducted using an Instron-Dynatup 8250 pneumatic-assisted, instrumented drop-weight impact testerequipped with a pneumatic break to avoid multiple strikes (Fig. 4.3-1). As shown in Fig. 4.3-2, a 6.35mm thick dog bone specimen of 254 mm in length, 25.4 mm in width at both ends and tapered down to 12.7 mm in the mid-section was clamped circumferentially in the specimen fixture of the drop-weight impact tester along a circle of a diameter of 76.2 mm measured from the center of the specimen. In addition, two strain gages were mounted on the front and back faces of the specimen, respectively, at a distance of 12.7 mm away from center.

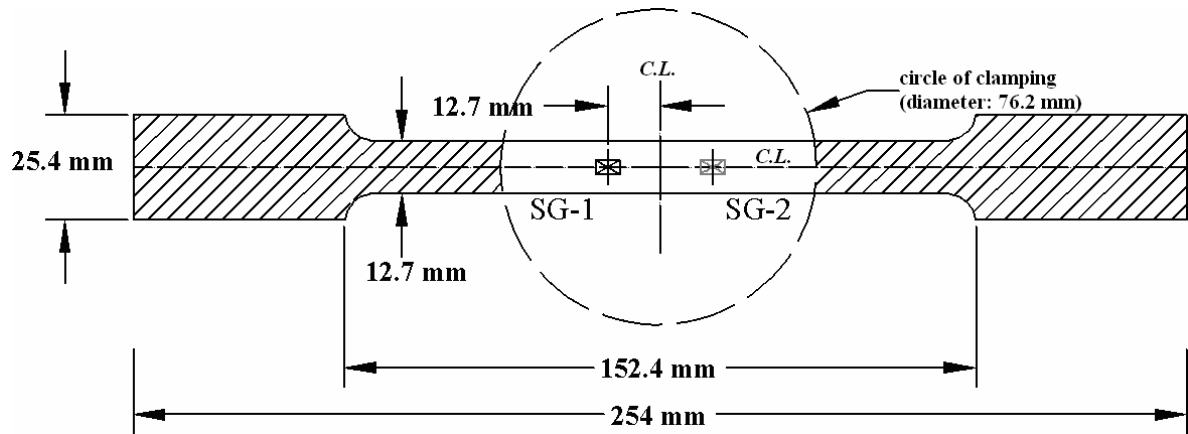Figure 4.3-1.   The drop-weight impact machine.

Figure 4.3-2.   Strain-gage mounted dog-bone composite beam specimen
for drop-weight impact test.

The specimens, as shown in Fig. 4.3-3, were then impacted by a Charpy-type straight-line impactor with different impact velocities, V_o. Table 4.3-1 lists the specimen stacking sequences and the impact velocities of a 5.1 kg hemi-spherical drop-weight tup for five drop-weight tests. For each drop-weight test, the impact velocity and the time-histories of impact force and strains were recorded. It should be pointed out that because of the high levels of strains generated during the drop-weight impact event, only one out of the five tests the strain gage mounted on the tension side survived (i.e., SG-2 on the bottom face in Fig. 4.3-2). On the other hand, we always recorded successfully the strain histories in SG-1, which was mounted on the top face in Fig. 4.3-2.
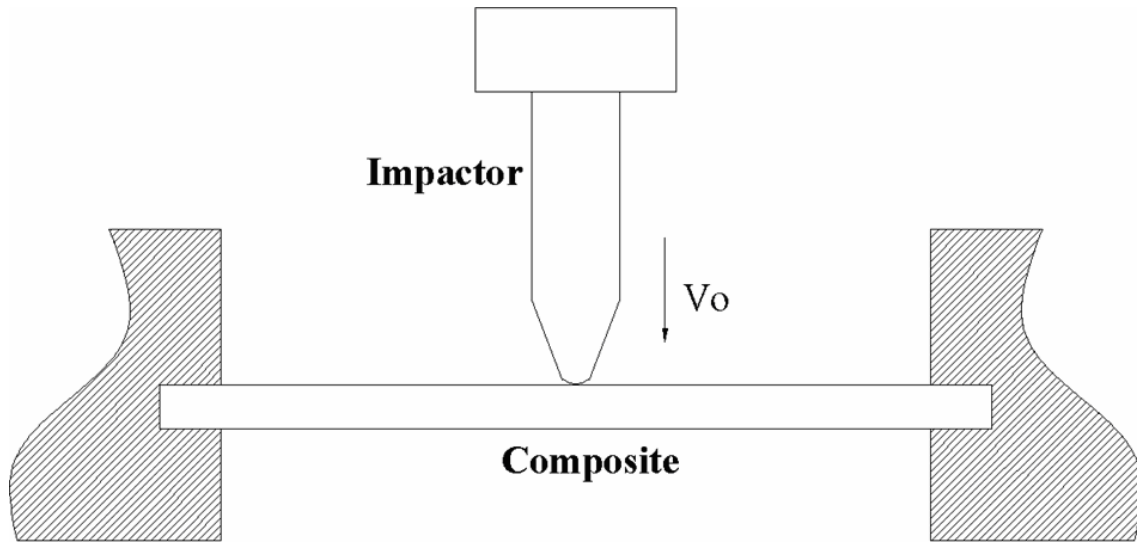
Figure 4.3-3.   Schematic diagram of the set-up for drop-weight impact tests.

Table 4.3-1.   Parameters of drop-weight impact tests. (drop weight: 5.1 kg hemi-spherical head)

Test	Lay-up sequence	Impact velocity, V_0 (m/s)
1	$\left[0_2^\circ/90_2^\circ\right]_{3S}$	3.98
2	$\left[90_2^\circ/0_2^\circ\right]_{3S}$	3.98
3	$\left[90_2^\circ/0_2^\circ\right]_{3S}$	10.21
4	$\left[90_3^\circ/45_3^\circ/0_3^\circ/-45_3^\circ\right]_S$	10.72
5	$\left[0^\circ\right]_{24}$	10.83

Experimental results and discussion
Various factors (such as lay-up configuration, laminate thickness, constituent properties, temperature, impact velocity and energy, etc) can affect the impact response and damage patterns. For instance, for the 1st and 2nd drop-weight tests (cross-ply beams of different stacking sequences), the tup was first placed at the highest point of the impact tester, then dropped by free-fall. The velocity obtained was around 3.98 m/s. Figure 4-3.4 depicts the time histories of impact force and dynamic strain for Drop Test 1. As shown in the figure, peak impact force: 5.5 KN and maximum dynamic strain: 2,100 $\mu\varepsilon$ occurred around 1.0 and 1.4 ms, respectively.

The post-impact specimens were inspected by a Physical Acoustics Corporation UltraPAC immersion ultrasonic imaging system (Fig. 4-3.5) to reveal internal damage, if any, using C-scan. By observing the ultrasonic C-scans and optical microfractographs, as shown in Figs 4-3.6 and 4-3.7, respectively, the 3.98 m/s drop-weight impact velocity did not create any delamination in the $\left[0_2^\circ/90_2^\circ\right]_{3S}$ specimen.

Figure 4.3-8 shows the recorded time histories of impact force and dynamic strains for Drop Test 2. The peak impact force and maximum dynamic strain were 5.0 KN and 1,000 $\mu\varepsilon$, and occurred around 1.5 and 1.7 ms, respectively. Figure 4.3-9 displays the corresponding post-impact optical microfractographs, which clearly shows slight delamination. As indicated by these figures, for two otherwise identical cross-ply beams, e.g., $\left[0_2^\circ/90_2^\circ\right]_{3S}$ *vs* $\left[90_2^\circ/0_2^\circ\right]_{3S}$, different stacking sequences provide small difference in impact resistance.
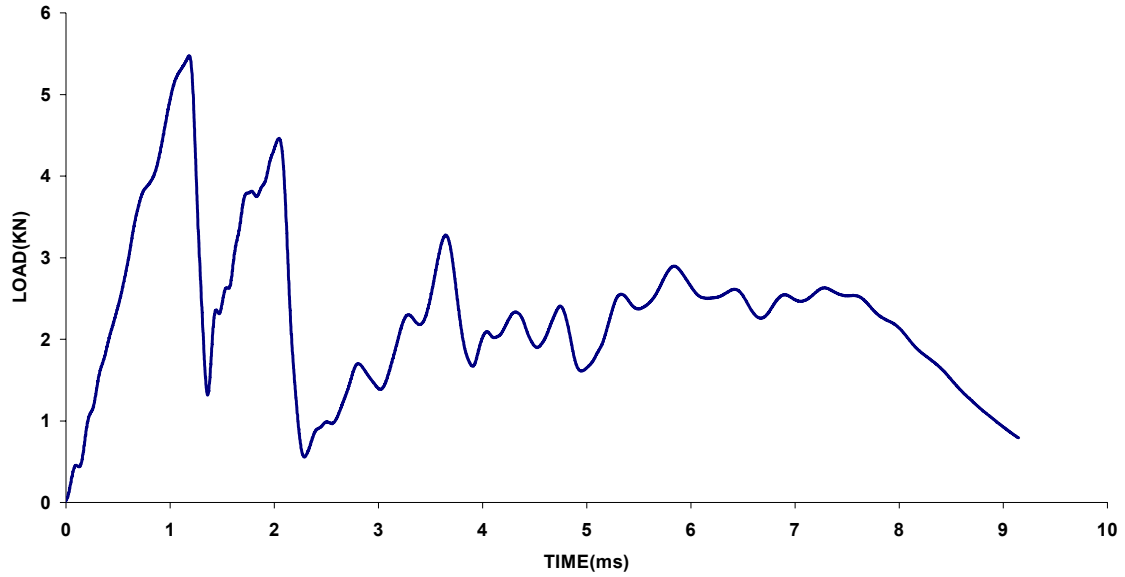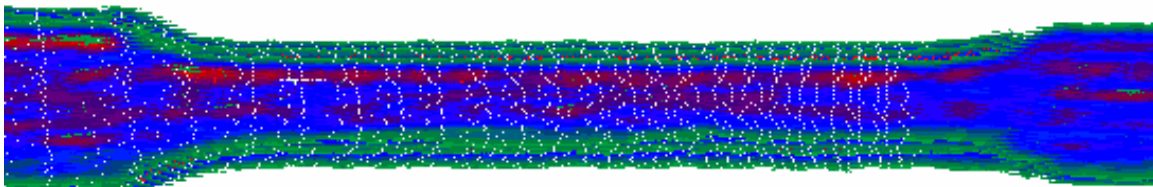
(a) impact force
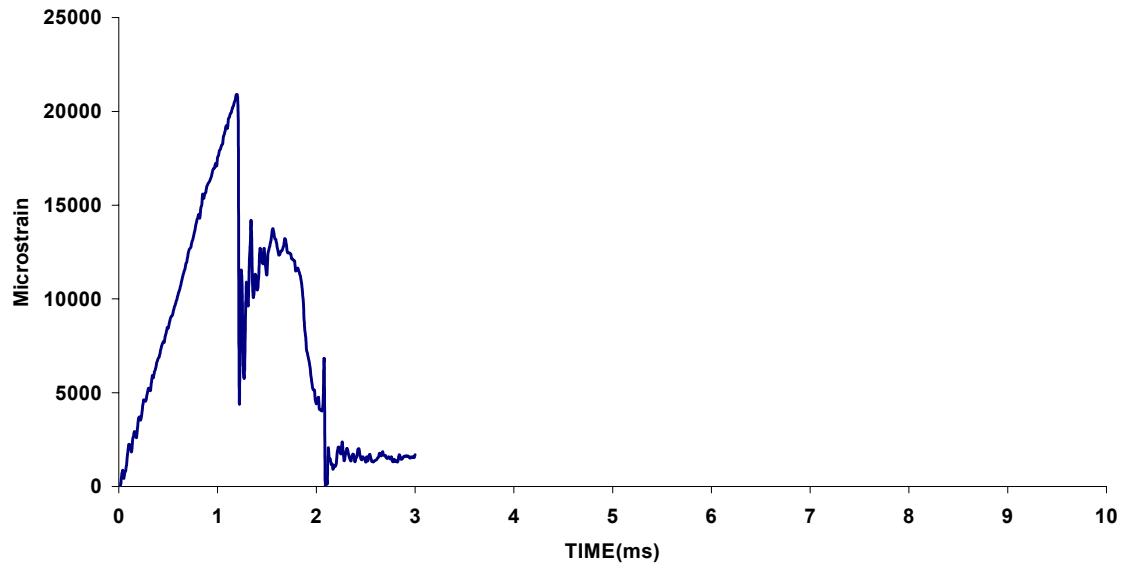
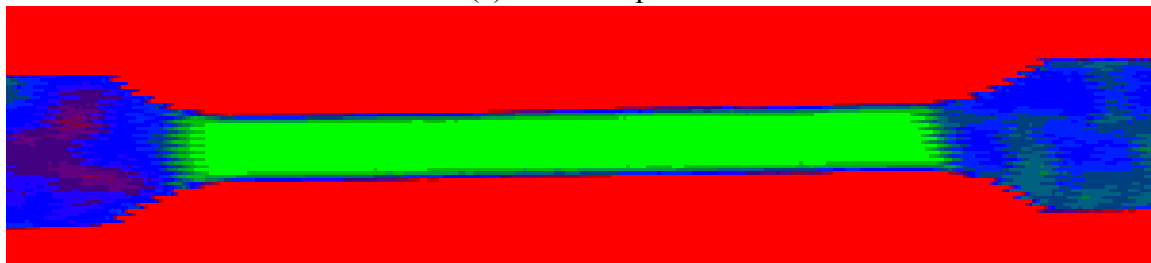
(b) dynamic strain (top gage: SG-1)

Figure 4.3-4.   Impact force and strain histories of Drop Test 1: $\left[0_2^\circ/90_2^\circ\right]_{3S}$ cross- ply S2 glass-toughened epoxy composite beam impacted at 3.98 m/s by a 5.1 kg hemi-spherical drop-weight.

Figure 4-3.5.   An immersion ultrasound system.

(a) before impact

(b) after impact

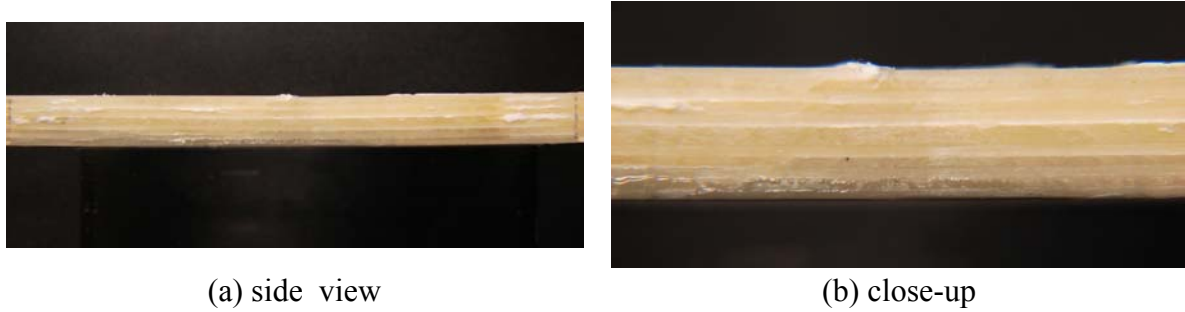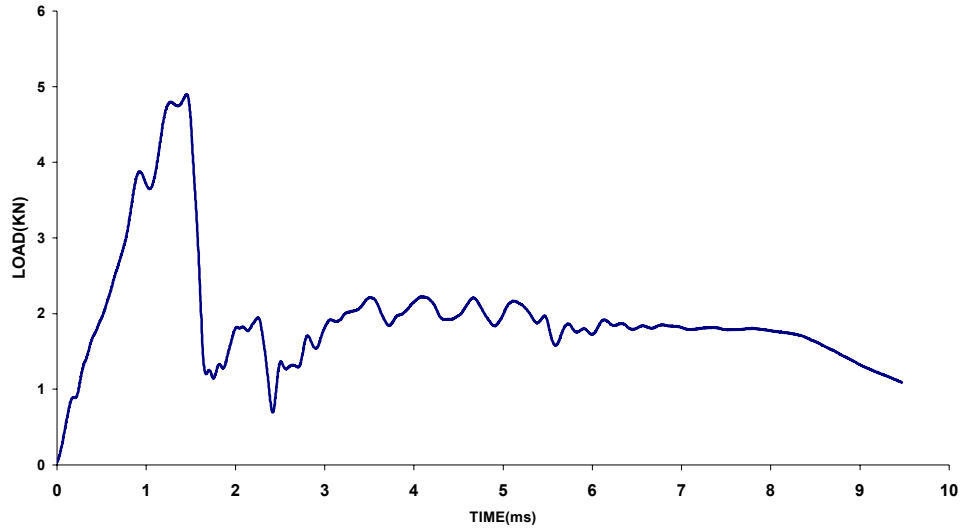Figure 4.3-6.   Ultrasonic C-scans of the cross-ply specimen before and after impact in Drop Test 1.

| (a) side view | (b) close-up |

Figure 4.3-7.   Post-mortem optical microfractographs of the cross-ply specimen used in Drop Test 1.

The results implies that the $\left[0_2^\circ/90_2^\circ\right]_{3S}$ stacking sequence is stronger than the $\left[90_2^\circ/0_2^\circ\right]_{3S}$ sequence. This can be explained easily by the fact that a lamina is much stronger along the 0° (longitudinal) direction than along the 90° (transverse) direction. During the dynamic flexural motion caused by drop-weight impact, since the maximum tensile and compressive axial strains occur at the top and bottom faces, hence placing the 0° orientation of the outer laminae along the spanwise direction of the composite beam should provide better impact resistance.

In order to reach higher drop-weight impact velocities, the pneumatic assistance option of the impact tester was activated for the remaining three Drop Tests; thus, as listed in Table 4.3-1, the impact velocities for Drop Tests 3 to 5 are 10.21, 10.72 and 10.83 m/s, respectively. These drop-weight tests with higher impact velocities caused more delamination and further damage. Figures 4.3-10 to 4.3-15 show their corresponding time-histories of impact forces and dynamic strains as well as optical microfractographs.

As depicted in Figs 4.3-12 and 4.3-13, the quasi-isotropic $\left[90_3^\circ/45_3^\circ/0_3^\circ/-45_3^\circ\right]_S$ specimen was the weakest and could only resist an impact force of 3.6 KN. During the drop-weight impact test, the specimen was broken completely at the impact site. By observing Figs 4.3-14 and 4.3-15, the uni-directional $\left[0^\circ\right]_{24}$ specimen could sustain a higher load of 3.9 KN; but also failed completely at the impact site. On the other hand, when impacted at 10.21 m/s, the $\left[90_2^\circ/0_2^\circ\right]_{3S}$ cross-ply specimen, even though suffered delamination in several layers; did not sever fully, as shown in Fig. 4.3-11. The cross-ply specimen sustained an impact force up to 5.8 KN, as indicated in Fig. 4.3-10. Thus, one may conclude that the cross-ply configurations: either $\left[0_2^\circ/90_2^\circ\right]_{3S}$ or $\left[90_2^\circ/0_2^\circ\right]_{3S}$ were stronger than other configurations when all other impact parameters being the same.

(a) impact force
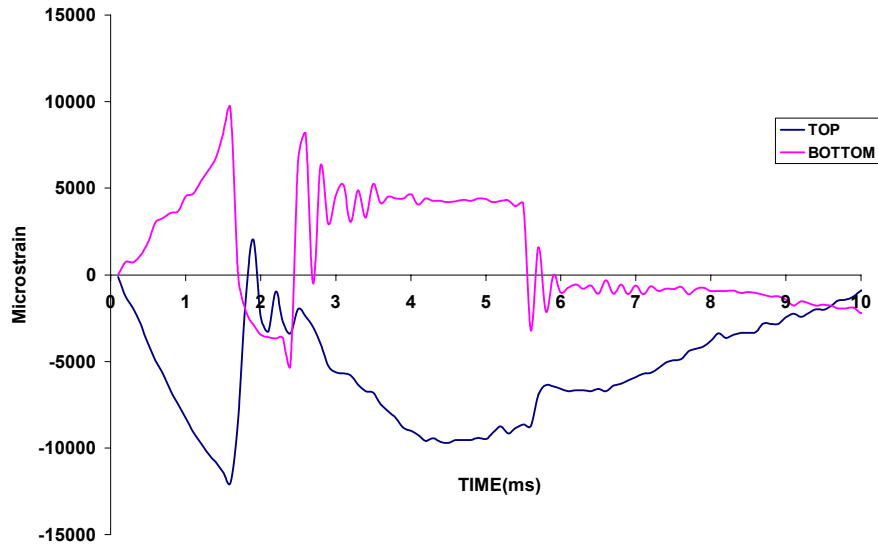
(b) dynamic strains

Figure 4.3-8.   Impact force and strain histories of Drop Test 2: $\left[90_2^\circ / 0_2^\circ\right]_{3S}$ cross- ply S2 glass-toughened epoxy composite beam impacted at 3.98 m/s by a 5.1 kg hemi-spherical drop-weight.
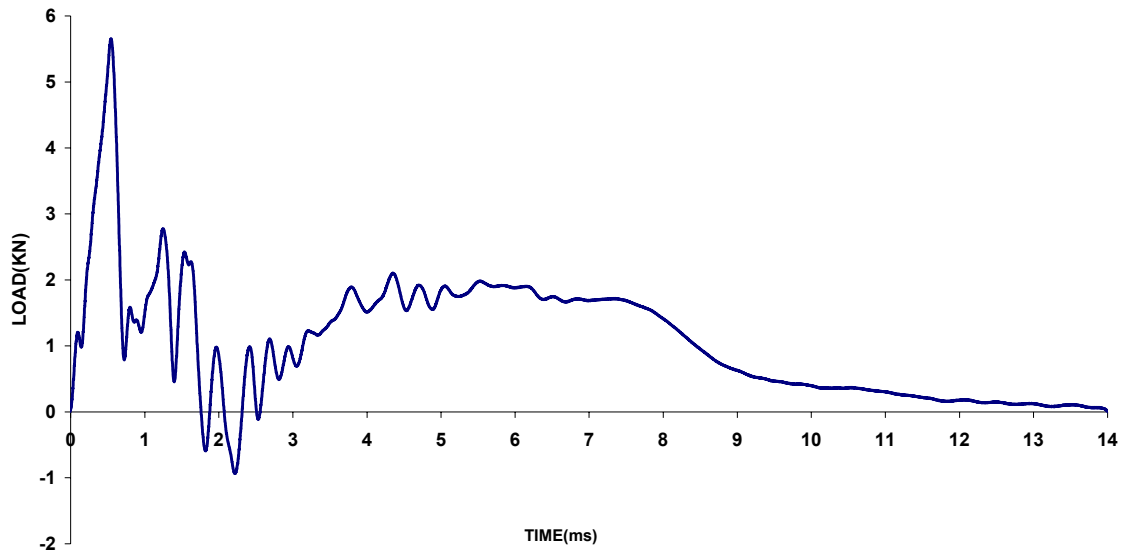

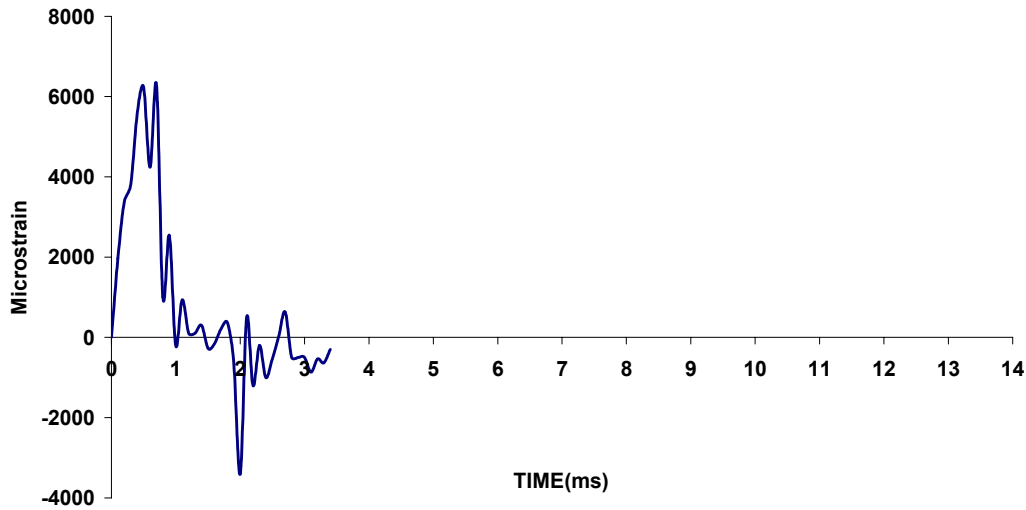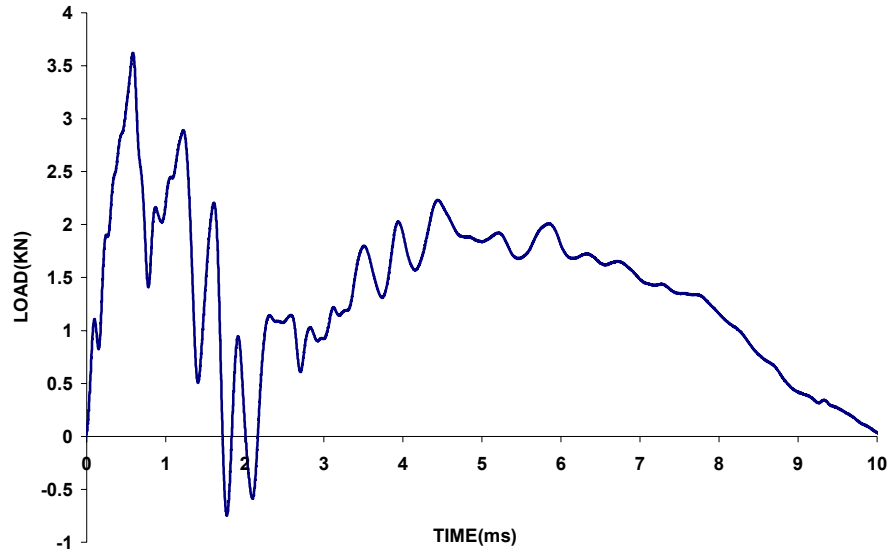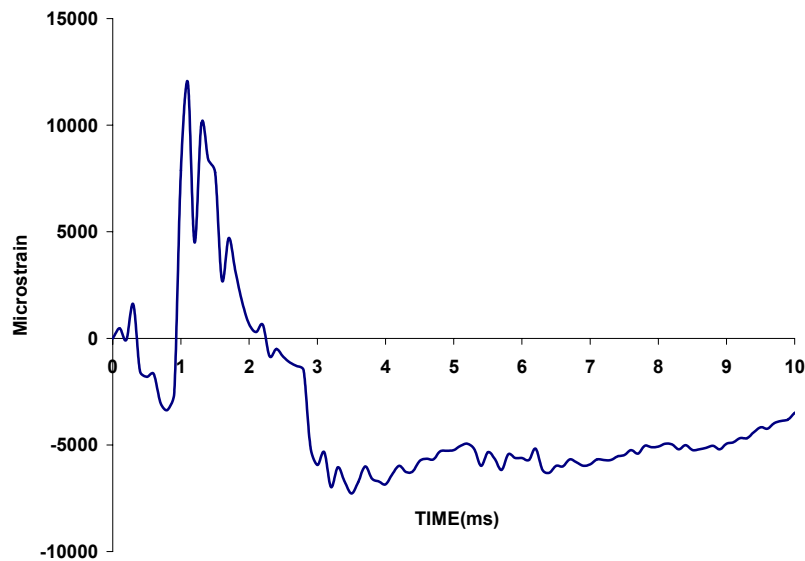(a) side view   (b) close-up

Figure 4.3-9.   Post-mortem optical microfractographs of the cross-ply specimen used in Drop Test 2.

(a) impact force

(b) dynamic strain (top gage: SG-1)

Figure 4.3-10. Impact force and strain histories of Drop Test 3: $\left[90_2^\circ / 0_2^\circ\right]_{3S}$ cross- ply S2 glass-toughened epoxy composite beam impacted at 10.21 m/s by a 5.1 kg hemi-spherical drop-weight.
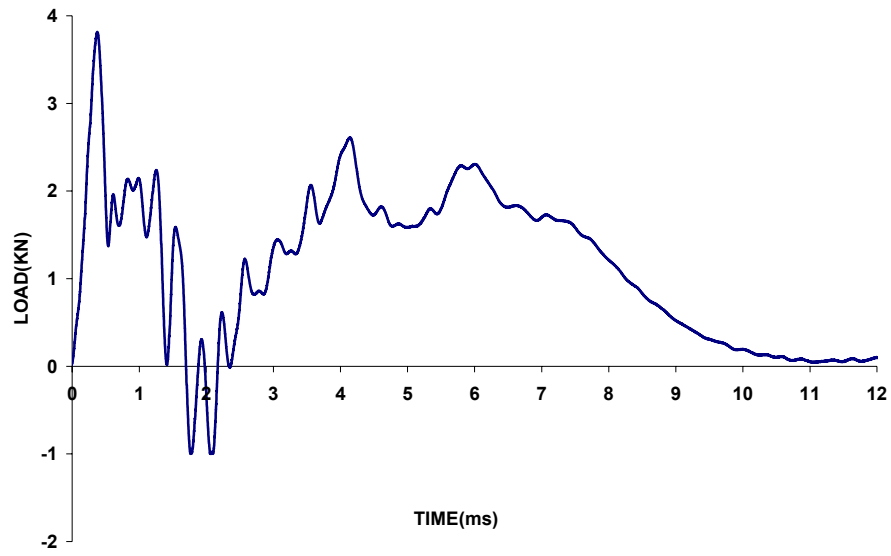

(a) side view   (b) close-up

Figure 4.3-11.   Post-mortem optical microfractographs of the cross-ply specimen used in Drop Test 3.

(a) impact force

(b) dynamic strain (top gage: SG-1)

Figure 4.3-12. Impact force and strain histories of Drop Test 4: quasi-isotropic $\left[90_3^\circ / 45_3^\circ / 0_3^\circ / -45_3^\circ\right]_S$ S2 glass-toughened epoxy composite beam impacted at 10.72 m/s by a 5.1 kg hemi-spherical drop-weight.
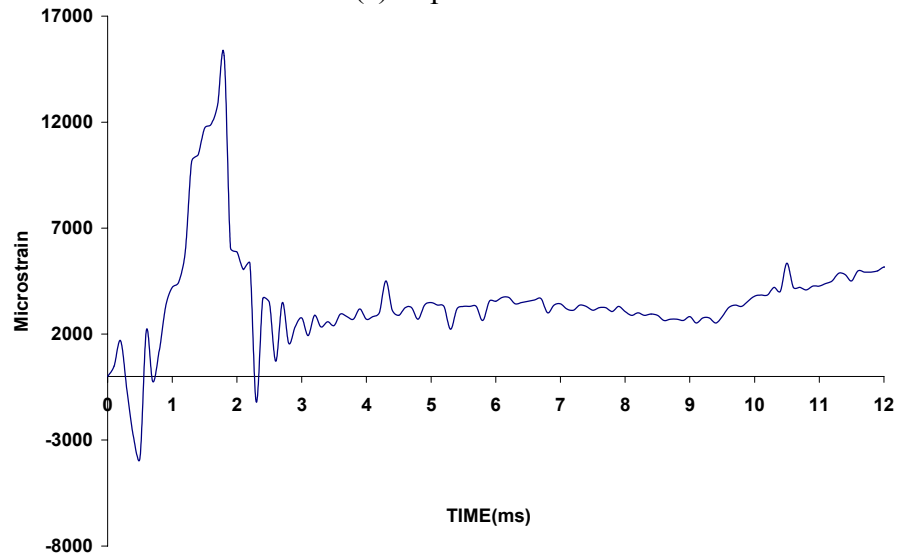

(a) side view

(b) close-up

Figure 4.3-13. Post-mortem optical microfractographs of the quasi-isotropic specimen used in Drop Test 4.

(a) impact force

(b) dynamic strain (top gage: SG-1)

Figure 4.3-14. Impact force and strain histories of Drop Test 5: $\left[0°\right]_{24}$ uni-directional S2 glass-toughened epoxy composite beam impacted at 10.83 m/s by a 5.1 kg hemi-spherical drop-weight.

(a) side view　　　　　　　　　　　　　　(b) close-up

Figure 4.3-15.　Post-mortem optical microfractographs of the uni-directional specimen used in Drop Test 5.

Dynamic finite element simulations

The afore-mentioned experimental results were used to validate a damage-induced nonlinear anisotropic constitutive law developed previously by this research group [176,177]. Figure 4.3-16 shows the stress-strain curves characterizing the damage-induced nonlinear anisotropic behaviors of the S2 glass/toughened epoxy. The slopes of these curves represent E_1: lamina Young's modulus along the fiber (longitudinal) direction, $E_2 = E_3$: lamina Young's moduli along the transverse directions, and $G_{12} = G_{13}$: lamina in-plane shear moduli, respectively. The initial slopes of these curves are: 40, 13 and 10 GPa, respectively. In addition, the density ρ of the composite is: 2 g/cm^3. These curves were then entered as User-Defined Material into LS-DYNA, which is a commercially available general-purpose finite element code for analysis of 3-D large deformation dynamic response of structures based on explicit-time integration scheme [178].

(a) E_1 (b) $E_2 = E_3$ (b) $G_{12} = G_{13}$
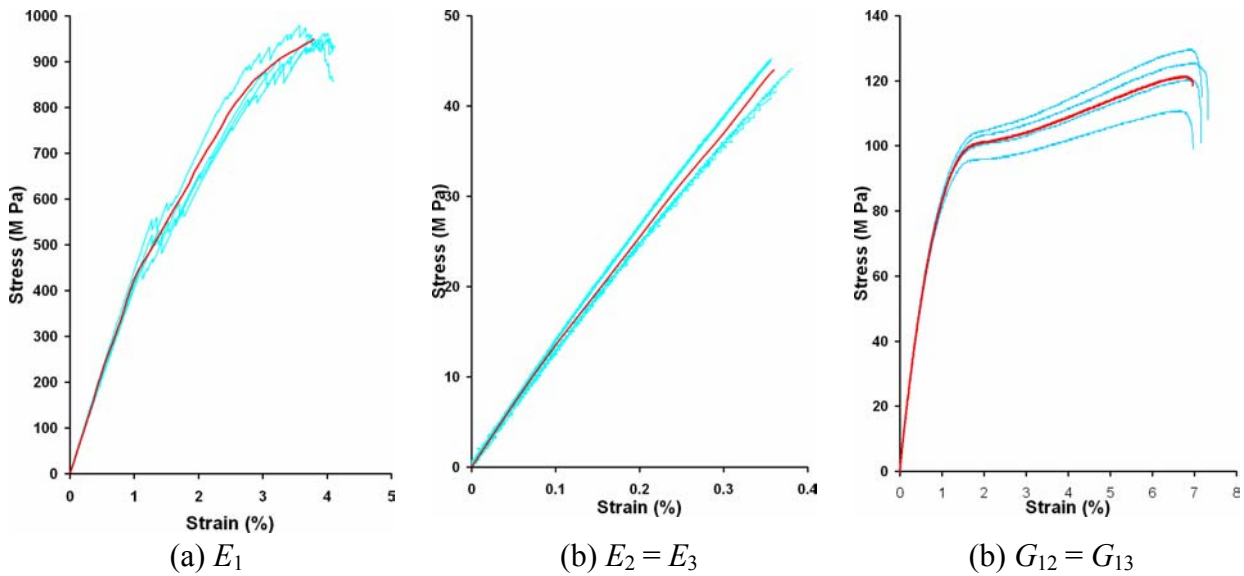
Figure 4.3-16. Nonlinear longitudinal, transverse and in-plane shear stress-strain curves with their slopes representing Young's and shear moduli.

Figure 4.3-17 shows the LS-DYNA finite element mesh simulating drop-weight impact onto a $\left[90_2^{\circ} / 0_2^{\circ} \right]_{3S}$ cross-ply composite beam. Low velocity drop-weight impact problems were modeled using orthotropic elastic material model (MAT 002) of LS-DYNA, which is valid for describing the elastic-orthotropic behaviors of solids, shells and thick shells without consideration for failure [178]. The Charpy-type straight-line impactor was modeled as a rigid body in the FEM simulations for drop-weight impact tests.
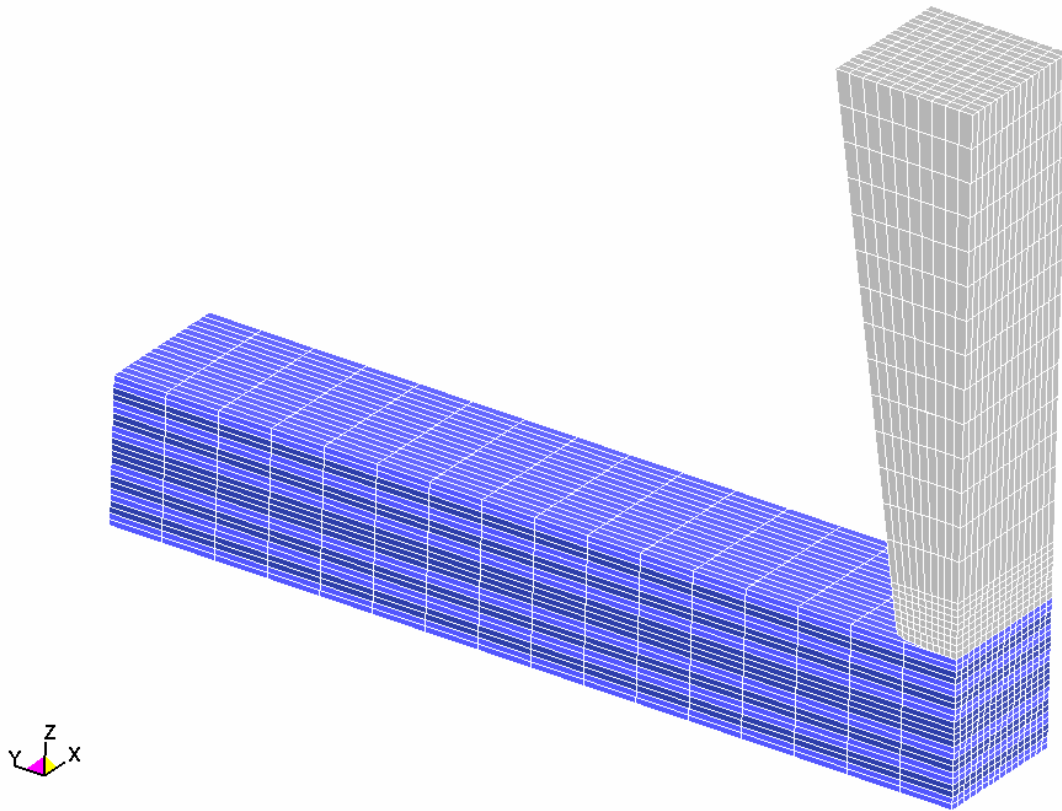
Figure 4.3-17.   Finite element simulation of drop-weight impact for the $\left[90_2^\circ / 0_2^\circ \right]_{3S}$ configuration.

In this study FEM predictions with experimental results were compared mainly for impact force and dynamic strain histories and post-impact damage patterns. The FEM mesh in Fig. 4.3-17 was used to simulate Drop Test 2: cross-ply $\left[90_2^\circ / 0_2^\circ \right]_{3S}$ composite beam impacted at 3.98 m/s by a 5.1 kg hemi-spherical drop-weight tup. Due to symmetry, only a quarter model was used with 256 elements for each layer for the 24-layer specimen. As shown in Fig. 4.3-18, the time histories of impact forces and dynamic strains between the experimental records and FEM results are in good agreement. The experimental curves of impact force and strain were smoother than the FEM results and exhibited time delays. This can be explained with the fact that experimental impact force and strain measurements were obtained through a load cell and strain gage amplifiers, where actual readings might have been filtered.
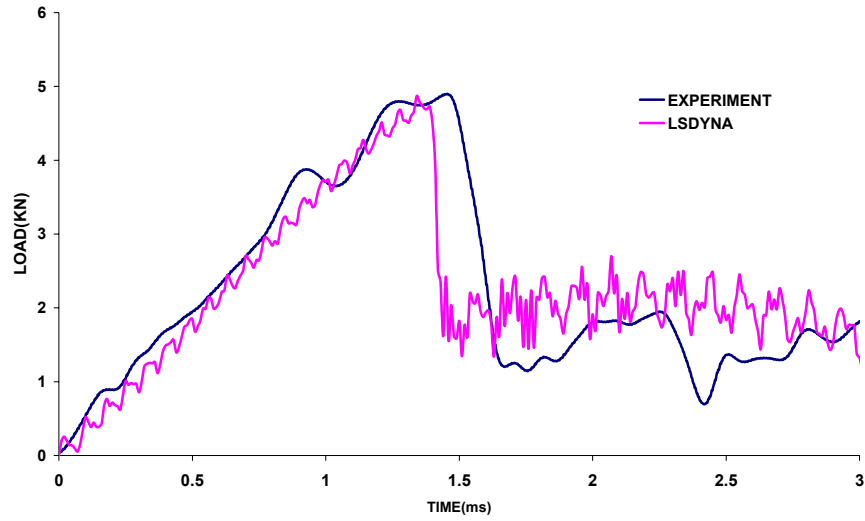
(a) impact force
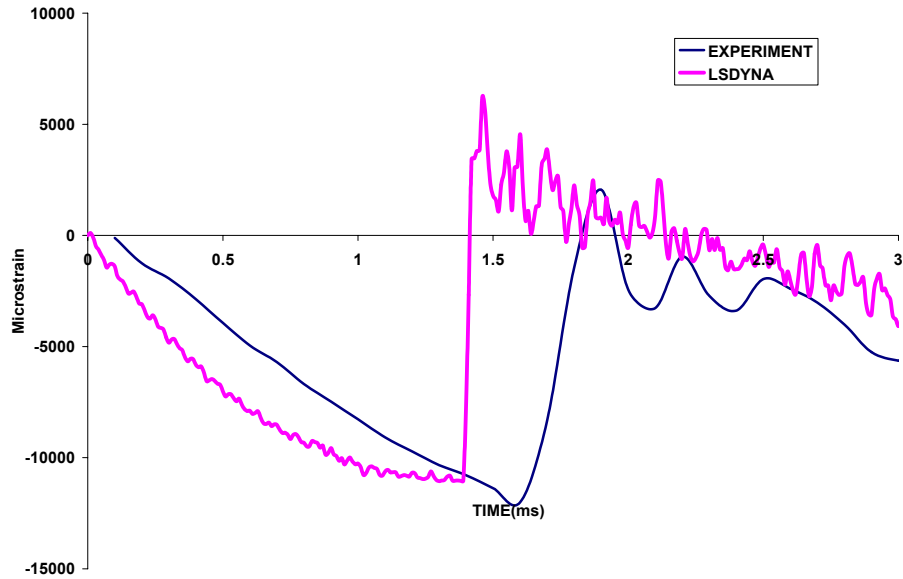
(b) dynamic strain

Figure 4.3-18. Comparison of impact force and dynamic strain histories for $\left[90_2^\circ / 0_2^\circ\right]_{3S}$ cross-ply S2 glass-toughened epoxy composite beam impacted at 3.98 m/s by a 5.1 kg hemi-spherical drop-weight.

4.4: Drop-weight impact tests of woven hybrid composites

Experimental procedures

Low impact tests at three different energy levels were carried out using the Dynatup impact machine. During all impact tests, a 5.1 kg weight was attached to a steel impactor with a hemispherical tip diameter of 16 mm. The first energy level 40J was obtained by placing the mass at the highest position and dropping it freely. To obtain 50J and 100J, the mass was placed at the highest position and the pneumatic assistance option was deployed to increase the impact energy. Specimens were clamped circumferentially along a diameter of 76.2 mm in the pneumatic clamped fixture. Figure 4.4-1 shows the schematic drawing of low impact test. "h" is the height to obtain maximum potential energy. "d" is the maximum deflection that occurs during the test. Details of the drop-impact tests conducted during this study are given in Table 4.4-1.
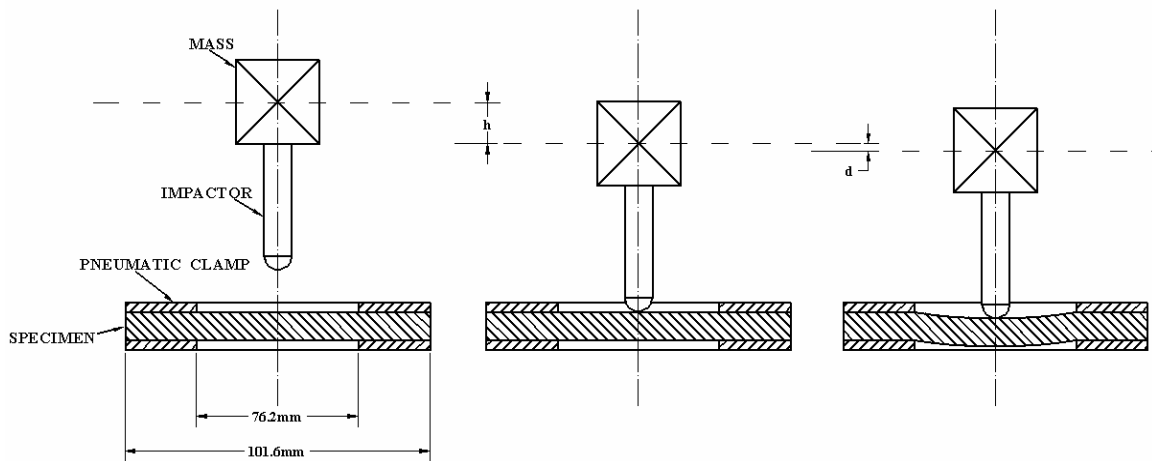
Figure 4.4-1 Schematic drawing of the experimental set-up for low impact tests of woven hybrid composites.

Table 4.4-1 Information of low impact tests of woven hybrid composites.

	SPECIMEN TYPE	VELOCITY(m/s)	MASS(kg)	IMPACT ENERGY(J)	ABSORBED ENERGY(J)	REBOUND ENERGY(J)
1	GL	3.82	5.1	40	15.84	24.16
2	GR/GL/GL/GR	3.91	5.1	40	16.71	23.29
3	GR	3.88	5.1	40	26.25	13.75
4	GL/GR/GR/GL	3.91	5.1	40	16.04	23.96
5	GL/GR/GR/GL	4.39	5.1	50	23.18	26.82
6	GR/GL/GL/GR	4.38	5.1	50	18.4	31.6
7	GR	4.4	5.1	50	35.86	14.14
8	GL	4.41	5.1	50	12.32	37.68
9	GR/GL/GL/GR	6.27	5.1	100	78	22
10	GL/GR/GR/GL	6.29	5.1	100	78.64	21.36
11	GR	6.26	5.1	100	100	0
12	GL	6.29	5.1	100	72	28

Impacted specimens were scanned using an ultrasonic system. The through transmission technique using 5 MHz focused transducer was successfully applied to see the internal delamination of the impacted specimens. Additionally, optical pictures of the front and back surface of the damaged composites were taken.

Experimental results and discussion

Figures 4.4-2 to 4.4-5 show the optical and C-scan images of impacted specimens. An important issue is how these images should be interpreted. Once optical images were evaluated, it was clear that the length of the horizontal and vertical cracks at the front surface of the GL and GR/GL/GL/GL specimens was longer compared to the other two types. Table 5.2 shows the length of the cracks of impacted specimens.

Table 4.4-2 Front surface crack length of composites impacted at 40J, 50J and 100J.

SPECIMEN TYPE	CRACK LENGTH (mm)							
	GL		GL/GR/GR/GL		GR/GL/GL/GR		GR	
IMPACT ENERGY	VERTICAL	HORIZONTAL	VERTICAL	HORIZONTAL	VERTICAL	HORIZONTAL	VERTICAL	HORIZONTAL
40J	40	33	28	23	54	61	39	35
50J	35	46	41	29	50	50	28	37
100J	81	48	21	34	76	64	39	42

The back surface damage for the GL specimen was not seen at 40J and 50J energy levels. The GR composites had back surface damage for all energy levels and perforation occurred at 100J test. When a glass outer layer was used, GL/GR/GR/GL composites had back surface damage more than glass composite but less than all others. The GR/GL/GL/GR composites, which had graphite as the outer skin, had less back surface damage than GR composites and more than all others. It can be said that glass fabrics can be used as an outer skin to decrease the surface damage of the graphite composites by paying the price of increased weight. Most of the composites delaminate after low impact. The delamination sometimes occurs inside the composite and can not be seen by naked eye. The degree of delamination should be examined carefully. The ultrasonic C-Scan is the most common technique to measure delamination in impacted composites. C-Scan images showed increase in delamination as a result of increased energy for all type of composites except for the 100J impact test of GR specimen. The 50J impact test created more delamination in GR specimen compared to 40J impact tests. However, 100J impact created less delamination than other energy levels. During 100 J impact test, perforation was observed. Thus, it can be said that the energy of the impactor was mostly used for perforation instead of delamination. Comparison of delaminated areas showed that GL and GR composites delaminated less than the hybrid types. The GL/GR/GR/GL composites delaminated more than all other types. The GR/GL/GL/GR composites also delaminated more than GL and GR composites but less than the GL/GR/GR/GL composites. There is a direct relation between the degree of delamination and the interfacial forces between the laminas. It can be said that the interface is stronger when the same type of laminae stacked together. However, stacking different fabrics or changing the direction of the laminae decreases interfacial strength. The increased delamination seen in the hybrid composites is because of weaker interfacial strength. Table 4.4-3 shows the delaminated areas of impacted specimens.

Table 4.4-1 Delaminated areas of impacted composites.

SPECIMEN TYPE	DELAMINATED AREA(mm^2)		
	40J	50J	100J
GL	116	161	310
GR	129	160	232
GL/GR/GR/GL	290	336	516
GR/GL/GL/GR	232	244	303

a) Front Surface

b) Back Surface
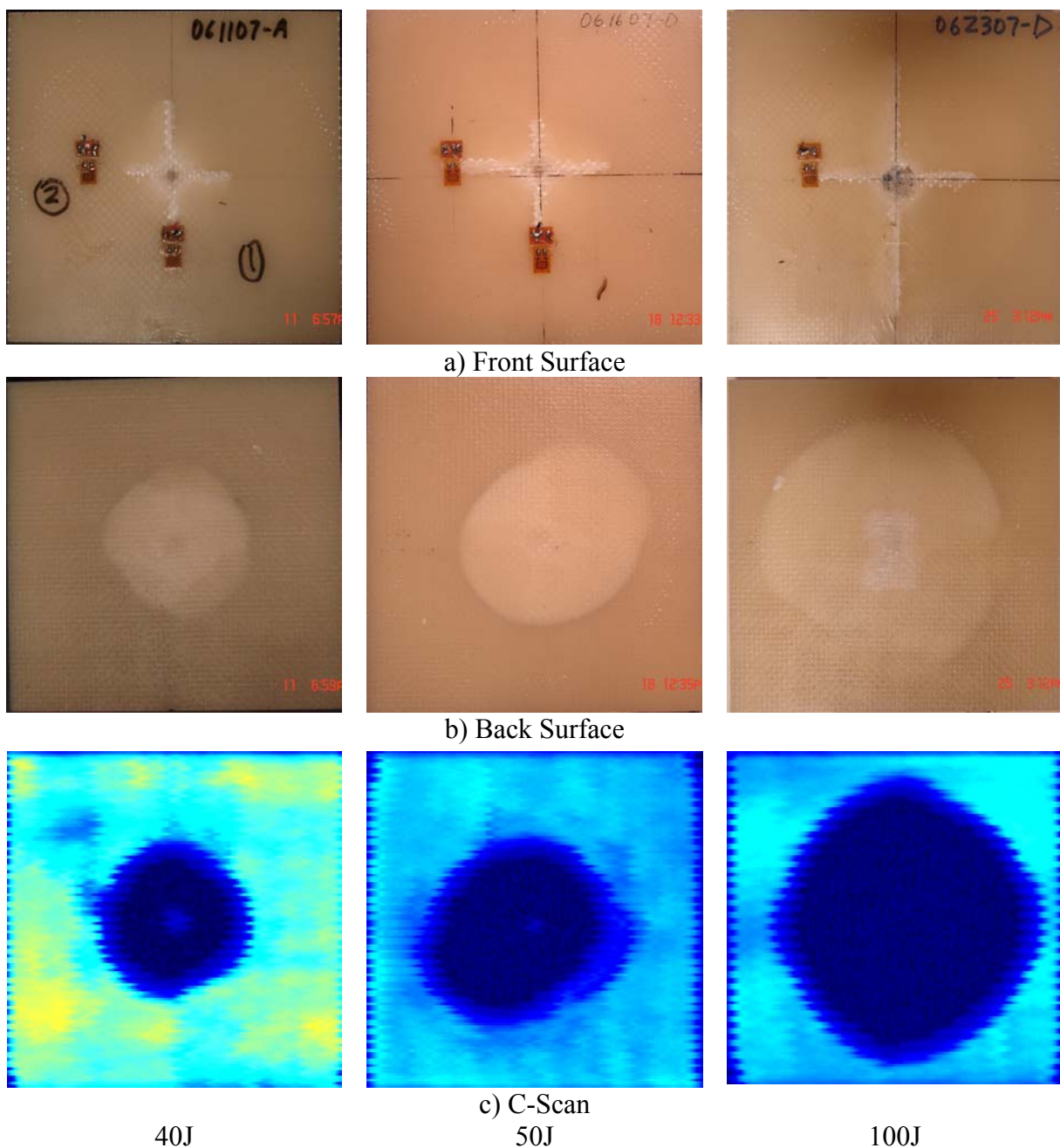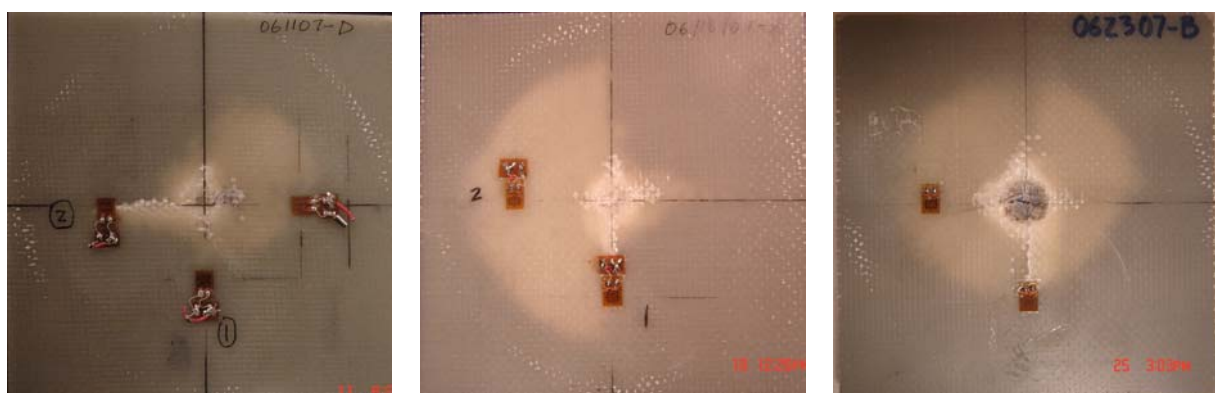

c) C-Scan

40J   50J   100J

Figure 4.4-2 Optical pictures and C-scans of GL composites impacted at 40J, 50J and 100J.

a) Front Surface

b) Back Surface
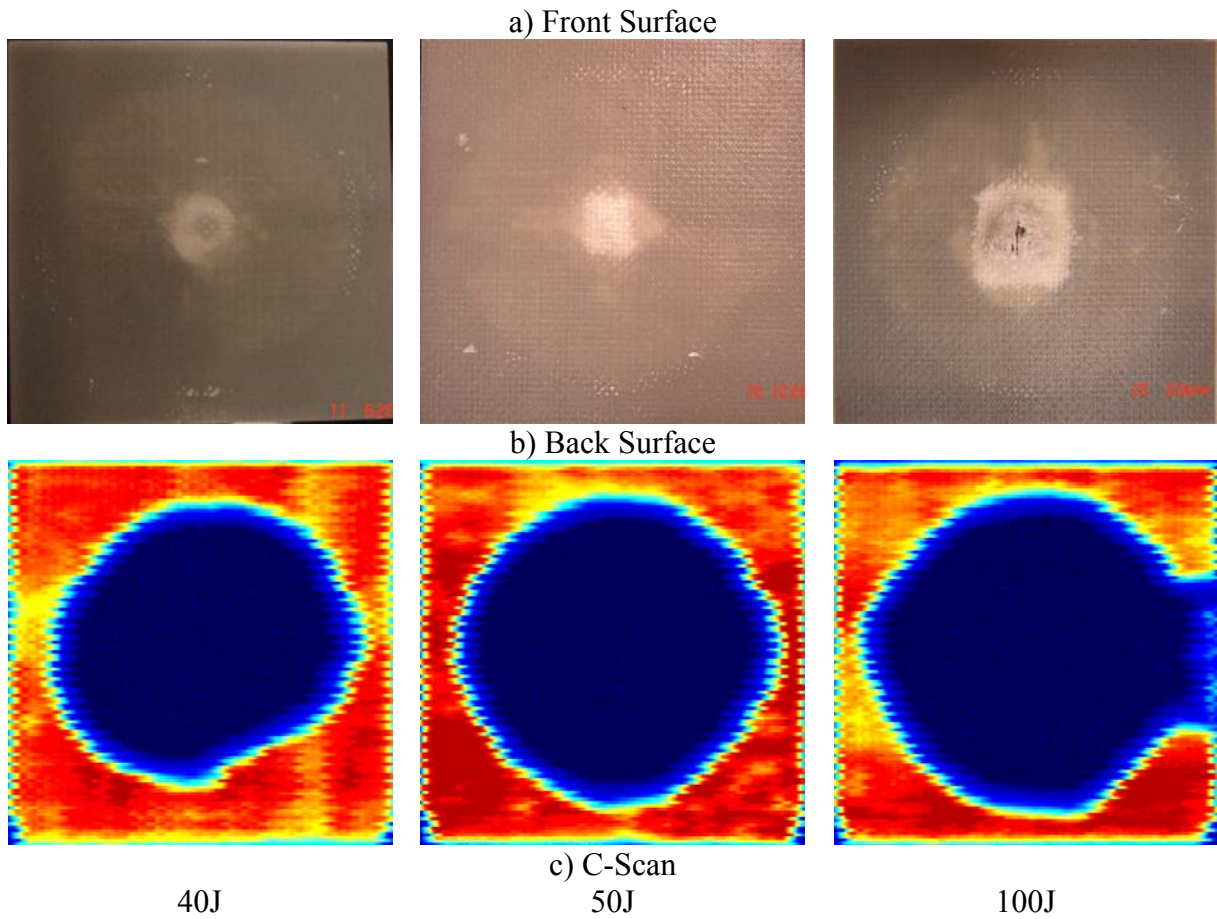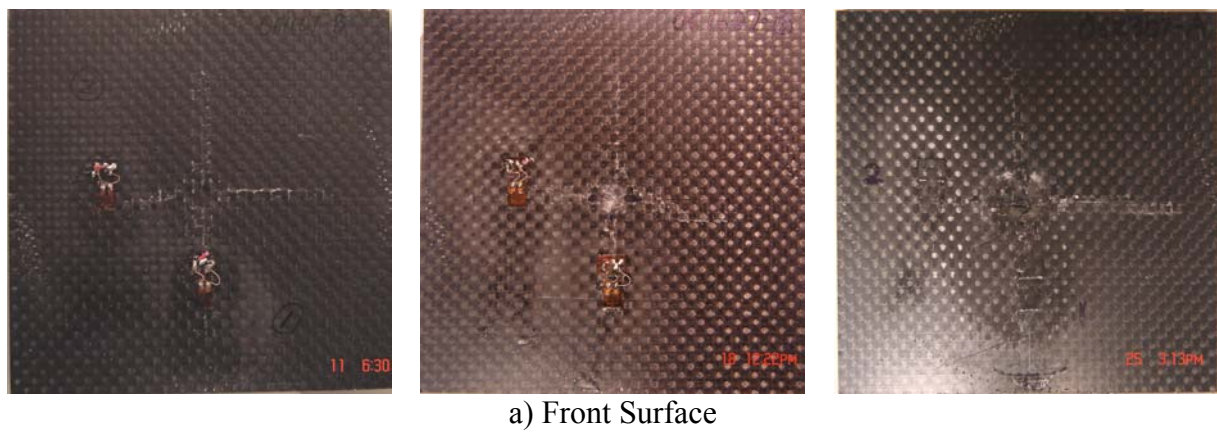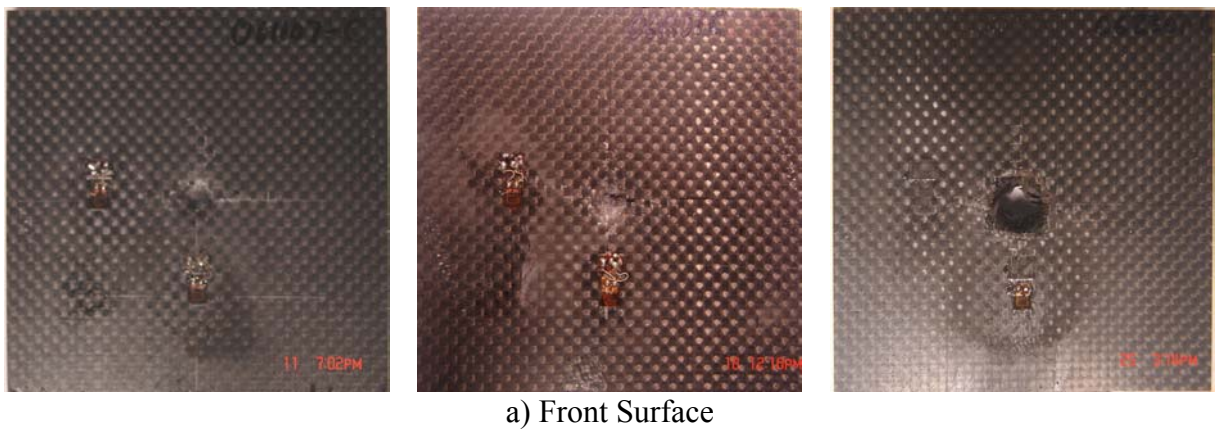

c) C-Scan

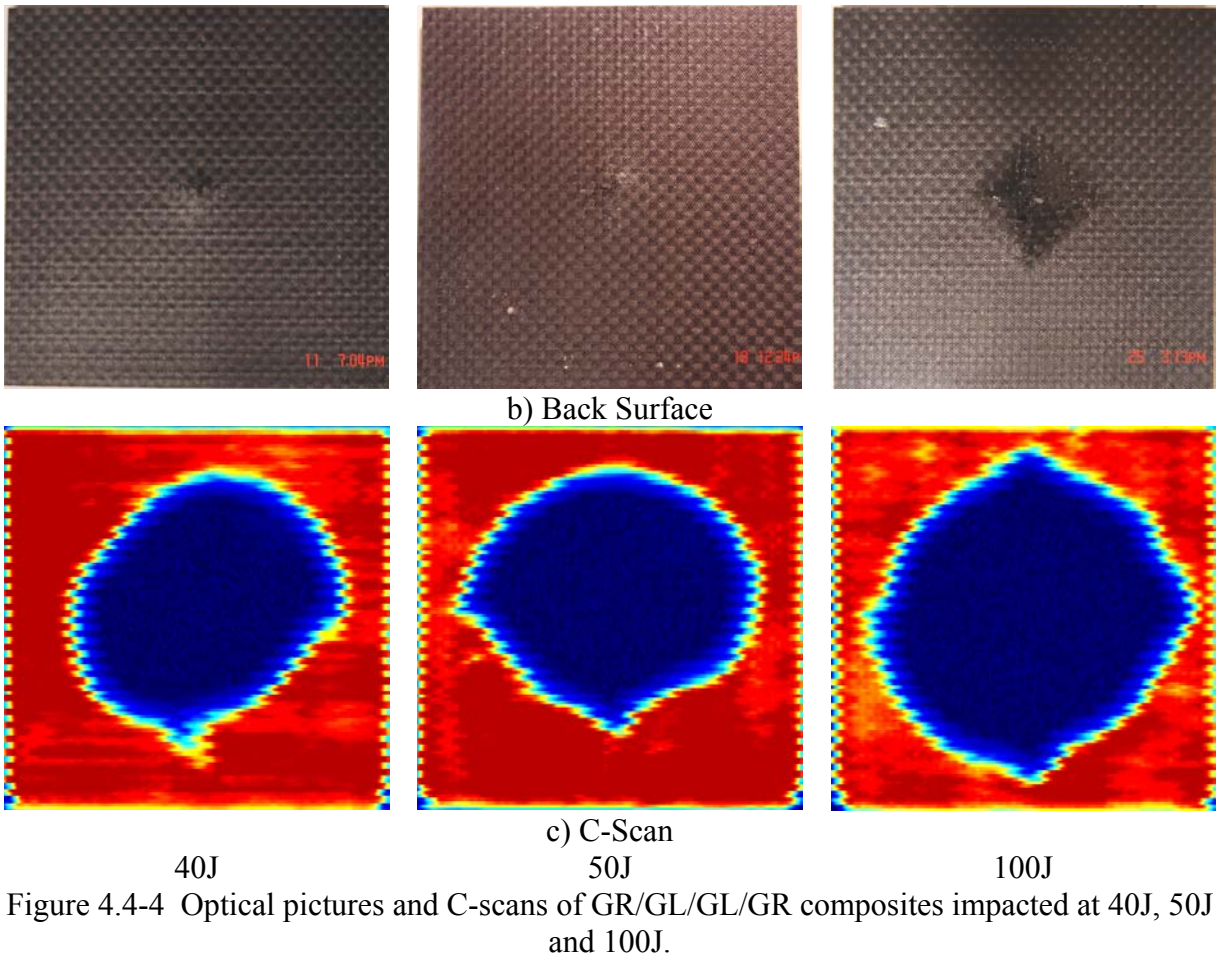| 40J | 50J | 100J |

Figure 4.4-3 Optical pictures and C-scans of GL/GR/GR/GL composites impacted at 40J, 50J and 100J.

a) Front Surface

b) Back Surface

c) C-Scan

40J   50J   100J

Figure 4.4-4 Optical pictures and C-scans of GR/GL/GL/GR composites impacted at 40J, 50J and 100J.

a) Front Surface

b) Back Surface
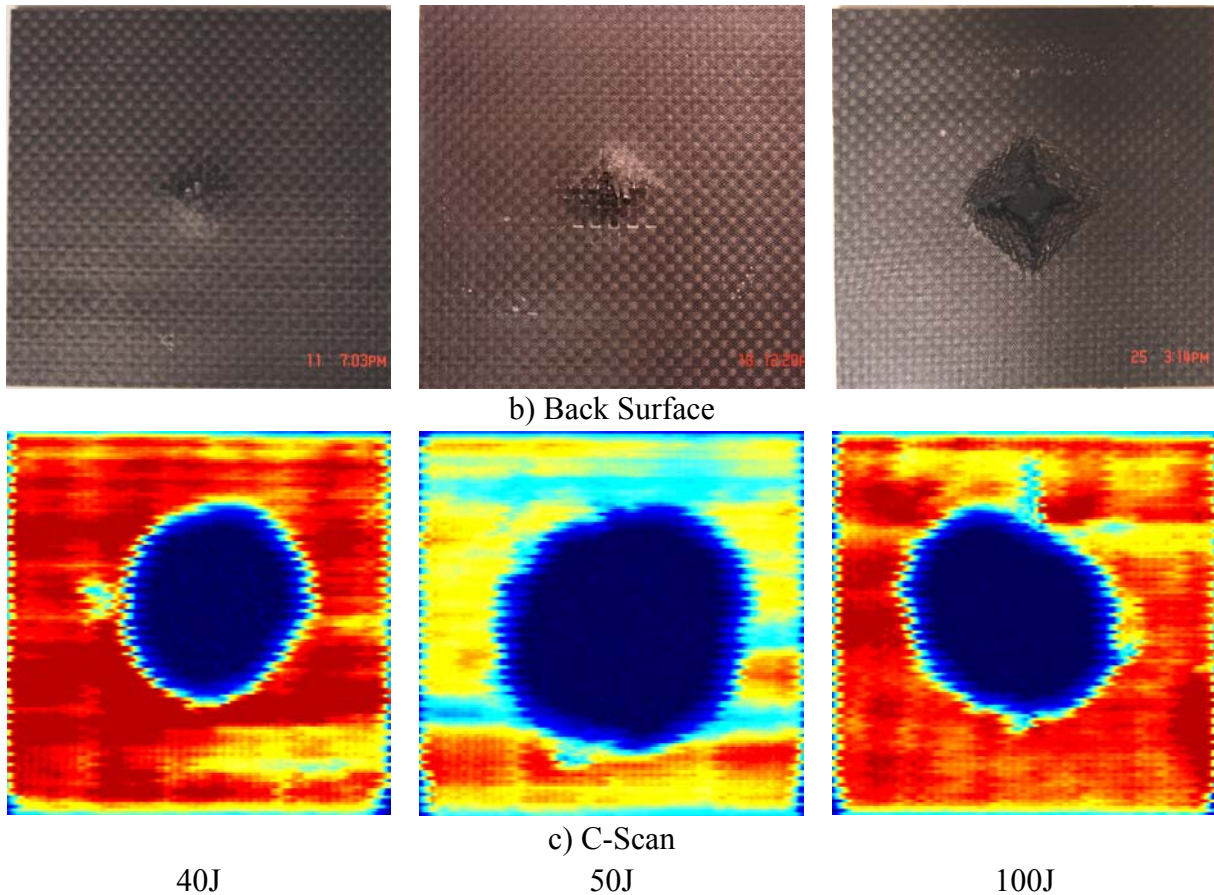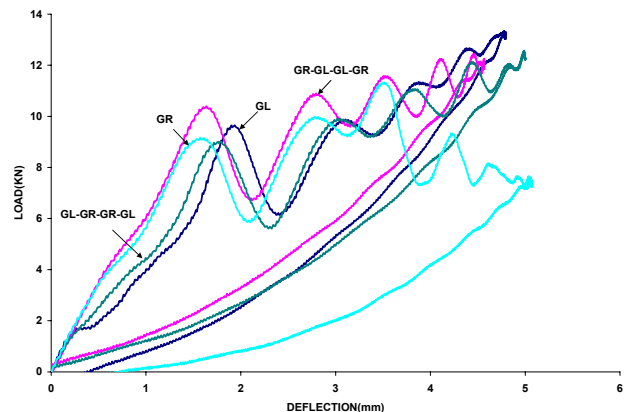

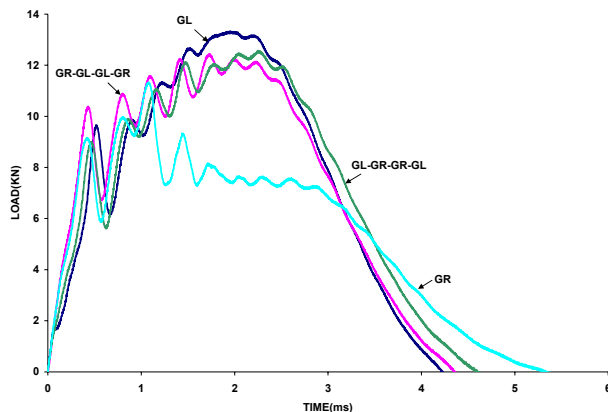c) C-Scan

| 40J | 50J | 100J |

Figure 4.4-5 Optical pictures and C-scans of GR composites impacted at 40J, 50J and 100J.

It should be noted that the Dynatup 930-I data acquisition system can only measure the initial velocity of the impactor and the load vs. time directly. Remaining parameters such as absorbed energy, velocity of impactor and deflection can be calculated using equations of motion. Figures 4.4-6 to 4.4-8 show the low impact response of composites subjected to impact at three different energy levels.

Figure 4.4-6.a shows the force time histories of the four types of specimens. Once the curves are evaluated, it is obvious that all of the curves are linear increase at the beginning until the 9-10KN load level. The oscillations started after that level and the load still increased. The GL specimen had a peak value of 13.3 KN, and the hybrid specimens behaved very similarly with a peak value of 12.4 KN. The load values for three cases became zero at around 4.3 ms. However, the GR specimen followed a completely different pattern and when the load was around 11.2 KN, sudden drop occurred and load did not change for 2 ms. The load started to decrease at $t = 3$ ms. The duration of the contact for GR was around 5.4 ms which was higher than the other cases. The visual images in Figure 4.4-2 to 4.4-5 clearly show that all the specimens had delamination and only the GR specimen had back surface damage during 40J impact. Thus, it can be said that the oscillations after linear increase represents delamination and the sudden drop of GR specimen represents the damage at the back surface. The area under the load deflection curve (Fig. 4.4-6.b) gives us the energy absorbed by the specimen during impact. At first look, it is obvious that the GR specimen absorbed more energy than the others. The remaining three specimens absorbed almost the same amount of energy during the 40 J impact.

The deflection-time histories (Fig. 4.4-6.c) clearly show the maximum deflection during the impact. The maximum deflection, which was 4.9 mm for GL, GL/GR/GR/GL and GR/GL/GL/GR specimens, occurred at 2.15 ms. The maximum deflection for GR specimen was 5.04 mm and happened at 2.7ms. The velocity-time (Fig. 4.4-6.d) histories also show when the velocity of the impactor became zero and how the velocity changed after impact. The energy time histories (Fig. 4.4-6.e) are commonly used to calculate the impact energy, absorbed energy and rebound energy. During the low impact event, when the impactor touches the specimen it has the full kinetic energy and starts discharging this energy into the specimen. Thus, energy in the specimen linearly increases at the beginning. Once impactor spends all of its energy, deflection of the specimen is at the highest point. This point corresponds to the impact energy and it was 40 J. At that point; the specimen is loaded with energy and tries to bounce back to initial position. Due to this high level of energy, some deformation and delamination occurs in the specimen and some of the energy is spent. The remaining energy is used for the rebound of the impactor. The energy absorbed by GL, GR/GL/GL/GR and GL/GR/GR/GL specimens was around 16 J. The GR specimen absorbed 26 J during the 40 J impact. These values can be seen by looking at the constant energy level after impact in energy-time histories (Fig. 4.4-6.e). Once the absorbed energy is subtracted from the contact energy, the rebound energy is determined.

The same evaluation procedure can be applied for the 50 J and 100j impacts. Instead of doing so, some important points will be highlighted for the remaining two sets of experiments. The response of the composite specimens to 50 J impact (Fig. 4.4-7) exhibited similar behavior as in the 40 J impact case. However, the duration of the impact, the peak load values and the absorbed energies increased as a result of increasing impact energy. The energy absorption (Fig. 4.4-7.e) by the specimens was different. While the GR specimen absorbed 35J, the GL specimen absorbed 12 J. The hybrid specimen's energy absorption was between GL and GR. The response of the composites to 100 J impact (Fig. 4.4-8) was quite different compared to other energy levels. A sudden drop after the peak load value was observed for all the specimen types (Fig. 4.4-8.a). This was due to the back surface damage which occurred for all types. The back surface images also (Figs 4.4-2 to 4.4-5) clearly show the damage. Another important point is the behavior of the GR specimen. All graphs for 100 J impact shows that GR behaved very differently than others. This was due to the perforation that happened in impacting the GR specimen at 100J energy level. The load- deflection curve (Fig. 4.4-8.b) did not have a close loop which was the case for all rebounded tests. Deflection continued (Fig. 4.4-8.c) to increase and velocity (Fig. 4.4-8.d) did not change sign. The energy-time curve (Fig. 4.4-8.e) shows that all of the impact energy was absorbed by the GR specimen.

a) Load-time histories

b) Load-deflection curves

c) Deflection-time histories

d)Velocity-time histories
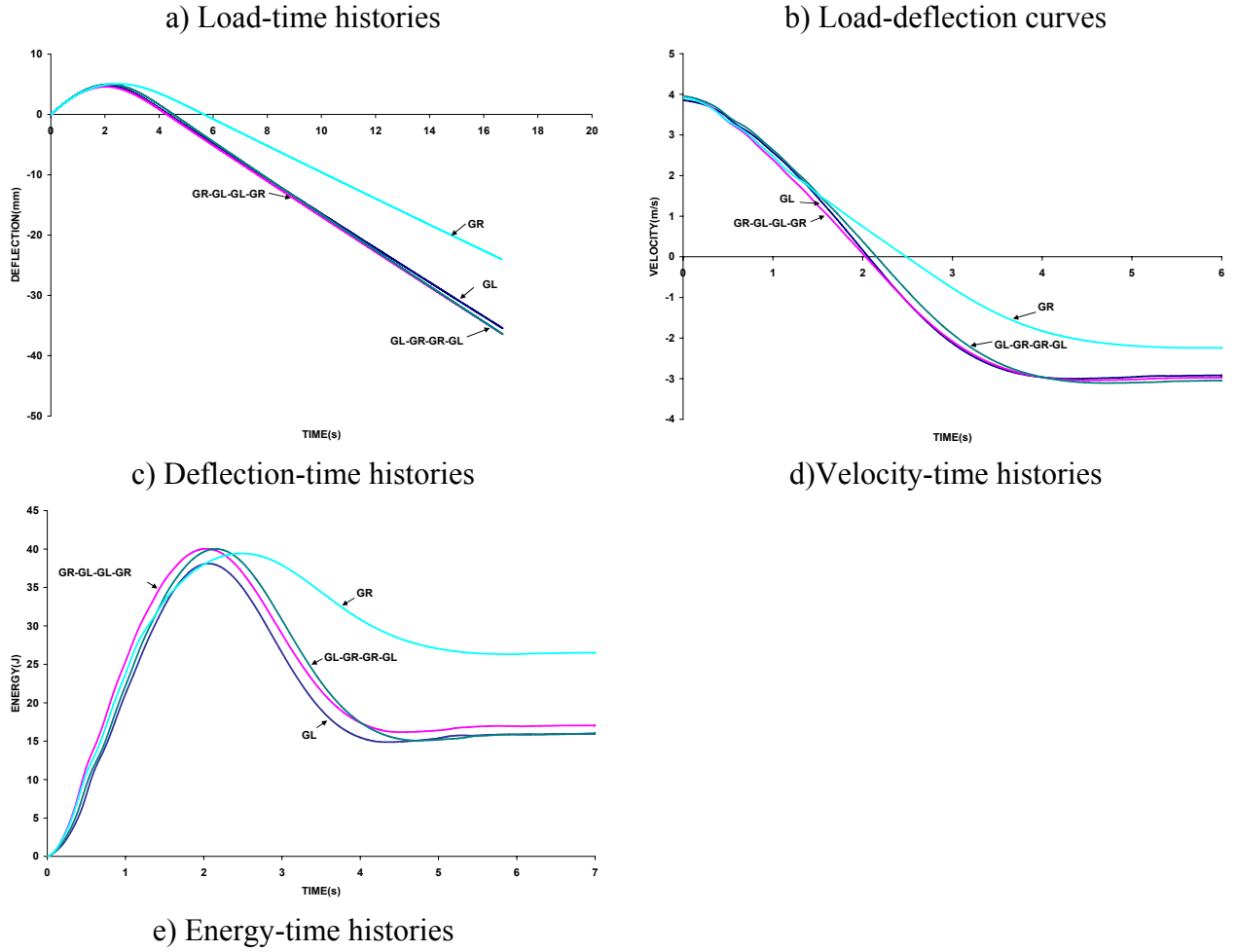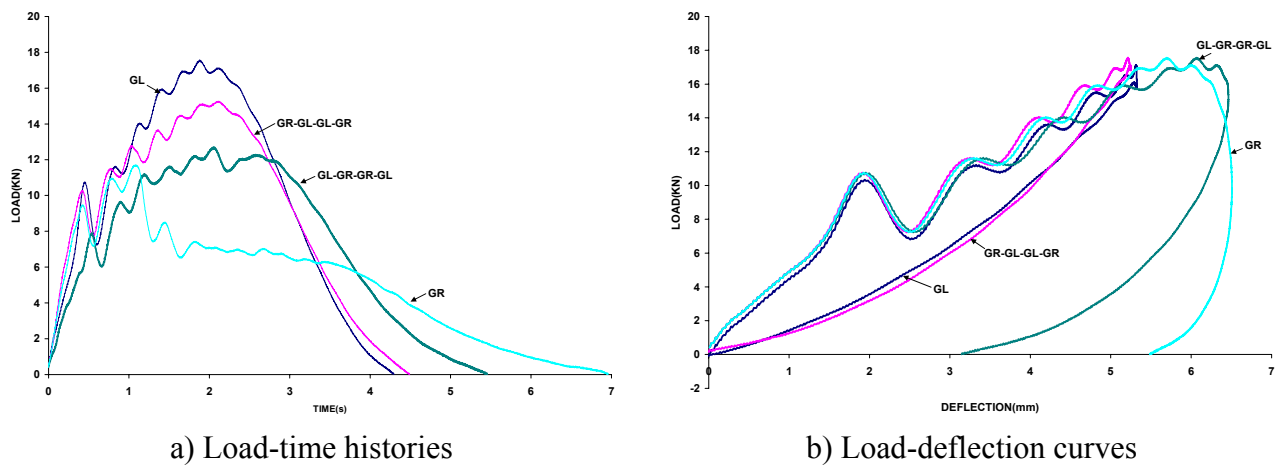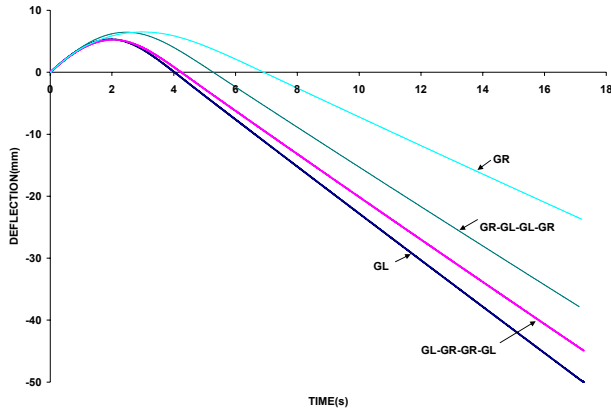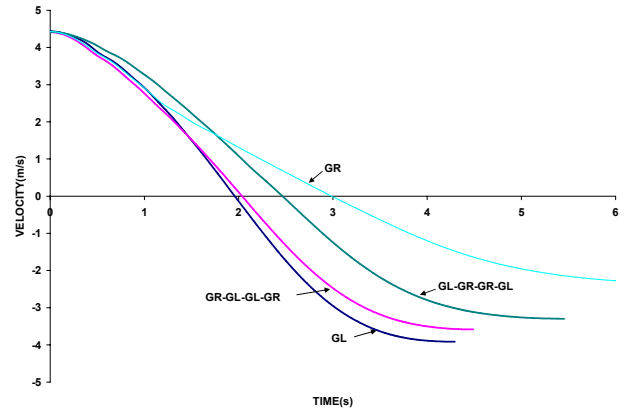
e) Energy-time histories

Figure 4.4-6 Low-impact response of GL, GR, GL/GR/GR/GL and GR/GL/GL/GR composites subjected to 40J impact.
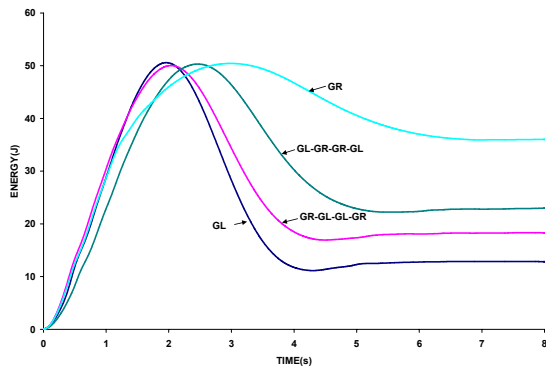
a) Load-time histories

b) Load-deflection curves

c) Deflection-time histories

d)Velocity-time histories

e) Energy-time histories

Figure 4.4-7 Low-impact response of GL, GR, GL/GR/GR/GL and GR/GL/GL/GR composites subjected to 50J impact.

a) Load-time histories

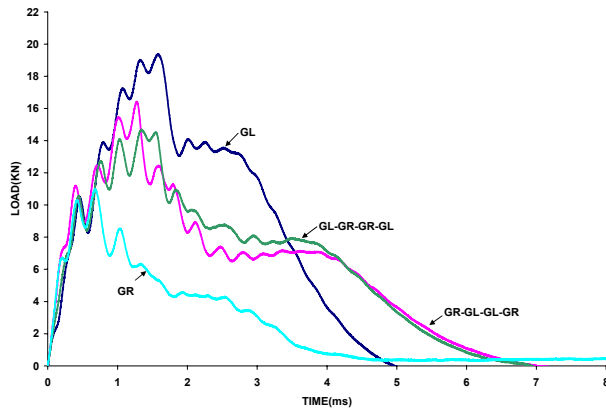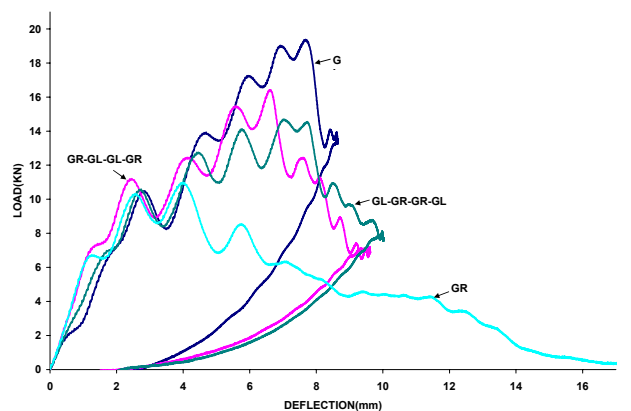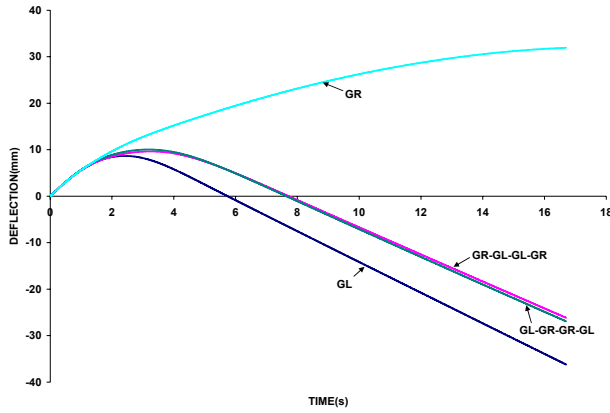b) Load-deflection curves

c) Deflection-time histories
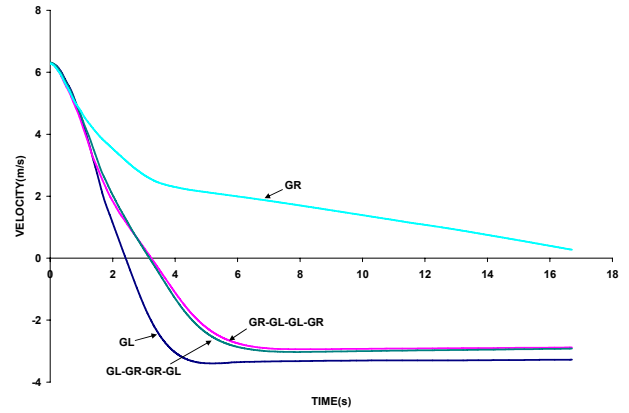
d)Velocity-time histories
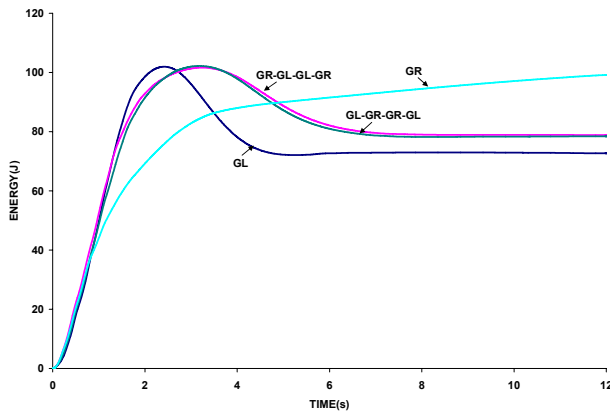
e) Energy-time histories

Figure 4.4-8 Low-impact response of GL, GR, GL/GR/GR/GL and GR/GL/GL/GR composites subjected to 100J impact.

Prior to impact tests, two strain-gages were mounted at the front surface of each specimen and the strain-time histories were recorded through a strain-gage amplifier and data-acquisition system. Figure 4.4-9 shows the locations of two strain-gages and dimensions of the impact specimens.
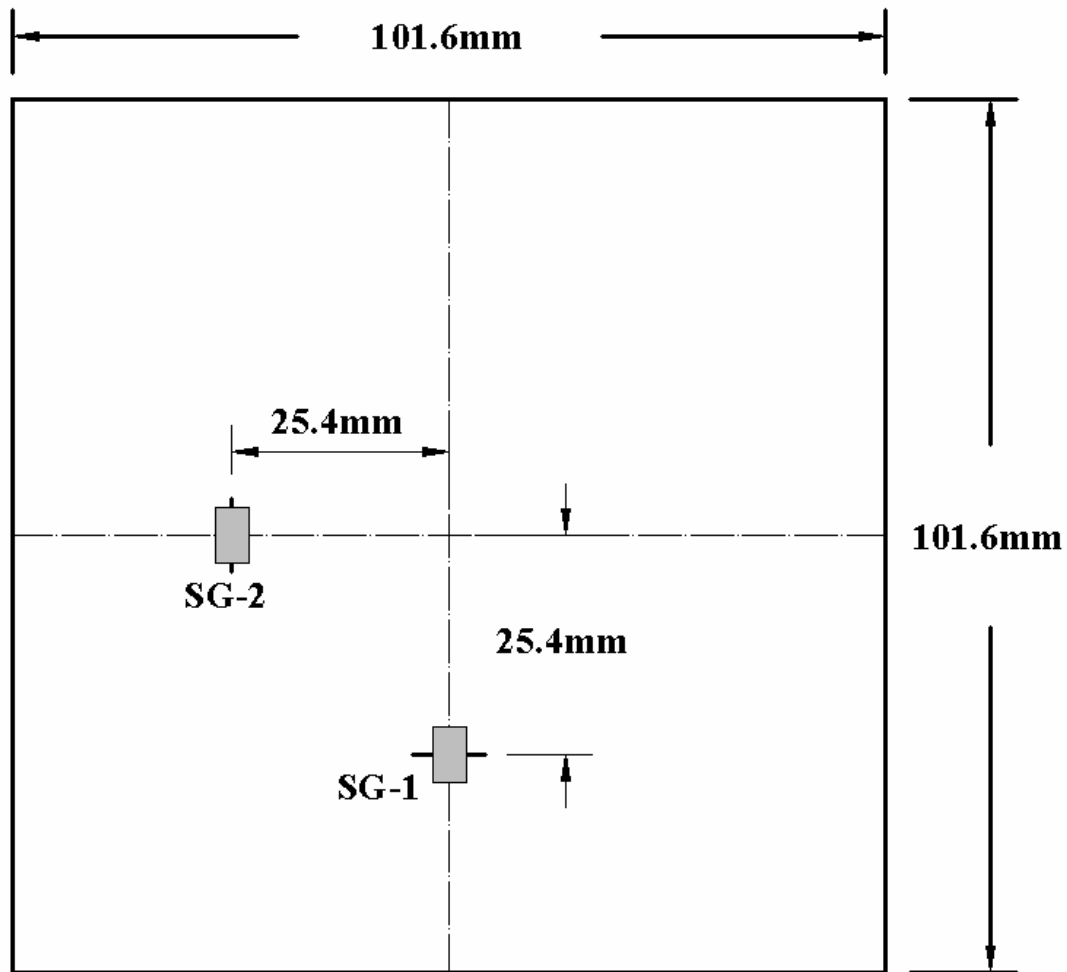
Figure 4.4-9 The strain-gage locations for low impact test specimens.

Strain time-histories at two locations for three sets of low impact test are shown in Figs 4.4-11 to 4.4-13. Comparing the strain values it is seen that strain created in non-hybrid specimens is less than strain in the hybrid specimens. GR specimens strain values are also less than hybrid types. Strain in the GL-GR-GR-GL specimens is greatest for all impact tests and followed GR-GL-GL-GR hybrid specimens. The shape of the strain-time curves is similar to that of the force-time curves of the same test. However sometimes, sudden drops and jumps were seen in the strain-time histories but not in the force-time histories. These sudden changes can be related the front surface cracks created by the low impact. These cracks sometimes propagated up to the strain gage locations and affected the sensitivity of the gage. On the other hand, strain outputs are directly related to bonding between strain-gages and specimen. The strain-gage mounting is a manual operation and depends purely on the ability of the experimenter. In some cases, because of weak bonding between strain gage and composite, strain-gage could not capture the real behavior of the specimen (GL-1 in Fig. 4.4-13). The solution to this problem is to use two strain gages on the same specimen and obtain at least one good strain-time history in case of loosing one.
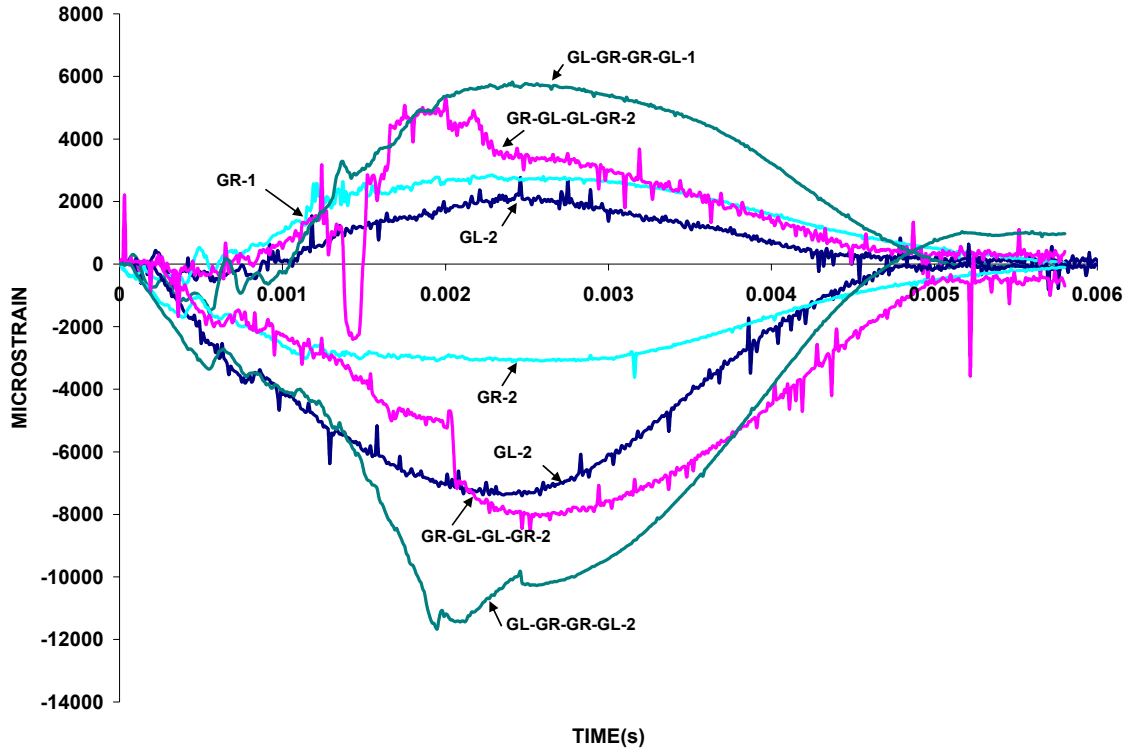
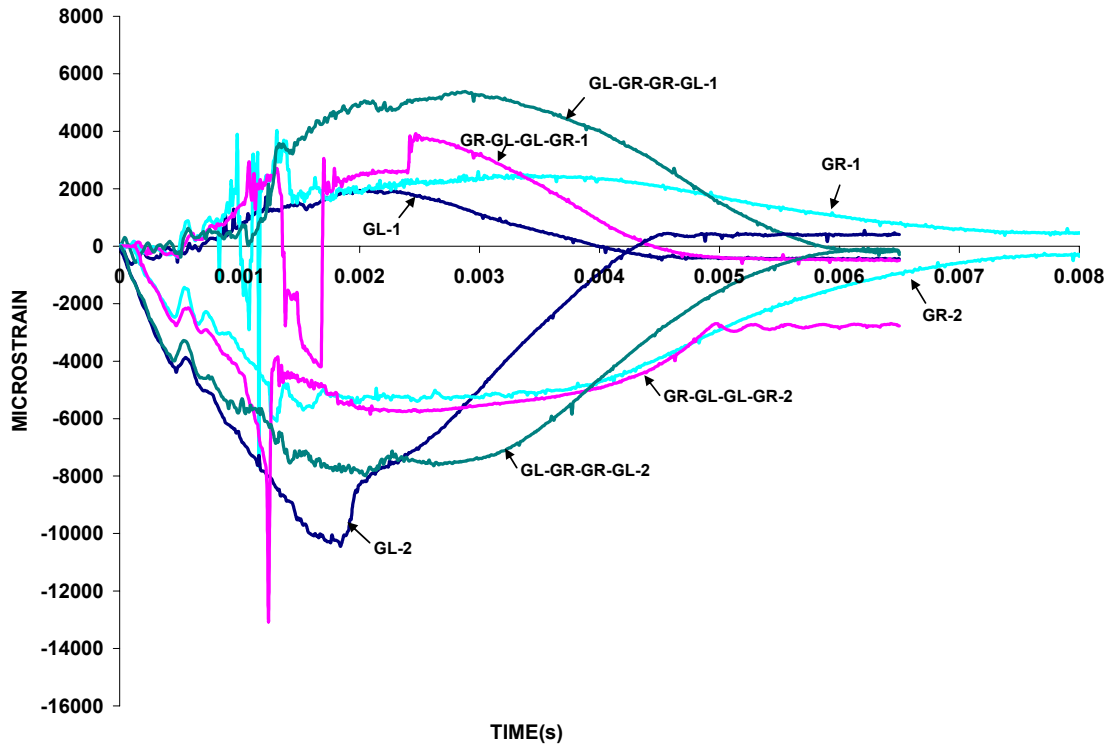Figure 4.4-11 Strain-time histories of 40J low impact tests.

Figure 4.4-12 Strain-time histories of 50J low impact tests.
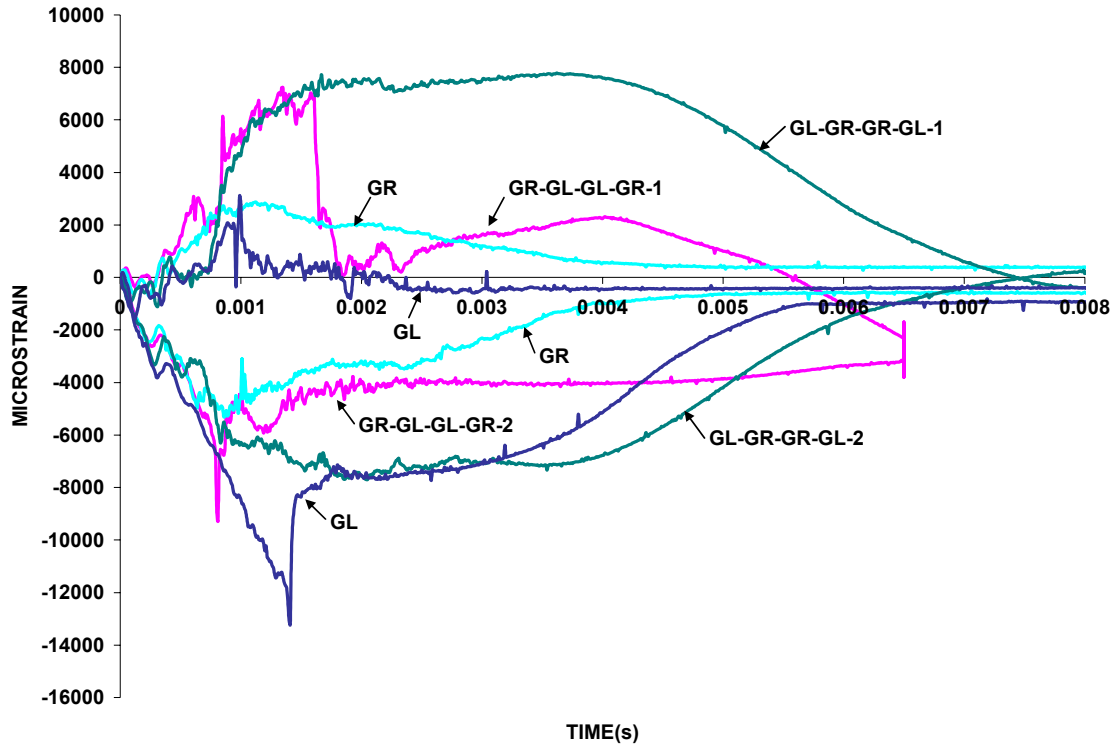
Figure 4.4-13 Strain-time histories of 100J low impact tests.

Finally, the hybrid composite panels were also subject to repeated drop-weight impact tests at an impact energy level of 32J. After each impact, the specimen was removed from drop-weight impact machine. Optical pictures were taken and the specimen was scanned with ultrasonic C-scan. The specimen was then mounted back to the drop-weight impact tester for next impact. The process was repeated until the specimen failed (i.e., perforated). In summary, the GR specimen was perforated at the end of the 6 impact; the hybrid GR/GL/GL/GR specimen was perforated after 33 impacts; the hybrid GL/GR/GR/GL specimen was perforated after 69 impacts; and the GL specimen did not perforate after 69 impact and there was no sign of significant damage to the composite. This explains that GL specimens performed best among others. After 69 impact the repeated impact test was stopped. The optical and C-scan images as well as the time histories of impact load and impact energy are shown in Figs 4.4-14 to 4.4-17 for these four types of composite panels, respectively.

GR

FRONT

BACK

ULTRASONIC C-SCANS

| 1TH | 2ND | 3RD | 4TH | 5TH | 6TH |
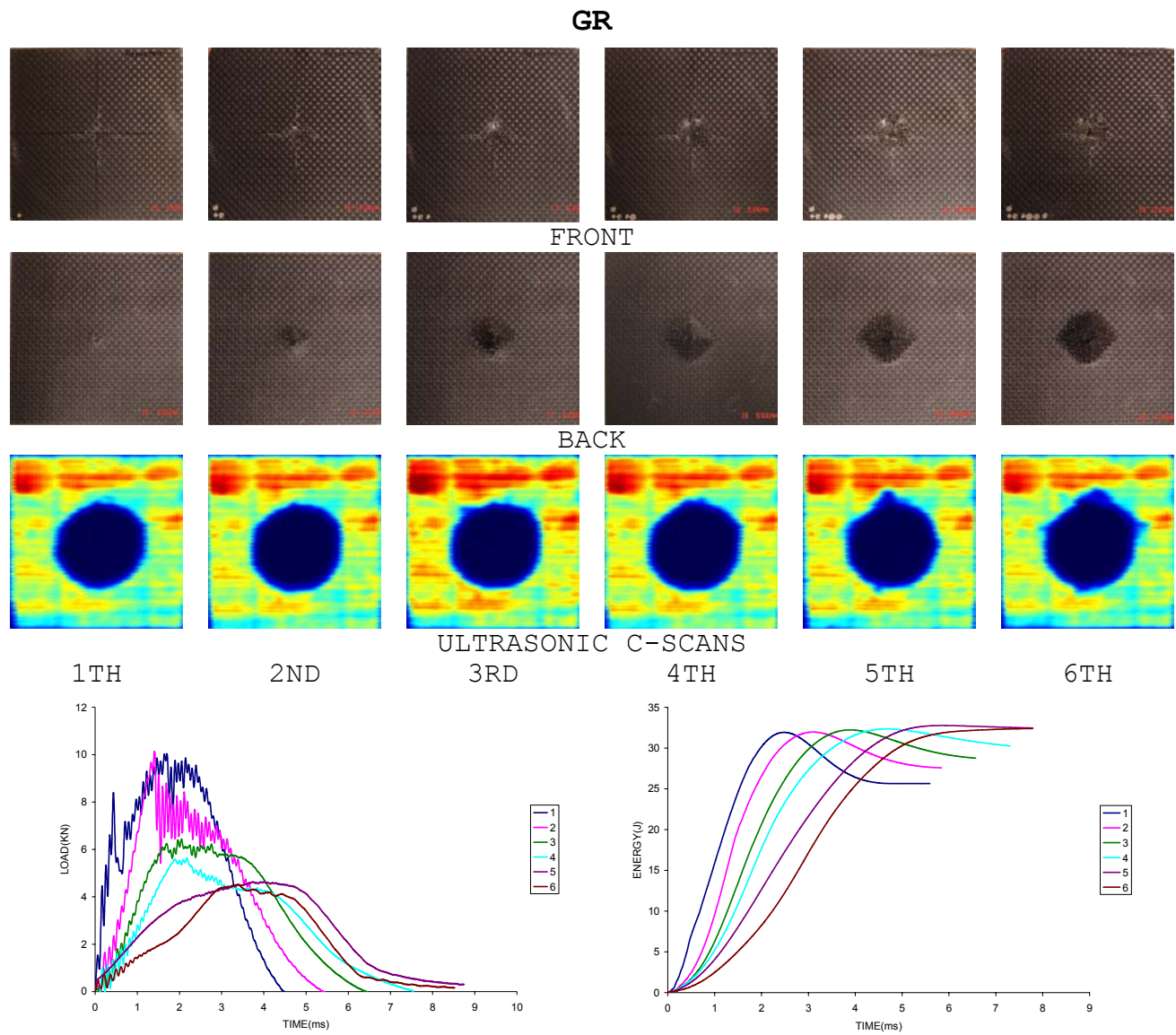
Figure 4.4-14 Repeated drop-weight impact results of a GR composite specimen (impact energy: 32J).

GR/GL/GL/GR

FRONT

BACK

ULTRASONIC C-SCANS

| 1TH | 9TH | 17TH | 25TH | 33TH |
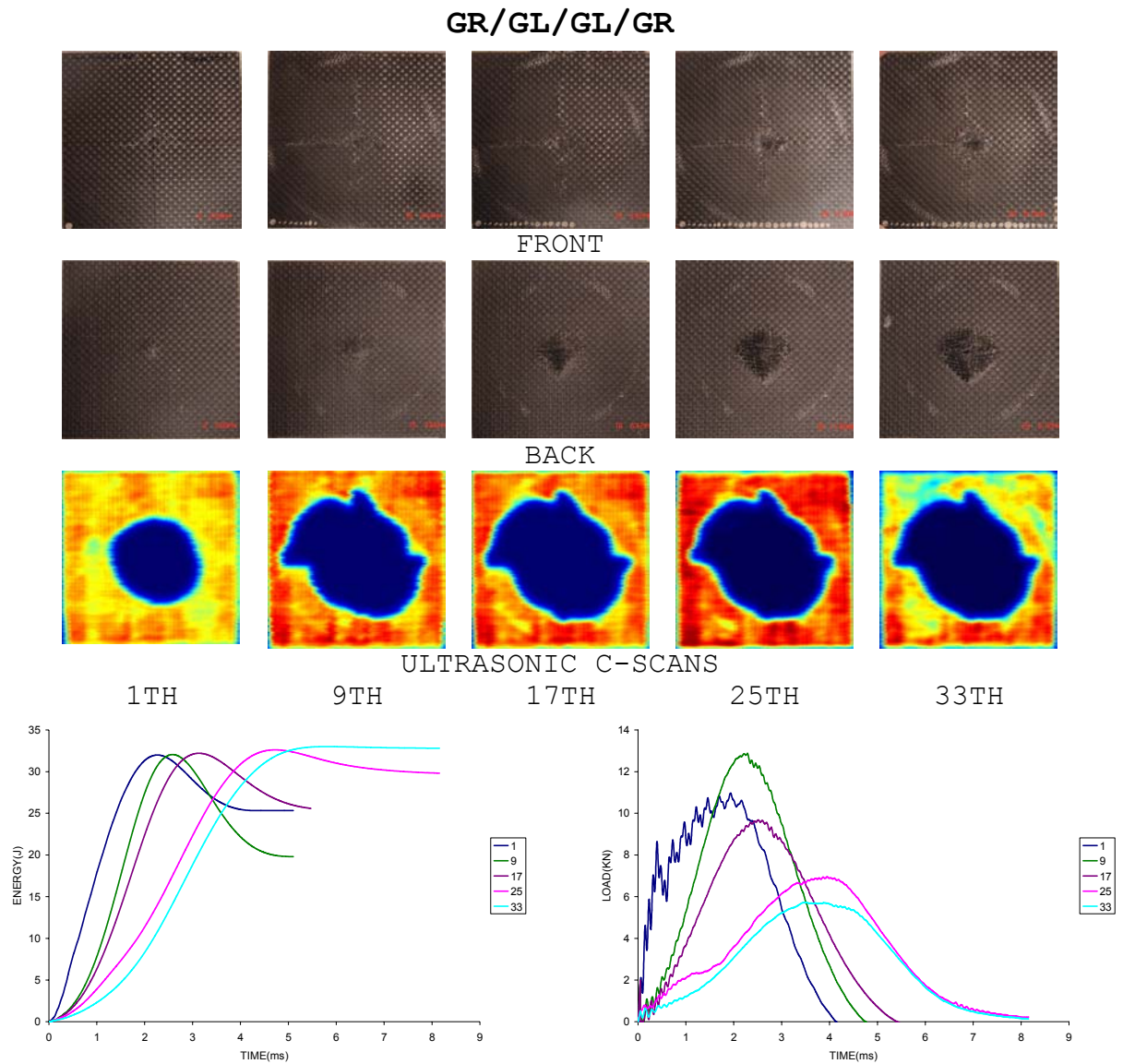
Figure 4.4-15 Repeated drop-weight impact results of a GR/GL/GL/GR hybrid composite specimen (impact energy: 32J).

GL/GR/GR/GL

FRONT

BACK

ULTRASONIC C-SCANS

| 1TH | 9TH | 17TH | 25TH | 33TH |

FRONT

BACK

ULTRASONIC C-SCANS

| 37 | 45 | 53 | 61 | 69 |

Figure 4.4-16 Repeated drop-weight impact results of a GL/ GR/GR/GL hybrid composite specimen (impact energy: 32J).

Figure 4.4-16 (continued)

GL

1TH	9TH	17TH	25TH	33TH

FRONT / BACK / ULTRASONIC C-SCANS

37	45	53	61	69

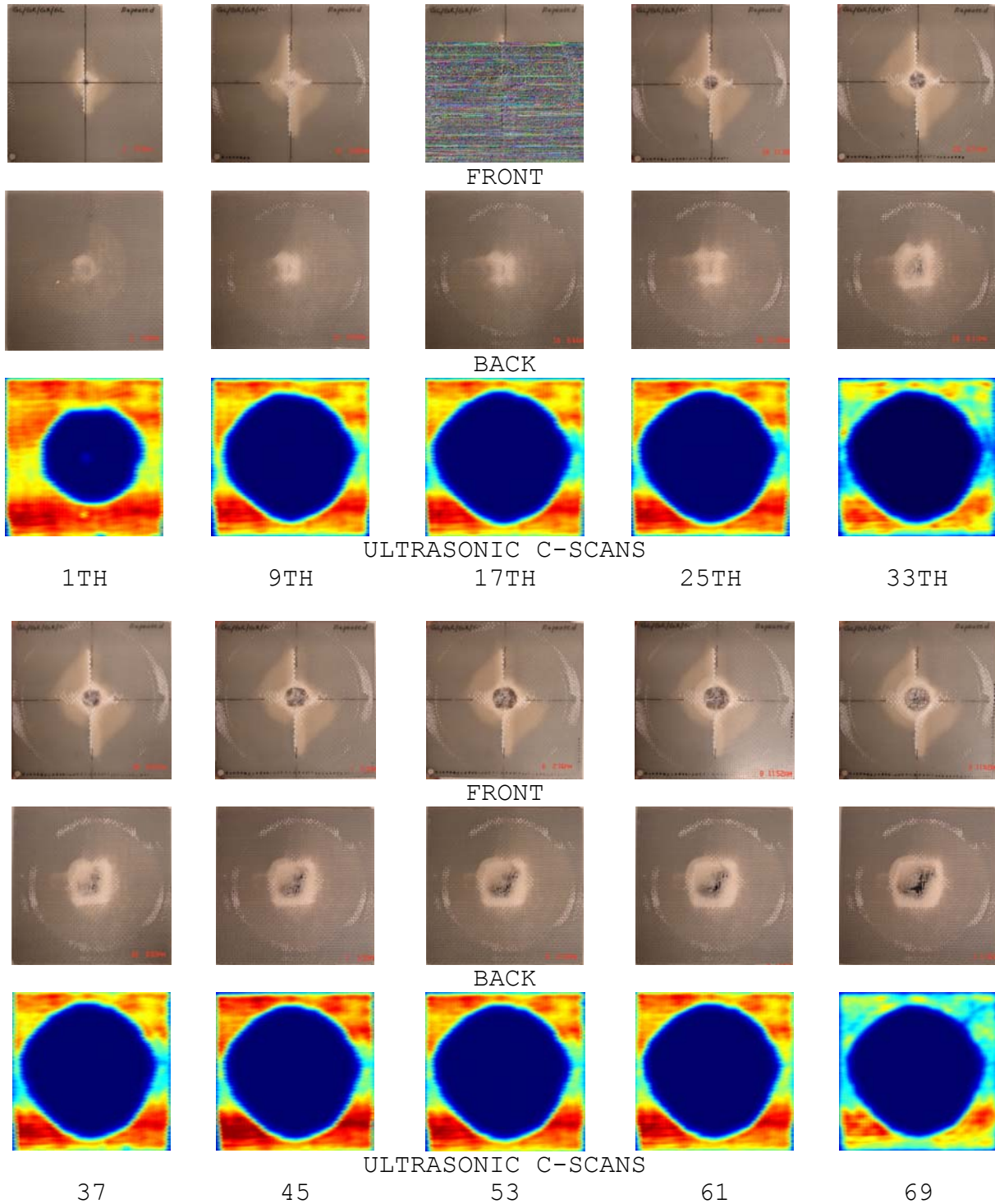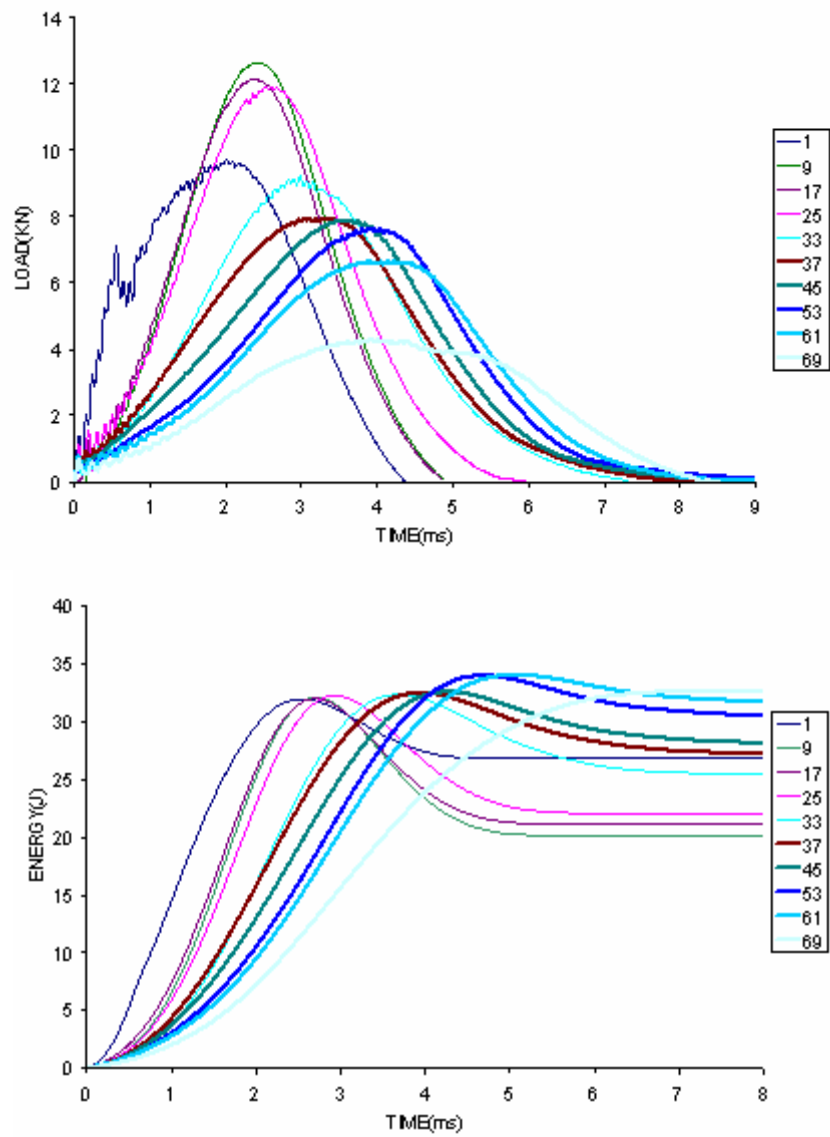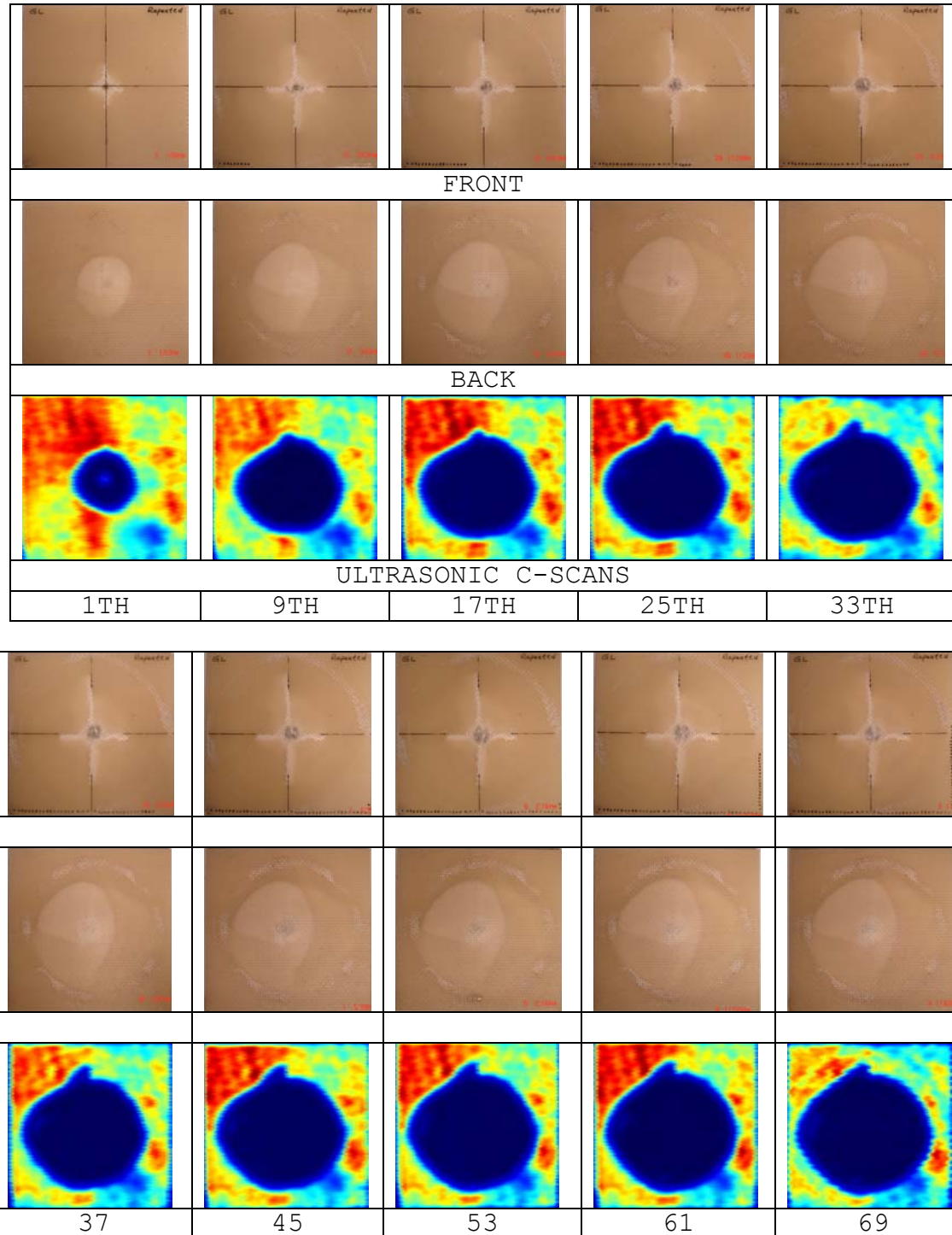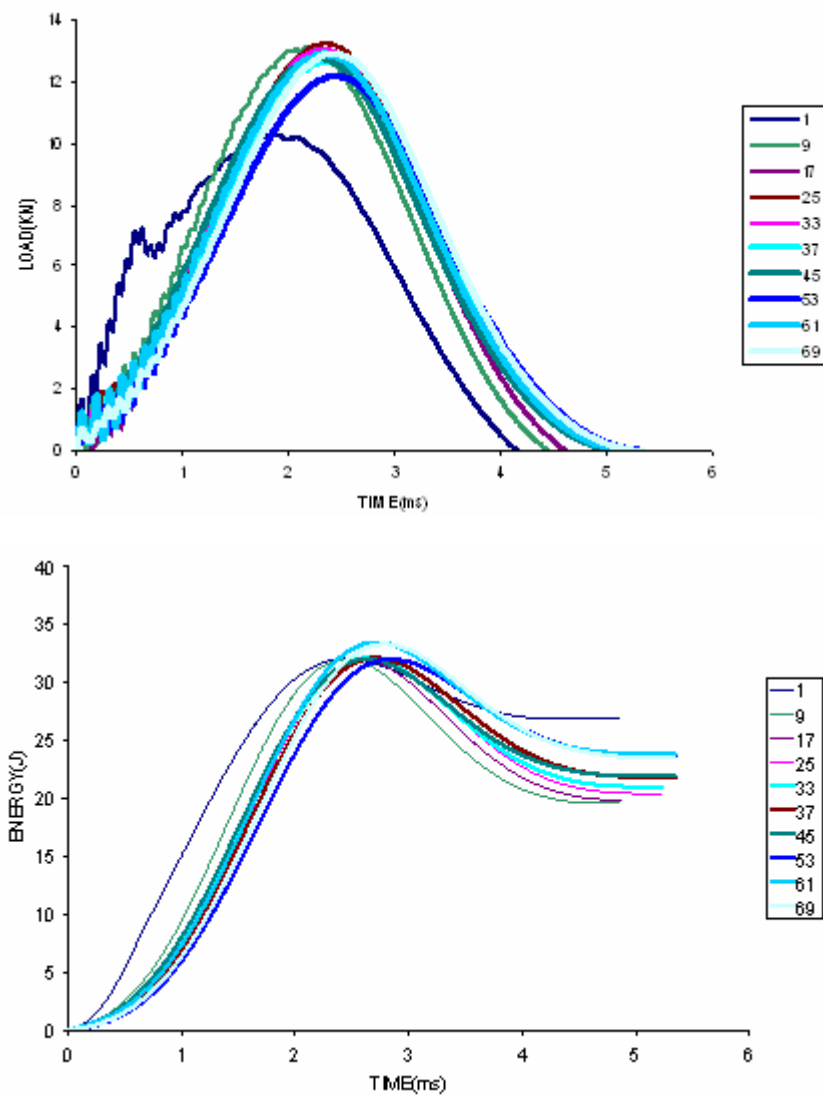Figure 4.4-17 Repeated drop-weight impact results of a GL composite specimen (impact energy: 32J).

Figure 4.4-17 (continued)

4.5: Ballistic impact tests

Experimental procedures

The last part of the experimental program is concerned about ballistic impact tests, which were conducted using an in-house high pressure gas gun. As shown in Fig. 4.5-1, high pressure helium, once released by a fast acting solenoid valve, provides the impact force needed to accelerate a 22-caliber copper bullet through the gun barrel to the desired speed. Near the muzzle of the gun barrel, two sets of diode laser-amplified photo diode pairs form two optical paths separated by 101.6 mm. The voltage changes caused by the traversing of the projectile through the two optical paths were recorded for estimating the projectile speed.
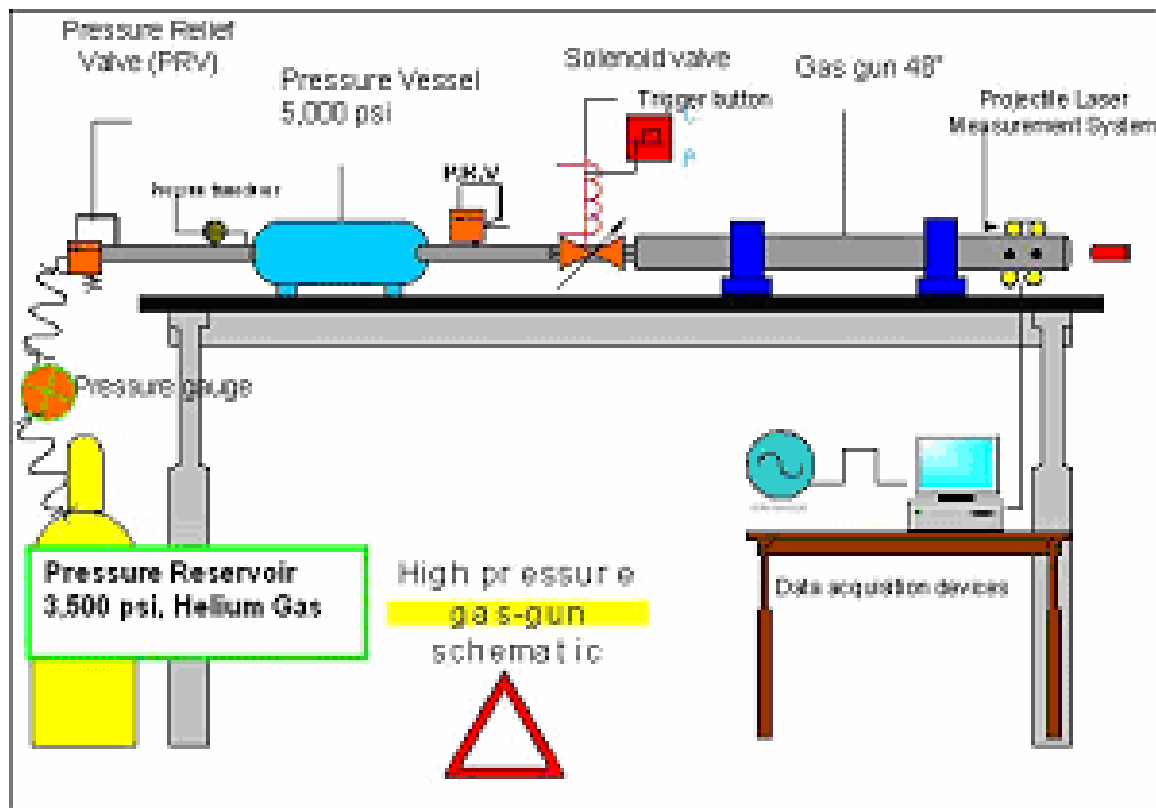
Figure 4.5-1.   Schematics of high-speed gas gun for ballistic impact tests.

The projectile then impinged onto a 24-layer composite strip specimen with dimensions shown in Fig. 4.5-2. The specimen, which was also mounted with strain gages, was clamped in a length of 50.8 mm at both ends. Thus, the ballistic impact test resembles a clamped-clamped beam under dynamic three-point bending. As shown in Fig. 4.5-2, the composite beam specimen was impacted by a 22-caliber copper projectile at the center. Two strain gages, marked as SG-1 and SG-2, respectively, were mounted on the impact side of the specimen. One of the strain gages was 25.4 mm and the other was 38.1 mm away from center. During the impact test, the projectile sometimes could not hit directly at the center. A strain gage can not survive the impact if the impingement is too close to it. Having one strain gage on each side allowed us to obtain at least one good strain measurement. Table 4.5-1 summarizes the specimen lay-up configurations and the impact velocities of three ballistic impact tests.

Figure 4.5-2.   A typical composite beam specimen mounted with two strain-gages on the ballistic impact side.

Table 4-4.1.   Parameters of ballistic impact tests. (projectile: 22-caliber copper bullet)

Test	Lay-up sequence	Impact velocity, V_0 (m/s)
1	$\left[0_3^\circ / 90_3^\circ\right]_{2S}$	120
2	$\left[0_3^\circ / 90_3^\circ\right]_{2S}$	298
3	$\left[0_3^\circ / 45_3^\circ / 90_3^\circ / -45_3^\circ\right]_{S}$	442

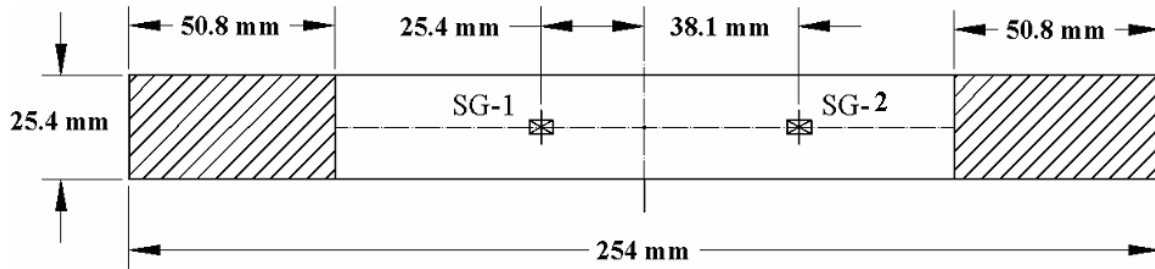### Experimental results and discussion

Figures 4.5-3 to 4.5-5 show the dynamic strain histories, post-impact optical microfractographs and the deformed 22-caliber copper projectile for the three ballistic impact tests described in Table 4.5-1. As shown in Fig. 4.5-3, no delamination was observed for Ballistic Test 1: $\left[0_3^\circ / 90_3^\circ\right]_{2S}$ cross-ply impacted at 120 m/s. Only the top layer of the composite was slightly damaged and the deformation of the projectile was not severe. For the Ballistic Test 2: $\left[0_3^\circ / 90_3^\circ\right]_{2S}$ cross-ply impacted at 298 m/s, the 22-caliber copper projectile penetrated into the ninth layer of the composite. As shown in Fig. 4.5-4, higher dynamic strains were produced; more delamination formed; and the projectile deformed more significantly.

For the case of ballistic impact Test 3: quasi-isotropic $\left[0_3^\circ / 45_3^\circ / 90_3^\circ / -45_3^\circ\right]_{S}$, the composite beam was impacted at 422 m/s. It was observed that the projectile penetrated fully and exited from the back side of the composite. There was serious damage to the composite as well as to the projectile. Figure 4.5-5 shows the strain histories, top surface and side views of the composite after impact, and the deformed projectile. Delamination occurred between all layers and was more severe around the center. The length of the delamination for all layers except the last three was approximately 30 mm. The last three layers delaminated more than the others. It should be pointed out that the sharp spikes in Fig. 4.5-5(a) might have resulted from computer glitches during data acquisition.
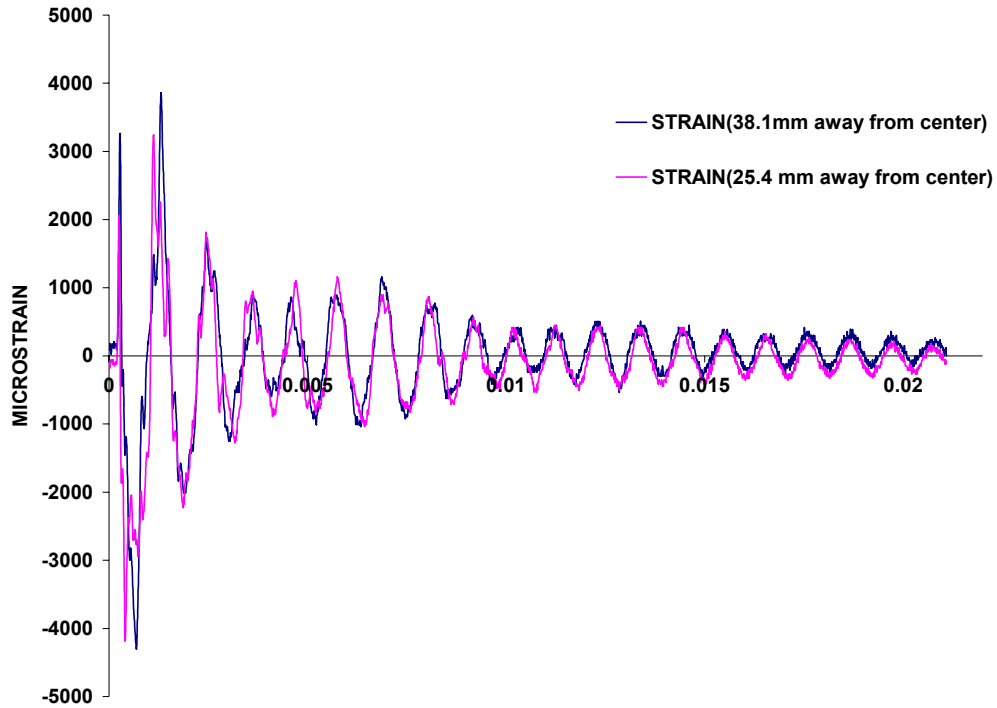
(a) dynamic strains
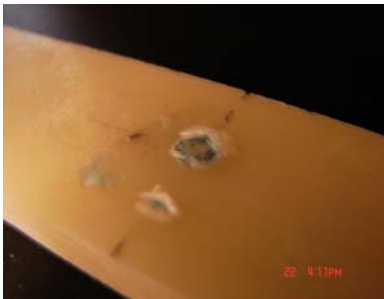
(b) perspective view   (c) side view   (d) projectile

Figure 4.5-3.   Strain histories and the post-mortem specimen and after-impact projectile of Ballistic Test 1: $\left[0_3^\circ / 90_3^\circ\right]_{2S}$ cross-ply S2 glass-toughened epoxy composite beam impacted at 120 m/s by a 22 caliber copper projectile.

(a) dynamic strains

(b) perspective view   (c) side view   (d) projectile

Figure 4.5-4.   Strain histories and the post-mortem specimen and after-impact projectile of Ballistic Test 2: $\left[0_3^\circ / 90_3^\circ\right]_{2S}$ cross-ply S2 glass-toughened epoxy composite beam impacted at 298 m/s by a 22 caliber copper projectile.
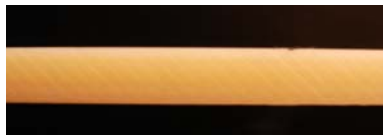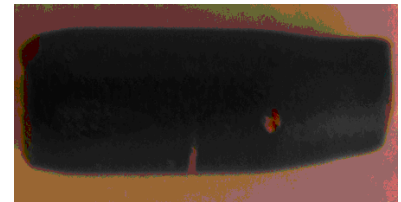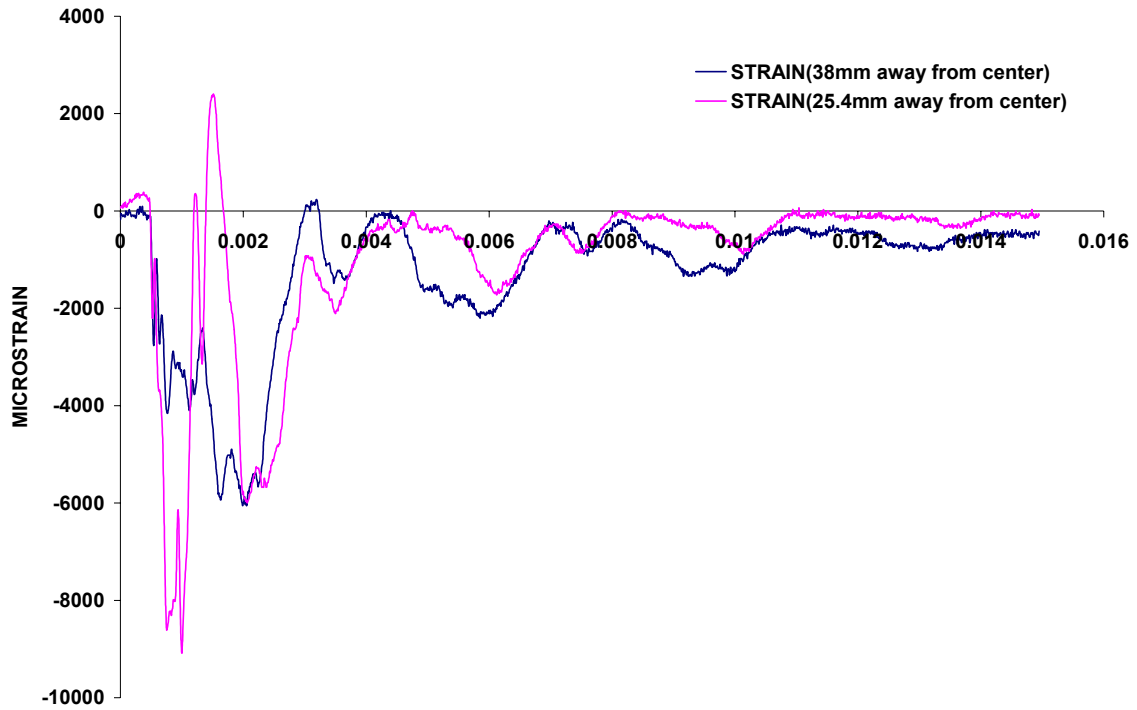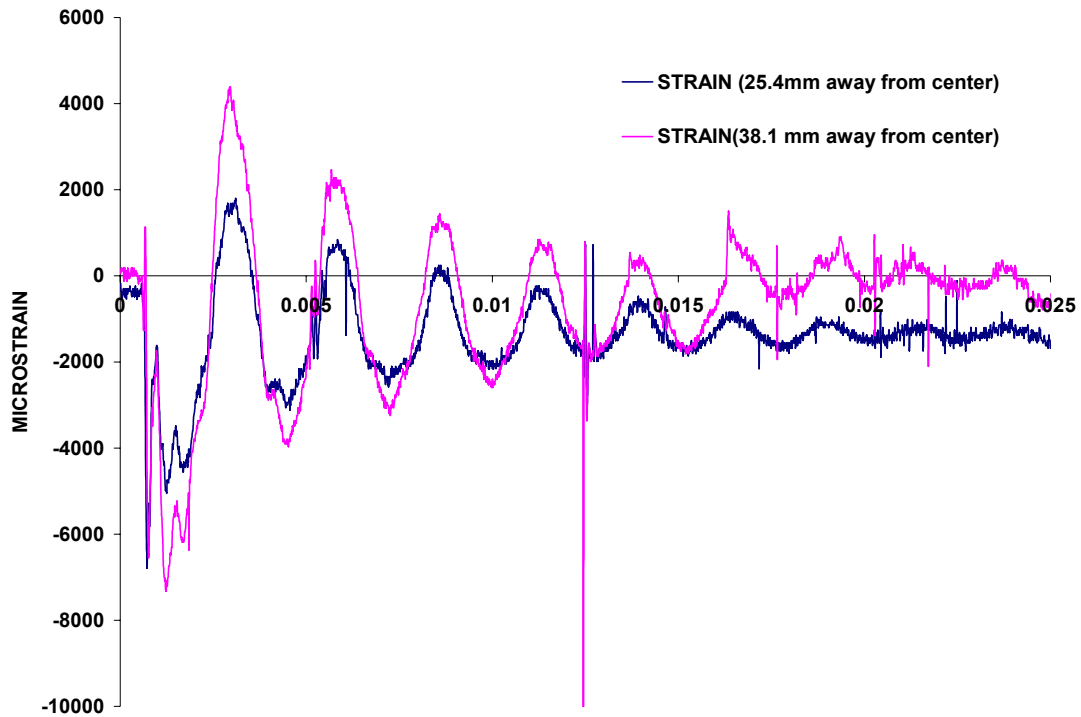
(a) dynamic strains
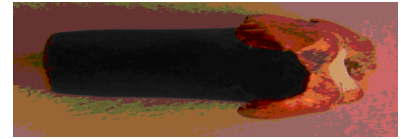
(b) perspective view   (c) side view   (d) projectile

Figure 4.5-5. Strain histories and the post-mortem specimen and after-impact projectile of Ballistic Test 3: $\left[0_3^\circ/45_3^\circ/90_3^\circ/-45_3^\circ\right]_S$ quasi-isotropic S2 glass-toughened epoxy composite beam impacted at 442 m/s by a 22 caliber copper projectile.
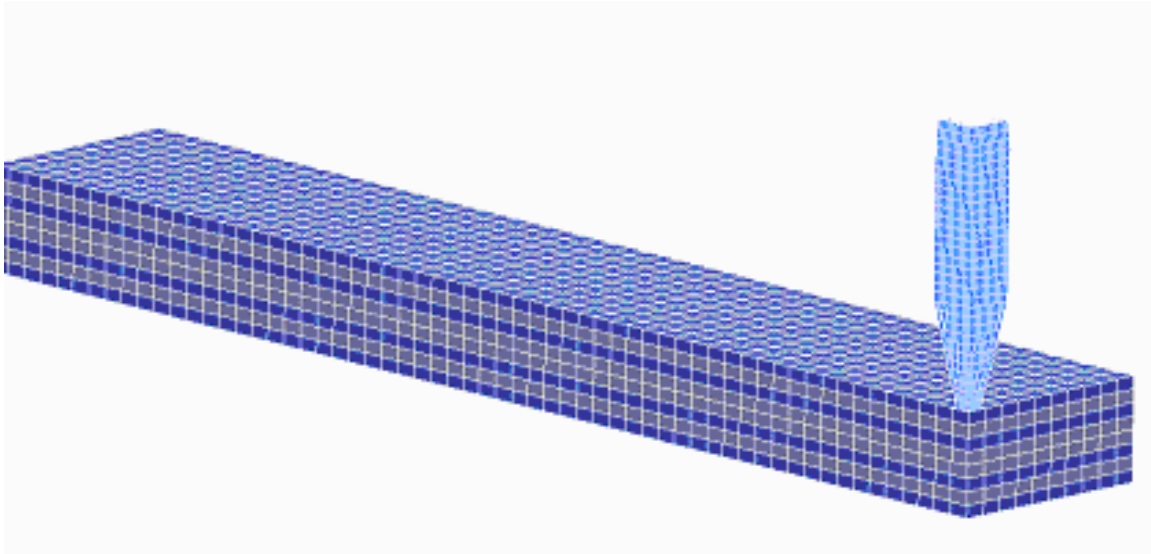
(a) ballistic impact model for the $\left[0^{\circ}_{3}/90^{\circ}_{3}\right]_{2S}$ configuration
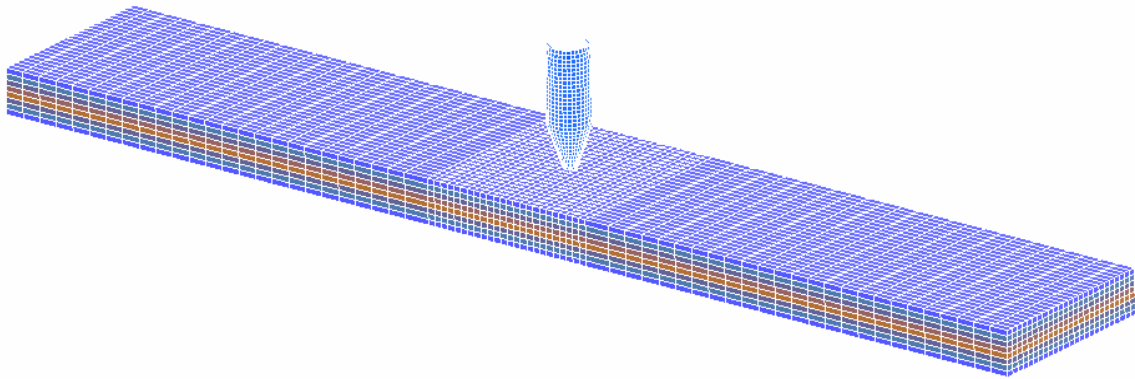
(b) ballistic impact model for the $\left[0^{\circ}_{3}/45^{\circ}_{3}/90^{\circ}_{3}/-45^{\circ}_{3}\right]_{S}$ configuration

Figure 4.5-6.   Finite element simulation models.

Figure 4.5-6.   Finite element simulations of ballistic impacts for the $\left[0^{\circ}_{3}/90^{\circ}_{3}\right]_{2S}$ and $\left[0^{\circ}_{3}/45^{\circ}_{3}/90^{\circ}_{3}/-45^{\circ}_{3}\right]_{S}$ configurations.

Dynamic finite element simulations

Figure 4.5-6 shows the LS-DYNA finite element meshes simulating (a) ballistic impact into a $\left[0^{\circ}_{3}/90^{\circ}_{3}\right]_{2S}$ cross-ply composite beam and (b) ballistic impact into a $\left[0^{\circ}_{3}/45^{\circ}_{3}/90^{\circ}_{3}/-45^{\circ}_{3}\right]_{S}$ quasi-isotropic composite beam. These two ballistic impact problems were modeled by plastic kinematic material (MAT 03) for the 22-caliber copper bullet and the Chang-Chang composite damage model (MAT 22) for the composite. The Chang-Chang model is an orthotropic material where optional brittle failure for composites can be defined [178-180]. Three failure criteria are possible in this model:

(1) <u>Matrix cracking failure</u>: $\left(\dfrac{\sigma_2}{S_2}\right)^2 + \left(\dfrac{\tau_{12}}{S_{12}}\right)^2 \geq 1$

where σ_2 and S_2 are the tensile stress and the associated tensile strength in the transverse direction whereas τ_{12} and S_{12} are the in-plane shear stress and the associated shear strength between fibers and the matrix. Once this type of failure occurs, the material constants E_2 (Young's modulus in the transverse direction), G_{12} (in-plane shear modulus in the 1-2 plane), ν_{12} and ν_{21} (Poisson's ratios in the 1-2 plane) are set to zero.

(2) <u>Fiber breakage</u>: $\left(\dfrac{\sigma_1}{S_1}\right)^2 + \left(\dfrac{\tau_{12}}{S_{12}}\right)^2 \geq 1$

where σ_1 and S_1 are the tensile stress and the associated tensile strength in the longitudinal direction whereas τ_{12} and S_{12} are again the in-plane shear stress and the associated shear strength between fibers and the matrix. After fiber breakage, E_1 (Young's modulus in the longitudinal direction), E_2, G_{12}, ν_{12} and ν_{21} are all set to zero.

(3) <u>Compression failure</u>: $\left(\dfrac{\sigma_2}{2S_{12}}\right)^2 + \left(\dfrac{\tau_{12}}{S_{12}}\right)^2 + \left[\left(\dfrac{C_2}{2S_{12}}\right)^2 - 1\right]\dfrac{\sigma_2}{C_2} \geq 1$

where C_2 is the transverse compressive strength. When this type of failure occurs, the material constants E_2, ν_{12} and ν_{21} are all set to zero.

Note that if the index 2 in any of the above criteria is replaced by index 3, the rules apply also to failures in the transverse 3-direction and the 1-3 plane.

The criterion for delamination between the composite layers is governed by the criterion: $\left[\dfrac{\max(0,\sigma_n)}{NFLS}\right]^2 + \left(\dfrac{\sigma_s}{SFLS}\right)^2 \geq 1$, where σ_n and σ_s are normal and shear stresses acting on the layer interface, respectively, while *NFLS* and *SFLS* are normal and shear strengths of the layer interface, respectively. This criterion was incorporated into LS-DYNA through

CONTACT_AUTOMATIC_SURFACE_TO_SURFACE_TIEBREAK

Additionally, ERODING_SURFACE_TO_SURFACE contact model was used between the impactor and composite. This model allows elements to be eroded when certain failure criteria are met. In this study strain-based failure criterion was used for element erosion; that is, when $\varepsilon \geq \varepsilon_{erosion}$, element was eroded and removed from calculation. In summary, the following strength values were used: $S_1 = 0.988$ GPa, $S_2 = S_3 = 0.044$ GPa, $S_{12} = S_{13} = 0.13$ GPa, $C_2 = 0.285$ GPa, $NFLS \to \infty$, $SFLS = 0.065$ GPa and $\varepsilon_{erosion} = 18\%$.

The FEM mesh in Fig. 4.5-6(a) was used to simulate Ballistic Tests 1 and 2: $\left[0_3^\circ/90_3^\circ\right]_{2S}$ cross-ply composite beam impacted at 120 and 298 m/s, respectively, by a 22-caliber copper projectile. Again, due to symmetry, only a quarter model was used. Because delamination mostly occurs at the interface where fiber orientations of the adjacent layers change and to save computational effort, instead of using 24 layers, only 8 layers with 600 elements for each layer were created. As shown in Fig. 4.5-7, the FEM predictions of strains are in good agreement with experimental results. Again perhaps due to the filtering in electronic circuitry, the experimental data were smoother and smaller than the FEM simulations.
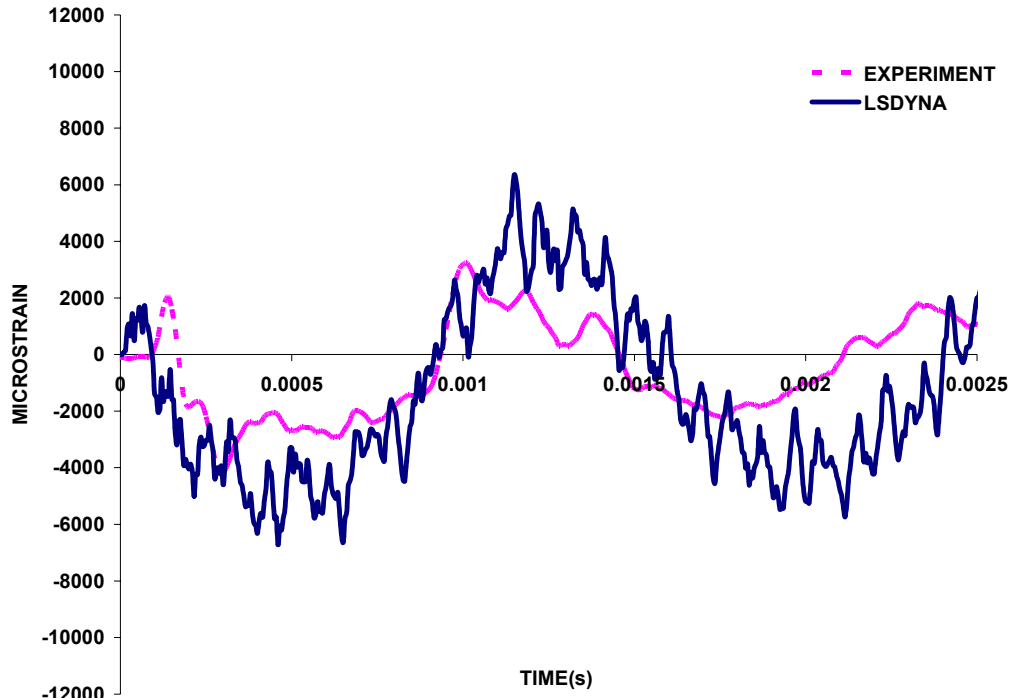
(a) Ballistic Test 1: $V_0 = 120$ m/s
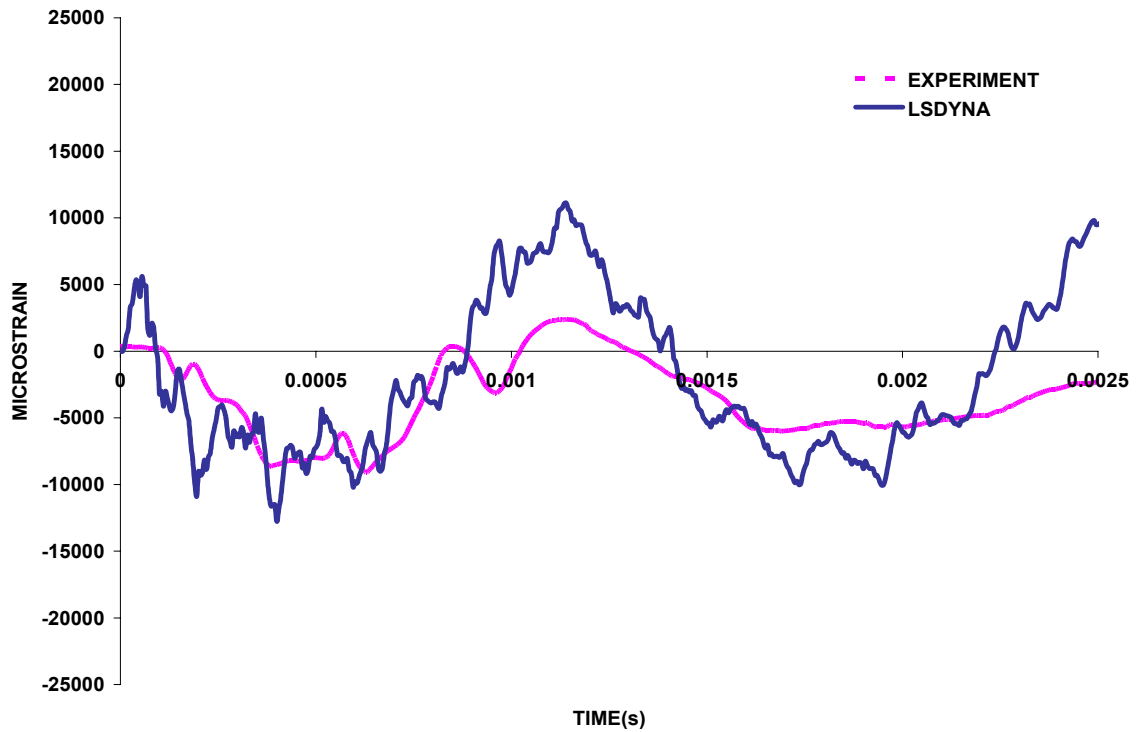
(b) Ballistic Test 2: $V_0 = 298$ m/s

Figure 4.5-7. Comparison of FEM predictions and experimental results of strain histories of Ballistic Tests 1 and 2: $\left[0_3^\circ / 90_3^\circ\right]_{2S}$ cross-ply composite beam impacted by a 22-caliber copper projectile.

For the 298 m/s case, the damage progression and beam-spanwise normal stress contours during impact are displayed in Fig. 4.5-8. Figure 4.5-9 shows the FEM prediction of time history of the projectile velocity. The result indicates that the projectile stuck to the composite specimen and the full impact duration completed in about 73 ms when the projectile velocity became zero literally.

t=0 ms

t=0.03 ms

t=0.06 ms

t=0.09 ms

t=0.12 ms

t=0.18 ms
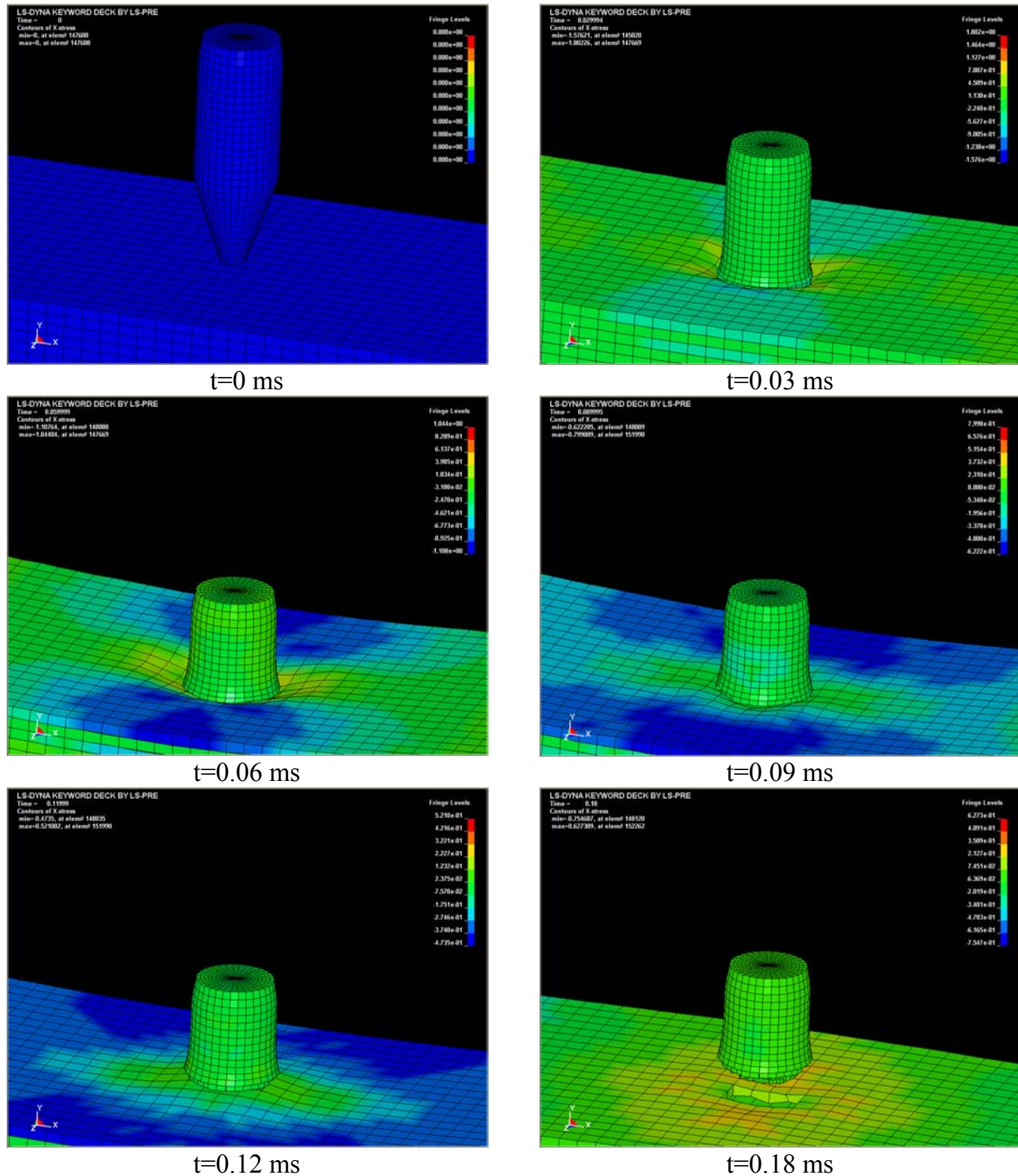
Figure 4.5-8. Impactor deformation, damage progression in the composite beam and beam-spanwise stress counters of FEM simulation for Ballistic Test 2.
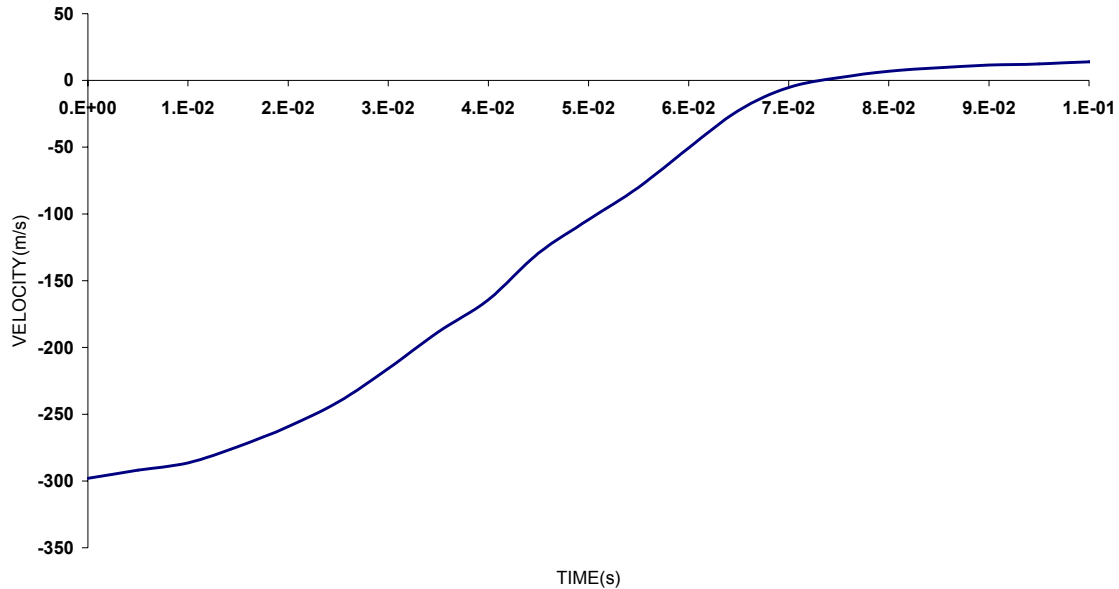
Figure 4.5-9.   FEM prediction of projectile velocity for Ballistic Test 2.

The FEM mesh in Fig. 4.5-6(b) was used to simulate Ballistic Test 3: $\left[0_3^\circ / 45_3^\circ / 90_3^\circ / -45_3^\circ \right]_S$ quasi-isotropic composite beam impacted at 442 m/s by a 22-caliber copper projectile. Full model was needed since the problem does not possess symmetry with respect to geometry and loading. Again only 8 layers with 1,875 elements for each layer were chosen to save computational effort. Notice that fine mesh was created for the area where projectile impacted the composite while the remaining part was meshed coarsely. The FEM predictions and experimental results for the Ballistic Test 3 case are compared in Figs 4.5-10 and 4.5-11 for dynamic strain, damage patterns in both front and side views and the deformation of the projectile. These two figures indicate that the FEM and experimental results are all in reasonably good agreement.

As shown in Fig. 4.5-11(d) the layers at the back tension side of the composite was delaminated extensively during the ballistic impact test. However, as depicted in Fig. 4.5-11(c), the FEM simulation showed less delamination. This may be attributed to the fact that during this ballistic impact test, the tip of the projectile was crashed into a mushroom shape, as shown in Fig. 4.5-11(f). The continuing penetration of the mushroom head into the back layers of the specimen may have gouged these layers; thus causing very severe damage. On the other hand, in order to maintain numerical stability, elements are eroded in LS-DYNA FEM computation when sufficient failure criteria were met; thus rendering the material elasticity to zero. Hence, the deformed projectile in FEM simulation, as shown in Fig. 4.5-11(e) caused less delamination.
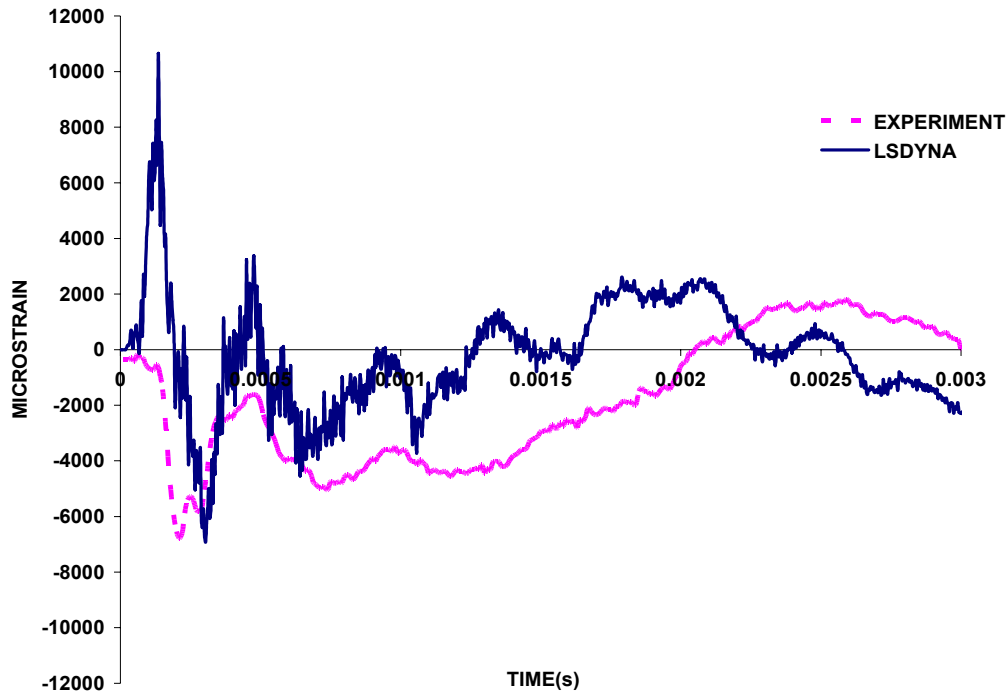
Figure 4.5-10. Comparison of FEM predictions and experimental results of strain histories of Ballistic Test 3: $\left[0_3^\circ / 45_3^\circ / 90_3^\circ / -45_3^\circ\right]_S$ quasi-isotropic composite beam

impacted at 442 m/s by a 22-caliber copper projectile.
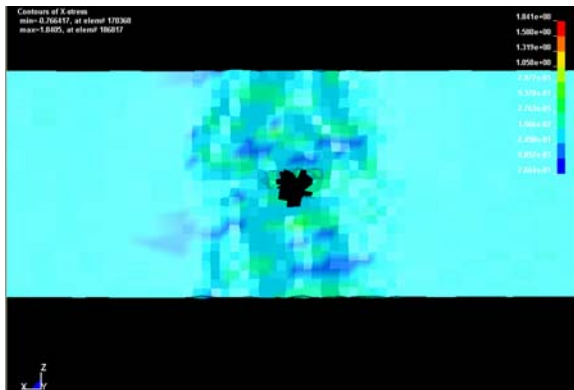
(a) stress contours @ t=0.125ms   (b) front view (experiment)
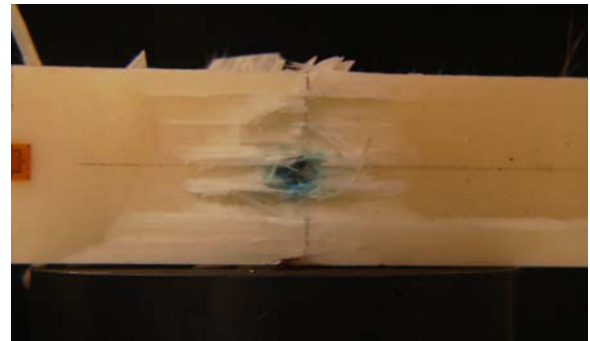
Figure 4.5-11. Comparisons of post impact damage patterns and projectile deformations of FEM and experimental results of Ballistic Test 3.
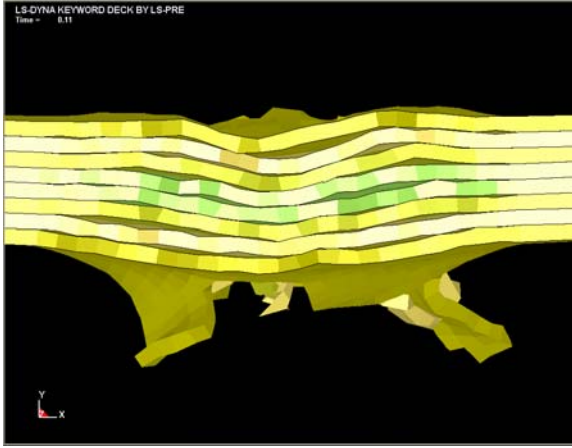
(c) side-view (FEM)
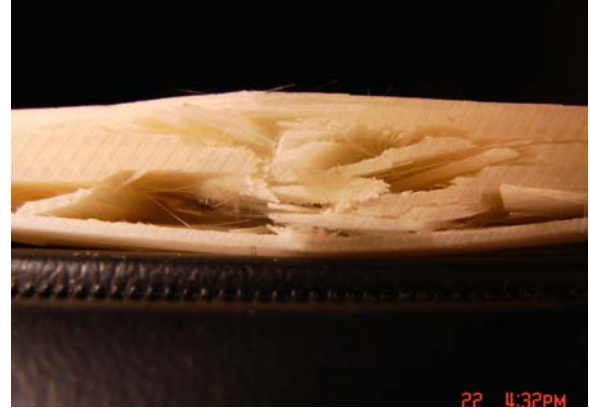
(d) side view (experiment)
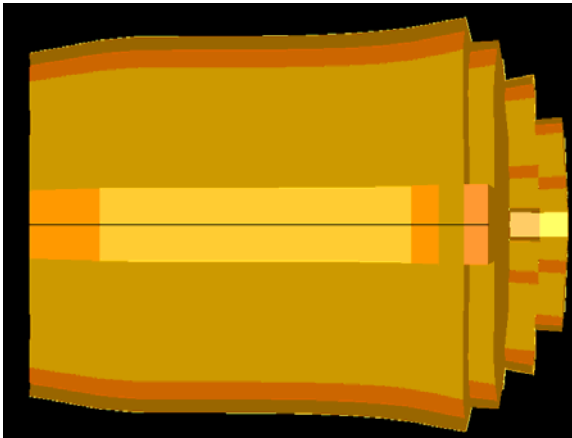
(e) projectile (FEM)

(f) projectile (experiment)

Figure 4.5-11. (continued)

Ballistic limit velocity V_{50}

Once the proposed damage-induced nonlinear anisotropic constitutive relation are verified by experimental results, the model can be employed in engineering design. For instance, we can use this model to predict the ballistic limit velocity V_{50} of armors made of this toughened composite. Here V_{50} is defined as the velocity required for a projectile to reliably penetrate (i.e., at least 50%) a piece of armor. Consider composite beams made of $\left[0^\circ\right]_{24}$ S2 glass-toughened epoxy with three different thicknesses: 6, 13 and 25 mm. As shown in Fig. 4.5-12, our LS-DYNA based FEM analyses predict the corresponding ballistic limit velocities as 300, 500 and 950 m/s, respectively. Indeed, the simulations can be used to conclude that for this class of composite beams, the V_{50} vs thickness relation is almost linear, as illustrated in Fig. 4.5-13.

6 mm (V_{50}=300 m/s)   13 mm (V_{50}=500 m/s)   25 mm (V_{50}=950 m/s)
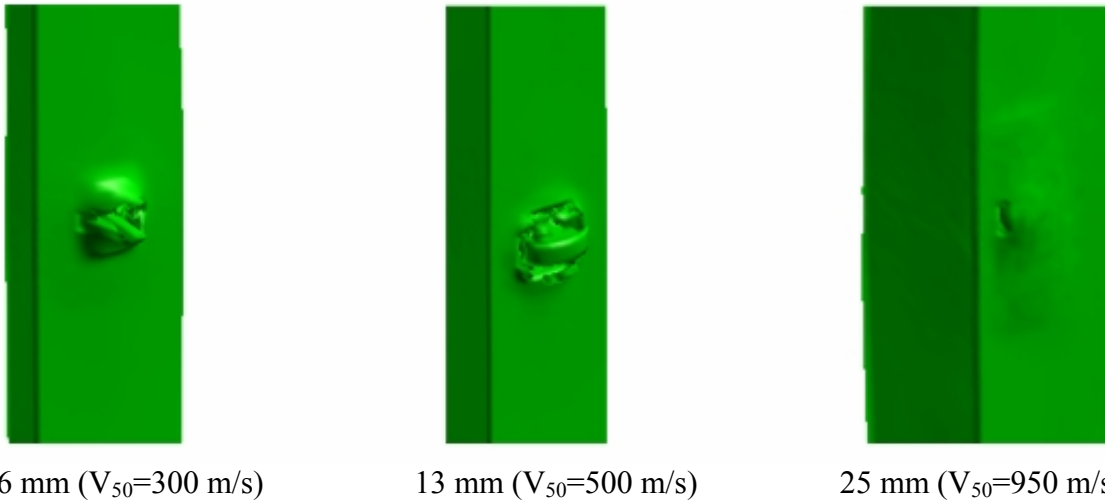
Figure 4.5-12. FEM estimated ballistic limit velocities (V_{50}) for S2 glass/ toughened epoxy composite beams with different thicknesses.
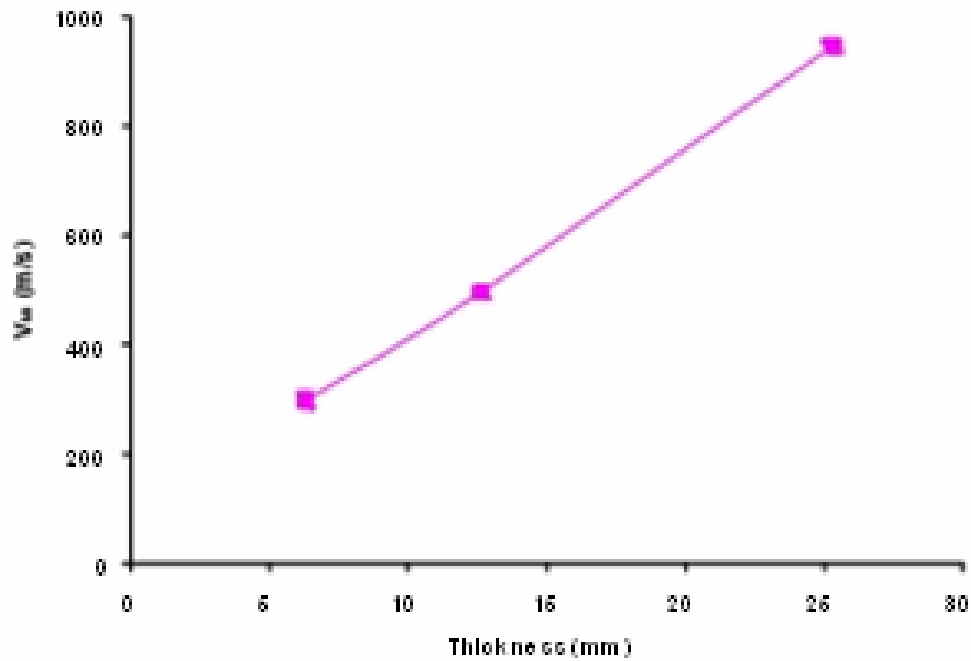
Figure 4.5-13. The almost linear V_{50} *vs* thickness relation, as predicted by finite element simulations.

4.6: Conclusions

S2-glass reinforced toughened epoxy composites and hybrid S2-glass/IM7-graphite reinforced API SC-79 epoxy composites impacted at drop-weight (i.e., low) and ballistic (i.e., high) velocities were studied experimentally and numerically. Based on this study, the following conclusions can be drawn:

a) The cross-ply configurations: $\left[0_3^\circ/90_3^\circ\right]_{2S}$, $\left[0_2^\circ/90_2^\circ\right]_{3S}$ or $\left[90_2^\circ/0_2^\circ\right]_{3S}$ have higher low impact resistance than the other configurations.

b) The time histories of impact force, dynamic strain, damage pattern and projectile deformation obtained from experiments and FEM simulations are in good agreement.

c) Delamination was the predominant damage mode for low-velocity drop-weight impact tests; whereas in addition to delamination, matrix failure, fiber breakage and projectile deformation were also observed in ballistic impact tests.

d) The ballistic limit velocity V_{50} depends almost linearly on the thickness of the composite beam.

e) The S2-glass fiber reinforced composites provide the best resistance to impact. It follows by GL/GR/GR/GL hybrid composites, GR/GL/GL/GR hybrid composites, and the the GR composites. However, the main reason for using GR is because of its high strength and high stiffness, which are important material characteristics for enhancing damage tolerance.

5. References

1. *Army Science and Technology Master Plan 2001, Vol. I*, http://www.saalt.army.mil/sard-zt/ASTMP01/astmp01.htm.

2. Fink BK. Performance metrics for composite integral armor. *J. of Thermoplastic Composite Materials*. 2000; 13: 417-31.

3. Abrate S. *Impact on Composite Structures*. Cambridge University Press, Cambridge, UK, 1998.

4. Horton RE and McCarty JE. Damage tolerance of composites. *Engineered Materials Handbook*, Vol. 1: <u>Composites</u>. ASM International, Metals Park, OH, 1987: 259-67.

5. Sierakowski RL and Newaz GM. *Damage Tolerance in Advanced Composites*. Technomic Publishing, Lancaster, PA, 1995.

6. Fink BK, Monib AM and Gillespie JW, Jr. *Damage Tolerance of Thick-Section Composites Subjected to Ballistic Impact, ARL-TR-2477*, U.S. Army Research Laboratory, May 2001.

7. Liu D, Raju BB and Richman T. Impact perforation resistance of laminated and assembled composite plates. *Int. J. of Impact Engineering* 2000; 24(6-7), 733-46.

8. Liu D, Raju BB and You J. Thickness effects in pinned joints for composites. *J. of Composite Materials* 1999; 33(1): 2-21.

9. Liu D, Raju BB and Dang X. Size effects on impact response of composite laminates. *Int. J. of Impact Engineering* 1998; 21(10), 837-54.

10. Chun H, Lee S and Daniel IM. Analysis of nonlinear flexural behavior of thick composites with fiber waviness. *Thick Composites for Load Bearing Structures*, AMD-235, Rajapakse, YDS and Kardomateas, GA (Eds). The 1999 ASME International Mechanical Engineering Congress and Exposition, Nashville, TN, November 14-19, 1999, pp. 9-20.

11. Wooh SC and Daniel IM. Wave propagation in composite materials with fibre waviness. *Ultrasonics* 1995; 33(1): 3-10.

12. Balasubramaniam K and Whitney SC. Ultrasonic through-transmission characterization of thick fibre-reinforced composites. *NDT&E International* 1996; 29(4): 225-36.

13. Lu X, Kim KY and Sachse W. *In situ* determination of elastic stiffness constants of thick composites. *Composites Science and Technology* 1997; 57: 753-62.

14. Mouritz AP, Townsend C and Shan Khan MZ. Non-destructive detection of fatigue damage in thick composites by pulse-echo ultrasonics. *Composites Science and Technology* 2000; 60: 23-32.

15. Gagneja S, Gibson RF and Ayorinde EO. Design of test specimens for the determination of elastic through-thickness shear properties of thick composites from measured modal vibration frequencies. *Composites Science and Technology* 2001; 61: 679-87.

16. Epstein JS and Deason VA. Impact wave propagation in a thick composite plate using dynamic moiré interferometry. *Optics and Lasers in Engineering* 1992; 17(1): 35-46.

17. Kim KH, Klann RT and Raju BB. Fast neutron radiography for composite materials evaluation and testing. *Nuclear Instruments & Methods in Physics Research, Sec. A* 1999; 422: 929-32.

18. Ball RJ and Almond DP. The detection and measurement of impact damage in thick carbon fibre reinforced laminates by transient thermography. *NDT&E International* 1998; 31(3): 165-73.

19. Dyka CT and Badaliance R. Damage in marine composites caused by shock loading. *Composites Science and Technology* 1998; 58: 1433-42.

20. Sun CT and Potti SV. A simple model to predict residual velocities of thick composite laminates subject to high velocity impact. *Int. J. of Impact Engineering* 1996; 18(3), 339-53.

21. Zhou G. Static behaviour and damage of thick composite laminates. *Composites Structures* 1996; 36: 13-22.

22. Daniel IM, Hsiao HM and Wooh SC. Failure mechanisms in thick composites under compressive loading. *Composite Part B: Engineering* 1996; 27: 543-52.

23. Hsiao HM and Daniel IM. Effect of fiber waviness on stiffness and strength reduction of unidirectional composites under compressive loading. *Composites Science and Technology* 1996; 56: 581-93.

24. Hsiao HM and Daniel IM. Elastic properties of composites with fiber waviness. *Composite Part A: Applied Science and Manufacturing* 1996; 27: 931-41.

25. Duffort L, Grédiac M and Surrel Y. Experimental evidence of the cross-section warping in short composite beams under three point bending. *Composites Structures* 2001; 51: 37-47.

26. Duffort L, Drapier S and Grédiac M. Closed-form solution for the cross-section warping in short beams under three point bending. *Composites Structures* 2001; 52: 233-46.

27. Grédiac M, Auslender F and Pierron F. Applying the virtual fields method to determine the through-thickness moduli of thick composites with a nonlinear shear response. *Composite Part A: Applied Science and Manufacturing* 2001; 32: 1173-25.

28. Pierron F, Zhavoronok S and Grédiac M. Identification of the through-thickness properties of thick laminated tubes using the virtual fields method. *Int. J. of Solids and Structures* 2000; 37: 4437-53.

29. Pierron F and Grédiac M. Identification of the through-thickness moduli of thick composites from the whole-field measurements using the Iosipescu fixtures: theory and simulations. *Composite Part A: Applied Science and Manufacturing* 2000; 31: 309-18.

30. Valoor MT and Chandrashekhara K. A thick composite-beam model for delamination prediction by the use of neural networks. *Composites Science and Technology* 2000; 60: 1773-79.

31. Nishiwaki T, Yokoyama A, Maekawa Z and Hamada H. A quasi-three-dimensional elastic wave propagation analysis for laminated composites. *Composites Structures* 1995; 32: 635-40.

32. Bogdanovich AE and Deepak BP. Three-dimensional analysis of thick composite plates with multiple layers. *Composite Part B: Engineering* 1997; 28: 345-57.

33. Matthews FL (Ed) *Joining Fibre-Reinforced Plastics*. Elsevier Applied Science, Barking, UK, 1987.

34. Benatar A, Gillespie JW, Jr and Kedward K. Joining of composites. Ch. 12 in *Advanced Composites Manufacturing*. Gutowski TG (Ed). Wiley, New York, 1997.

35. Schwartz MM. *Joining of Composite Matrix Materials*. ASM International, Materials Park, OH, 1994.

36. Kedward K (Ed). *Joining of Composite Materials, ASTM STP 749*. American Society for Testing and Materials, Philadelphia, 1981.

37. Lubin G (Ed). *Handbook of Fibreglass and Advanced Plastic Composites*. Van Norstrand Reinhold, New York, 1969.

38. Hancox NL. Introduction to fibre composite hybrids. Ch. 1 in *Fibre Composite Hybrid Materials*. Hancox NL (Ed). Applied Science Publishers, London, 1981.

39. Chou TW. *Microstructural Design of Fiber Composites*. Cambridge University Press, New York, 1992: 285-374.

40. Summerscales J and Short D. Carbon fibre and glass fibre hybrid reinforced plastics. *Composites*, 1978; 9: 157-66.

41. Lovell DR. Reinforcements. Ch. 2A in *Fibre Composite Hybrid Materials*. Hancox NL (Ed). Applied Science Publishers, London, 1981.

42. Manders PW and Bader MG. The strength of hybrid glass/carbon fibre composites. *J. of Materials Science* 1981; 16: 2233-45.

43. Rossettos JN and Shen X. On the axial and interfacial shear stresses due to thermal mismatch in hybrid composite sheets. *Composites Science and Technology* 1995; 54: 417-22.

44. Khatri SC and Koczak MJ. Thick-section AS4-graphite/E-glass/PPS hybrid composites: part I. tensile behavior. *Composites Science and Technology* 1996; 56: 181-92.

45. Khatri SC and Koczak MJ. Thick-section AS4-graphite/E-glass/PPS hybrid composites: part II. flexural response. *Composites Science and Technology* 1996; 56: 473-82.

46. Cheon SS, Lim TS and Lee DG. Impact energy absorption characteristics of glass fiber hybrid composites. *Composite Structures* 1999; 46: 267-78.

47. Park R and Jang J. Impact behavior of aramid fiber/glass fiber hybrid composite: evaluation of impact behavior using delamination area. *J. of Composite Materials* 2000; 34 [13]: 1117-35.

48. Naik NK, Ramasimha R, Arya H, Prabhu SV and Sharma Rao N. Impact response and damage tolerance characteristics of glass-carbon/epoxy hybrid composite plates. *Composite Part B: Engineering* 2001; 32: 565-74.

49. Shan Y and Liao K. Environmental fatigue of unidirectional glass-carbon fiber reinforced hybrid composite. *Composite Part B: Engineering* 2001; 32: 355-63.

50. Shan Y, Lai KF, Wan KT and Liao K. Static and dynamic fatigue of glass-carbon hybrid composites in fluid environment. *J. of Composite Materials* 2002; 36(2): 159-172.

51. Zinoviev PA and Smerdov AA. Ultimate properties of unidirectional fiber composites. *Composites Science and Technology* 1999; 59: 625-34.

52. Thwe MM and Liao K. Effects of environmental aging on the mechanical properties of bamboo-glass fiber reinforced polymer matrix hybrid composites. *Composite Part A: Applied Science and Manufacturing* 2002; 33: 43-52.

53. Sreekala MS, George J, Kumaran MG and Thomas S. The mechanical performance of hybrid phenol-formaldehyde-based composites reinforced with glass and oil palm fibres. *Composites Science and Technology* 2002; 62: 339-53.

54. Stewart RW, Verijenko VE and Adali S. Analysis of the in-plane properties of hybrid glass/carbon woven fabric composites. *Composites Structures* 1997; 39(3-4): 319-28.

55. Scida D, Aboura Z, Benzeggagh ML and Bocherens E. Prediction of the elastic behaviour of hybrid and non-hybrid woven fabric composites. *Composites Science and Technology* 1997; 57: 1727-40.

56. Lee SH, Noguchi H and Cheong SK. Tensile properties and fatigue characteristics of hybrid composites with non-woven carbon tissue. *Int. J. of Fatigue* 2002; 24: 397-405.

57. Morii T, Hamada H, Desaeger M, Gotoh A, Yokoyama A, Verpoest I and Maekawa Z. Damage tolerance of glass mat/epoxy laminates hybridized with flexible resin under static and impact loading. *Composites Structures* 1995; 32: 133-39.

58. Hwang SF and Mao CP. Failure of delaminated interply hybrid composite plates under compression. *Composites Science and Technology* 2001; 61: 1513-27.

59. Hwang SF and Mao CP. The delamination buckling of single-fibre system and interply hybrid composites. *Composites Structures* 1999; 46: 279-87.

60. Hwang SF and Shen BC. Opening-mode interlaminar fracture toughness of interply hybrid composite materials. *Composites Science and Technology* 1999; 59: 1861-69.

61. Park R and Jang J. The effects of hybridization on the mechanical performance of aramid/polyethylene interply fabric composites. *Composites Science and Technology* 1998; 58: 1621-28.

62. Kim JK, Sham ML, Sohn MS and Hamada H. Effect of hybrid layers with different silane coupling agents on impact response of glass fabric reinforced vinylester matrix composites. *Polymer* 2001; 42: 7455-60.

63. Fu SY, Mai YW, Lauke B and Yue CY. Synergistic effect on the fracture toughness of hybrid short glass fiber and short carbon fiber reinforced polypropylene composites. *Materials Science and Engineering A* 2002; 323: 326-35.

64. Fu SY, Xu G and Mai YW. On the elastic modulus of hybrid particle/short-fiber/polymer composites. *Composite Part B: Engineering* 2002; 33: 291-99.

65. Fu S, Wu P. and Han Z. Tensile strength and rupture energy of hybrid poly(methylvinylsiloxane) composites reinforced with short PET fibers and wollastonite whiskers. *Composites Science and Technology* 2002; 62: 3-8.

66. Saha N, Banerjee AN and Mitra BC. Tensile behaviour of unidirectional polyethylene-glass fibers PMMA composite laminates. *Polymer* 1996: 37(4): 699-701.

67. Saha N and Banerjee AN. Stress relaxation behaviour of unidirectional polyethylene-glass fibers PMMA composite laminates. *Polymer* 1996: 37(20): 4633-38.

68. Li Y, Xian XJ, Choy CL, Guo M and Zhang Z. Compressive and flexural behavior of ultra-high-modulus polyethylene fiber and carbon fiber hybrid composites. *Composites Science and Technology* 1999; 59: 13-18.

69. Park R and Jang J. Stacking sequence effect of aramid-UHMPE hybrid composites by flexural method. *Polymer Testing* 1997; 16: 549-62.

70. Larsson F and Svensson L. Carbon, polyethylene and PBO hybrid fibre composites for structural lightweight armour. *Composite Part A: Applied Science and Manufacturing* 2002; 33: 221-31.

71. Dutra RCL, Soares BG, Campos EA and Silva JLG. Hybrid composites based on polypropylene and carbon fiber and epoxy matrix. *Polymer* 2000; 41: 3841-49.

72. He J, Zhang H and Wang Y. *In-situ* hybrid composites containing reinforcements at two orders of magnitude. *Polymer* 1997: 38(16): 4279-83.

73. He J, Wang Y and Zhang H. In situ hybrid composites of thermoplastic poly(ether ether ketone), poly(ether sulfone) and polycarbonate. *Composites Science and Technology* 2000; 60: 1919-30.

74. Kay R. Resin systems. Ch. 2B in *Fibre Composite Hybrid Materials*. Hancox NL (Ed). Applied Science Publishers, London, 1981.

75. Schmitt-Thomas, KhG, Yang ZG and Malke R. Failure behavior and performance analysis of hybrid-fiber reinforced PAEK composites at high temperature. *Composites Science and Technology* 1998; 58: 1509-18.

76. Tattersall P. Manufacturing processes. Ch. 2C in *Fibre Composite Hybrid Materials*. Hancox NL (Ed). Applied Science Publishers, London, 1981.

77. Ahmadian R and Mantena PR. Modal characteristics of structural portal frames made of mechanically joined pultruded flat hybrid composites. *Composite Part B: Engineering* 1996; 27: 319-28.

78. Nori CV, McCarty TA and Mantena PR. Vibration analysis and finite element modeling for determining shear modulus of pultruded hybrid composites. *Composite Part B: Engineering* 1996; 27: 329-37.

79. Chiu CH, Tsai KH and Huang WJ. Crush-failure modes of 2D triaxially braided hybrid composite tubes. *Composites Science and Technology* 1999; 59: 1713-23.

80. Vlot A and Gunnink JW (Eds). *Fibre Metal Laminates: an Introduction*. Kluwer, Dordrecht, The Netherlands, 2001.

81. Vlot A. *Glare: History of the Development of a New Aircraft Material*. Kluwer, Dordrecht, The Netherlands, 2001.

82. Vermeeren C (Ed). *Around Glare: a New Aircraft Material in Context*. Kluwer, Dordrecht, The Netherlands, 2002.

83. Song JI and Han KS. Effect of volume fraction of carbon fibers on wear behavior of Al/Al$_2$O$_3$/C hybrid metal matrix composites. *Composites Structures* 1997; 39(3-4): 309-18.

84. Jang J and Lee C. Performance improvement of GF/CF functionally gradient hybrid composite. *Polymer Testing* 1998; 17: 383-94.

85. Xu Y, Otsuka K, Yoshida H, Nagai H, Oishi R, Horikawa H and Kishi T. A new method for fabricating SMA/CFRP smart hybrid composites. *Intermetallics* 2002; 10: 361-69.

86. Tylikowski A and Hetnarski RB. Semiactive control of a shape memory alloy hybrid composite rotating shaft. *Int. J. of Solids and Structures* 2001; 38: 9347-57.

87. Yang D. Shape memory alloy and smart hybrid composites – advanced materials for the 21st century. *Materials and Design* 2000; 21: 503-05.

88. Birman V, Chandrashekhara K and Sain S. An approach to optimization of shape memory alloy hybrid composite plates subject to low-velocity impact. *Composite Part B: Engineering* 1996; 27: 439-46.

89. Muto N, Arai Y, Shin SG, Matsubara H, Yanagida H, Sugita M and Nakatsuji T. Hybrid composites with self-diagnosing function for preventing fatal fracture. *Composites Science and Technology* 2001; 61: 875-83.

90. Kalnin IL. Evaluation of unidirectional glass-graphite fiber/epoxy resin composites. *Composite Materials: Testing and Design (Second Conference), ASTM STP 497*. American Society for Testing and Materials, Philadelphia, 1972: 551-63.

91. Aveston J and Sillwood JM. Synergistic fibre strengthening in hybrid composites. *J. of Materials Science* 1976; 11: 1877-83.

92. Zweben C. Tensile strength of hybrid composites. *J. of Materials Science* 1977; 12: 1325-37.

93. Maron G, Fischer S, Tuler FR and Wagner HD. Hybrid effects in composites: conditions for positive or negative effects versus rule-of-mixtures behaviour. *J. of Materials Science* 1978; 13: 1419-26.

94. Phillips MG. Elastic and thermal properties of composites. Ch. 3 in *Fibre Composite Hybrid Materials*. Hancox NL (Ed). Applied Science Publishers, London, 1981.

95. Kretsis G. A review of the tensile, compressive, flexural and shear properties of hybrid fibre-reinforced plastics. *Composites* 1987; 18: 13-23.

96. Leischner U and Johnson AF. Micromechanics analysis of hybrid woven fabric composites under tensile and compressive load. *Composite Materials Technology* 1994; IV: 397-405.

97. Ishikawa T and Chou TW. Elastic bahaviour of woven hybrid composites. *J. of Composite Materials* 1982; 16: 2-19.

98. Prevorsek DC, Kwon YD and Chin HB. Analysis of the temperature rise in the projectile and extended chain polyethylene fiber composite armor during ballistic impact and penetration. *Polymer Engineering and Science* 1994; 34: 141-52.

99. Lee BL, Walsh TF, Won ST and Patts HM. Penetration failure mechanisms of armor-grade fiber composites under impact. *J. of Composite Materials* 2001; 35(18): 1605-33.

100. Camanho PP and Matthews FL. Stress analysis and strength prediction of mechanically fastened joints in FRP: a review. *Composite Part A: Applied Science and Manufacturing* 1997; 28: 529-47.

101. Oh JH, Kim YG and Lee DG. Optimum bolted joints for hybrid composite materials. *Composites Structures* 1997; 38(1-4): 329-41.

102. Dvorak GJ, Zhang J and Canyurt O. Adhesive tongue-and-groove joints for thick composite laminates. *Composites Science and Technology* 2001; 61: 1123-42.

103. Hart-Smith LJ. Further developments in the design and analysis of adhesive-bonded structural joints. *Joining of Composite Materials, ASTM STP 749*. Kedward K (Ed). American Society for Testing and Materials, Philadelphia, 1981: 3-31.

104. Delale F, Erdogan F and Aydinoglu MN. Stresses in adhesively bonded joints: a close-form solution. *J. of Composite Materials* 1981; 15: 249-71.

105. Delale F and Erdogan F. Viscoelastic analysis of adhesively bonded joints. *J. of Applied Mechanics* 1981; 48: 331-38.

106. Bahei-El-Din YA and Dvorak GJ. New designs of adhesive joints for thick composite laminates. *Composites Science and Technology* 2001; 61: 19-40.

107. Matthews FL, Roshan AA and Phillips LN. The bolt bearing strength of glass/carbon hybrid composites. *Composites* 1982; 13: 225-27.

108. Achenbach JD. *Wave Propagation in Elastic Solids*. North-Holland Publishing, Amsterdam, The Nethelands, 1973.

109. Liu D and Malvern LE. Matrix cracking in impacted glass/epoxy plates. *J. of Composite Materials* 1987; 21: 594-609.

110. Wu HT and Springer GS. Measurements of matrix cracking and delamination caused by impact on composite plates. *J. of Composite Materials* 1988; 22: 518-532.

111. Liaw BM, Pierides AM and Liu YX. Ultrasonic assessment of impact damage in aluminum/acrylic sandwich plates. *Proceedings of the SEM Annual Conference on Experimental and Applied Mechanics*, Portland, OR, June 4-6, 2001: 264-68.

112. Cantwell WJ and Morton J. Geometrical effect in the low velocity impact response of CFRP. *Composite Structures* 1989; 12: 39-60.

113. Liu D. Impact induced delamination: a view of bending stiffness mismatching. *J. of Composite Materials* 1988; 22: 674-92.

114. Avery WB and Grande DH. Influence of materials and lay-up parameters on impact damage mechanisms. *Proceedings of the 22nd International SAMPE Technical Conference*, Nov. 6-8, 1990: 470-83.

115. Ambut DR, Prasad CB and Waters WA. A drop weight apparatus for low speed impact testing of composite structures. *Experimental Mechanics* 1995; 35: 77-82.

116. Winkel JD and Adam DF. Instrumented drop weight impact testing of cross-ply and fabric composites. *Composites* 1985; 16(4): 268-78.

117. Delfosse D, Pageau G, Bennett A and Pousatrip A Insteumented impact testing at high velocities. *J. of Composite Technology and Research* 1993; 15(1): 38-45.

118. Strait LH, Karasek ML and Amateau MF. Effects of stacking sequence on the impact resistance of carbon fiber reinforced thermoplastic toughened epoxy laminates. *J. of Composite Materials* 1992; 26: 1725-40.

119. Dransfield K, Baillie C and Mai YW. Improving the delamination resistance of CFRP by stitching – a review. *Composite Science and Technology* 1994; 50(3): 305-17.

120. Pelstring RM. Stitching to improve damage tolerance of composites. *The 34th International SAMPE Symposium*, Reno, Nevada, May 8-11, 1989: 1519-28.

121. Sun CT and Chen JK. On the impact of initially stressed composite laminates. *J. of Composite Materials* 1985; 19: 490-504.

122. Nishijima S and Okada T. Charpy impact test of cloth reinforced epoxide resin at low temperature. *Nonmetallic Materials and Composites at Low Temperatures*, Hartwig G and Evans D (Eds), Plenum Press, New York, 1982: 259-75.

123. Dutta P, Faran K and Hui D. Influence of low temperature on energy absorption in laminated composites. *Proceedings of the Ninth International Conference on Composite Materials, ICCM/9*, Vol. V: Composites Behaviour, Miravete A (Ed), Madrid, Spain, July 12-16, 1993: 311-320.

124. Tan TM and Sun CT. Use of static indentation laws in the impact analysis of laminated composites. *J. of Applied Mechanics* 1985; 52: 6-12.

125. Shivakumar KN, Elber W and Illg W. Prediction of impact force and duration due to low-velocity impact on circular composite laminates. *J. of Applied Mechanics* 1985; 52: 674-80.

126. Shivakumar KN, Elber W and Illg W. Prediction of low-velocity impact damage in thin circular laminates. *AIAA J.* 1985; 23(3): 442-49.

127. Sun CT and Grady JE. Dynamic delamination fracture toughness of a graphite/epoxy laminate under impact. *Composite Science and Technology* 1988; 31: 55-72.

128. Sun CT and Jih CJ. Mechanics of delamination in composite laminates subjected to low velocity impact. *Impact Response and Elastodynamics of Composites, ASME AMD Vol. 116*, Mal AK and Rajapakse YDS (Eds) 1990: 1-10.

129. Choi HY and Chang FK. A model for predicting damage in graphite/epoxy laminated composites resulting from low velocity point impact. *J. of Composite Materials* 1992; 26: 2134-69.

130. Salpekar SA. Analysis of delamination in cross-ply laminates initiating from impact induced matrix cracking. *J. of Composites Technology and Research* 1993;15: 88-94.

131. Razi H and Kobayashi AS. Delamination in cross-ply laminated composite subjected to low-velocity impact. *AIAA Journal* 1993; 31: 1498-1502.

132. Zukas JA. Numerical simulation of impact phenomena. Ch. 10 in *Impact Dynamics*. Zukas, JA, Nicholas T, Swift HF, Greszczuk LB and Curran DR (Eds). Wiley, New York, NY, 1982.

133. Zukas JA. Three-dimensional computer codes for high velocity impact simulation. Ch. 11, *ibid*.

134. Rajendran AM and Kroupa JL. Impact damage model for ceramic materials. *J. of Applied Physics* 1989; 66(8): 3560-65.

135. den Reijer PC. *Impact on Ceramic Faced Armour*. Ph.D. Thesis, Delft University, 1991.

136. Grady DE and Winfree NA. Impact fragmentation of high-velocity compact projectiles on thin plates: a physical and statistical characterization of fragment debris. *Int. J. of Impact Engineering* 2001; 26: 249-62.

137. Fellows, NA and Barton PC. Development of impact model for ceramic-faced semi-infinite armour. *Int. J. of Impact Engineering* 1999; 22: 793-811.

138. Boeing Specification Support Standard BSS 7260, *Advanced Composite Compression Tests*, The Boeing Company, Seattle, WA (originally issued February 1982, revised December 1988).

139. Lal KM. Residual strength assessment of low velocity impact damage of graphite-epoxy laminates. *J. of Reinforced Plastics and Composites* 1983; 2: 226-38.

140. Cantwell WJ and Morton J. The impact resistance of composite materials – a review. *Composites* 1991; 22: 347-62.

141. Romeo G and Gaetani G. Effect of low velocity impact damage on the buckling behavior of composite panels. *Proceedings of the 17th Congress of ICAS*, Stockholm, Sweden, September 9-14, 1990; 1: 994-1004.

142. Naik NK. *Woven Fabric Composites*. Technomic Publishing, Lancaster, PA, 1994.

143. Naik NK, Sekher YC and Meduri S. Damage in woven-fabric composites subject to low-velocity impact. *Composites Science and Technology* 2000; 60: 731-44.

144. Kim JK and Sham ML. Impact and delamination failure of woven-fabric composites. *Composites Science and Technology* 2000; 60: 745-61.

145. Kang TJ and Kim C. Energy-absorption mechanisms in Kevlar multiaxial warp-knit fabric composites under impact loading. *Composites Science and Technology* 2000; 60: 773-84.

146. Pandita SD, Falconet D and Verpoest I. Impact properties of weft knitted fabric reinforced composites. *Composites Science and Technology* 2002; 62: 1113-23.

147. Wu E and Liau J. Impact of unstitched and stitched laminates by line loading. *J. of Composite Materials* 1993; 27: 1443-64.

148. Mouritz AP, Gallagher J and Goodwin AA. Flexural strength and interlaminar shear strength of stitched GRP laminates following repeated impacts. *Composites Science and Technology* 1997; 57: 509-22.

149. Mouritz AP. Ballistic impact and explosive blast resistance of stitched composites. *Composite Part B: Engineering* 2001; 32: 431-39.

150. Sato C and Ikegami K. Dynamic deformation of lap joints and scarf joints under impact loads. *Int. J. of Adhesion & Adhesives* 2000; 20: 17-25.

151. Bezemer AA, Guyt CB and Vlot A. New impact specimen for adhesives: optimization of high-speed loaded adhesive joints. *Int. J. of Adhesion & Adhesives* 1998; 18: 255-60.

152. Adams RD and Harris JA. A critical assessment of the block impact test for measuring the impact strength of adhesive bonds. *Int. J. of Adhesion & Adhesives* 1996; 16(2): 61-71.

153. Kinloch AL and Kodokian GA. The impact resistance of structural adhesive joints. *J. of Adhesion* 1987; 24(1): 109-26.

154. Lee YS, Kang KH and Park O. Response of hybrid laminated composite plates under low-velocity impact. *Computers and Structures* 1997; 65(6): 965-74.

155. Meyers MA. *Dynamic Behavior of Materials*. Wiley, New York, NY, 1994.

156. Nicholas T. Material Behavior at high strain rates. Ch. 8 in *Impact Dynamics*. Zukas, JA, Nicholas T, Swift HF, Greszczuk LB and Curran DR (Eds). Wiley, New York, NY, 1982.

157. Curran DR. Dynamic Fracture. Ch. 9 in *Impact Dynamics*. *ibid*.

158. Adanur S, Tsao YP and Tam CY. Improving fracture resistance of laminar textile composite by the third direction reinforcement. *Composite Engineering* 1995; 5(9): 1149-58.

159. Liu D, Shakour E and Lu X. Joining forces in assembled composite beams. *J. of Composite Materials* 2001; 35(22): 1985-2008.

160. Liu D and Raju BB. Effects of joining techniques on impact perforation assembled composite plates. *Experimental Mechanics* 2000; 40(1): 46-53.

161. Liu D. Delamination resistance in stitched and unstitched composite plates subjected to impact loading. *J. of Reinforced Plastics and Composites* 1990; 9(1): 59-69.

162. Garg AC and Mai YW. Failure mechanisms in toughened epoxy resin – a review. *Composites Science and Technology* 1988; 31(3): 179-223.

163. Cheung CK, Liaw BM, Delale F, Walser AD and Raju BB. Bending-induced damages of S2 glass/toughened epoxy composites at room and elevated temperatures. *Proceedings of the 13th Annual Technical Conference on Composite Materials, American Society for Composites*, Baltimore, Maryland, September 21-23, 1998: 981-90.

164. Liaw BM, Cheung CK, Delale F, Walser AD and Raju BB. Tension-induced damages of S2 glass/toughened epoxy composites at room and elevated temperatures. *Proceedings of the 13th Annual Advanced Composite Conference & Exposition, ACCE'98*, Mechanics Session, Paper No. 3, Cobo Center, Detroit, MI, September 28-29, 1998.

165. Cheung CK, Long X, Liaw BM, Delale F, Walser AD and Raju BB. Temperature effect on damage in S2 glass/toughened epoxy composites. *Durability and Damage Tolerance of Composite Materials and Structures - 1999, MD-Vol. 86/AMD-Vol. 232,* Pelegri A, Chan WS, Haque A and Hosur MV (Eds). The 1999 ASME International Mechanical Engineering Congress and Exposition, Nashville, TN, November 14-19, 1999: 41-49.

166. Pike T, McArthur M and Schade D. Vacuum assisted resin transfer molding of a layered structural laminate for application on ground combat vehicles. Proceedings of the 28th International SAMPE Technical Conference, Seattle, WA, November 4-7, 1996: 374-80.

167. Fink BK and Gillespie JW, Jr. *Cost-Effective Manufacturing of Damage-Tolerant Integral Armor*. ARL-TR-2319, U.S. Army Research Laboratory, September 2000.

168. Knoell AC and Robinson EY. Analysis of truss, beam, frame, and membrane components, Ch. 3 in Structural Design and Analysis, Part I, Chamis CC (Ed), *Composite Materials*, Vol. 7, Broutman LJ and Krock RH (Eds), Academic Press, New York 1975.

169. Skudra, AM, Bulavs FYa, Gurvich MR and Kruklinsh. *Analysis of Composite Beam Systems*, Technomic Publishing, Lancaster, PA 1991.

170. Karal M. *AST Composite Wing Program – Executive Summary*. NASA CR 2001-210650, 2001.

171. Chatelet E, Lornage D and Jacquet-Richardet G. A three dimensional modeling of the dynamic behavior of composite rotors. *Int. J. of Rotating Machinery* 2002; 8(3): 185-92.

172. Wang K. *Vibration Analysis of Cracked Composite Bending-torsion Beams for Damage Diagnosis*. Ph.D. dissertation, Virginia Polytechnic Institute and State University, Blacksburg, VA 2004.

173. Barrett DJ. The mechanics of Z-fiber reinforcement. *Composite Structures* 1996; 36: 23-32.

174. Dow, MB and Dexter HB. Development of stitched, braided and woven composite structures in the ACT program and at Langley Research Center (1985 to 1997) – summary and bibliography. NASA/TP-97-206234, 1997.

175. Stickler PB and Ramulu M. Investigation of mechanical behavior of transverse stitched T-joints with PR520 resin in flexure and tension. *Composite Structures* 2001; 52(3-4): 307-314.

176. Cheung CK, Long X, Liaw BM, Delale F, Walser AD and Raju BB. Composite strips with a circular stress concentration under tension. *Proceedings of the SEM X International Congress & Exposition on Experimental and Applied Mechanics*, Section 89: Composites, Paper No. 387, Costa Mesa, CA, June 7-10, 2004.

177. Cheung CK, Liu JJ, Liaw BM, Delale F and Raju BB. Tension-induced damage in composite strips with a center hole or a pin joint at various temperatures. presented in *the International Mechanical Engineering Congress and Exposition*, New York, NY, November 2001.

178. LS-DYNA 971, Livermore Software Technology Corporation (LSTC), Livermore, CA. http://www.lstc.com.

179. Chang, FK and Chang KY. Post-failure analysis of bolted composite joints in tension or shear-out mode failure. *J. of Composite Materials* 1987; 21: 809-33.

180. Chang, FK and Chang KY. A progressive damage model For laminated composites containing stress concentrations. *J. of Composite Materials* 1987; 21: 834-55.